Microstructural Mechanisms of Solid State Interreactions

Guido Schmitz
Universität Göttingen, 2001

Abstract

The interreaction of materials is often considered within the framework of continuum models, which neglect the internal microstructure of the materials. By contrast, recent experimental studies demonstrate that the microstructural conditions may control the reaction kinetics and in some cases even the choice among different reaction channels.

This thesis especially addresses the underlying atomic mechanisms. In order to determine atomic transport and transformations on the nanometer length scale, most recent microscopic methods like Z-contrast electron microscopy and atomprobe tomography are applied. The set-up and further development of these experimental techniques are described in detail. Then, results of case studies of reactions between metallic thin films are presented, which address different physical situations of increasing complexity. The early interdiffusion stages of two fcc metals are investigated by using the model systems Cu/Au and Ag/Au. The different behaviour of these two systems allows important conclusions on the role of mismatch stress and the mechanisms of its relaxation. The selection and nucleation of product phases are studied at Al/Ag and Al/Ni interfaces. Atom probe tomography reveals in both cases precursory stages in dependence on the initial microstructure. As these intermediate products do not agree with the equilibrium phase diagram, the observed phenomena emphasize the kinetic nature of early reaction stages.

To Maria, Theresia, Jakob and Clara

Contents

1   Introduction

In recent decades, we got used to measure technological progress by the ever-increasing packaging density of electronic devices, which revolutionized data procession and by that our daily life [1]. Almost unnoticed by the public, this technical revolution was made possible by an improved understanding of materials' interactions, which allows to control stability and properties of various interfaces on a length scale of only a few nanometers. It might be stated without exaggeration that the reaction of solids joining at a common interface kept physicists and material scientist excited, at least since the famous interdiffusion experiments of Kirkendall in 1947 [2].

To a major part, the remarkable interest stems from applications of enormous economic potential. The control of the Si/SiO_2 interface and the formation of silicide contacts by reaction of Si with appropriate metals are prerequisites to build the field-effect transistor, the basic switching element of today's data technology. The active surface of modern hard-disks comprises a multilayer composite of various metallic thin films, each selected for a well-defined function. Recent applications of the 'giant magneto-resistance' (GMR) in magnetic sensors and future data storage devices require metallic layers or oxide tunnel barriers of only 1 to 2 nm thickness, which have to be stable under application conditions, even at the elevated temperatures under the hoods of motor vehicles [3]. Less obvious examples may be found from the adhesion of surface coatings, the interaction between matrix and reinforcements in composite materials or the reversible reactions taking place in secondary batteries.

On the other hand, one must not overlook that solid state interreactions are a challenge to basic science, too. This point of view at least motivates the study of model systems presented in this thesis. With decreasing layer thickness, attention is drawn to the earliest reaction stages, which are distinguished by steep composition gradients. This way, highly non-equilibrium states are prepared, of which the kinetic behaviour is no longer described by equilibrium thermodynamics. As a representation of 'near-equilibrium' physics, diffusional laws predict the immediate formation of all intermetallic compounds known from the equilibrium phase diagram. By contrast, in the experiment usually only one phase is observed in very early reaction stages. Frequently, this phase is a metastable one and in most prominent examples even amorphous. The discovery of the so called 'solid state amorphization reaction' (SSAR) [4, 5, 6] caused particular excitement, as it emphasized the kinetic nature of early interreaction stages and proved at the same time the metastable nature of amorphous structures.

Up to now, nucleation mechanisms, the selection of the first product phase, and especially the stabilization of non-equilibrium phases are not really understood. Established models are solely based on a continuum approach using near-

equilibrium transport equations in a layered reaction geometry. If necessary, kinetic constraints are introduced in an ad-hoc manner to explain the suppression of equilibrium phases. Often, this unsatisfying theoretical situation arises from very limited experimental data, which seems to be a surprising statement in view of the enormous work and effort done in the last decades. However, it is still very difficult to observe transport and reaction on the required nanometer scale.

Early experimental data are based on depth profiling techniques like Rutherford back scattering (RBS) or secondary ion mass spectrometry (SIMS), which do not provide sufficient information in lateral direction along the interface. X-ray diffraction can be interpreted only by using a-priori models, for which often a simple layer geometry had to be assumed because of lacking microscopic data. This situation has changed by the remarkable progress of microscopic tools. High resolution electron microscopy established as a standard method in the eighties of the last century. It yields insight into structural transformations at interfaces in atomic resolution, so that atomic mechanisms of reaction barriers could be addressed experimentally for the first time [7, 8, 9]. In recent years, particular effort has been devoted to the development of spatially resolved nano-analysis, which is required to identify atomic transport paths and to determine to which extend the composition of early reaction products agrees with the prediction of phase diagrams.

The work presented in this thesis deals especially with this latter problem. Developing and applying state-of-the-art nano-analytical tools, the atomic transport mechanisms and the composition of early products are determined microscopically. Three experimental studies are presented, which address different physical situations. The work concentrates on the reaction between metals. Compared to covalent or ionic materials, metals are highly tolerant to structural defects, which is why metals are preferred construction materials. For the work here, this has important consequences, as metallic thin films usually form a nano-crystalline microstructure, distinguished by a high density of grain boundaries and dislocations. It will be shown, that this microstructural constraint forces a complicated three dimensional morphology of the reaction zone. Under this condition, phenomena might develop, which would not be observed in epitaxial semiconductor or ceramic specimens. On the other hand, the 3D reaction morphology requires an advanced microscopic analysis able to determine local compositions with nanometer resolution.

The present report is subdivided into several sections which allows the reader to concentrate on the topic of his interest. In a brief survey the actual physical knowledge on the kinetics of interreactions is sketched. I tried to keep this outline very short, but a common basis is necessary to understand the motivation of the presented experiments and their interpretation. For chemical analysis, a special version of Z-contrast electron microscopy and atom probe tomography

have been applied. The physical principles of these methods, recent developments and application examples are described in the third chapter.

In the fourth chapter, the interdiffusion between two fcc metals is studied at the examples of Cu/Au (above the ordering temperature) and Ag/Au. Apparently, a very simple situation, since no compound is formed during the reaction, and furthermore epitaxially interfaces are prepared. Thus, one might expect diffusion by simple random walk. However, the reactions develop quite differently, because of the considerable lattice mismatch in the case of Cu/Au. This results in plastic deformation and finally in the recrystallization of the diffusion zone. As the dominant mechanism occurs on the length scale of several tens of nanometers, the investigation is mainly based on cross section electron microscopy.

The nucleation of product phases is especially addressed in a study of Al/Ag presented in the fifth chapter. According to earlier X-ray diffractometry only one product phase forms in thin film reactions of these metals. However in this case, atomprobe analysis reveals the formation of the expected compound way of its equilibrium composition. The final state is achieved in a subsequent step by means of a decomposition instead of the conventional mixing reaction.

A study on phase selection in Ni/Al is reported in the last chapter. This binary system shows a sequence of several intermetallics formed subsequently in the reaction zone. The influence of different microstructures on the reaction mechanism is demonstrated using different layer deposition methods. Atomprobe tomography combined with diffractometry reveals that also in Ni/Al, a compound of the equilibrium phase diagram is formed at first in a non-equilibrium state, distinguished by deviations in its composition and degree of long range order. The stabilization of this intermediate state is considered based on Monte-Carlo simulations of the reaction.

2 The physics of solid state interreactions

Certainly, the so-called *phase selection* represents the most striking phenomenon regarding the early stages of interreactions. Opposed to late stages, where all equilibrium phases of a system appear in a layered stack, during early stages usually only one phase is observed. Up to now, the understanding of this effect is a scientific challenge. After several decades of research, it is still controversial whether the first product is determined by a competition in growth or by selective nucleation. In the following, established concepts to describe layer growth and nucleation are discussed.

2.1 Growth kinetics

Triggered by the limited information obtained with depth profiling techniques, interreactions are often considered on a well-defined layer geometry. In this framework, the reaction is completely characterized by the evolution of one-dimensional composition profiles like that shown in fig. 1. As an immediate consequence of the layer geometry, atomic transport through the products is required for further thickness growth of the reaction zone. The resulting diffusion problem was solved by Kirkaldy [10] and by Kidson [11], assuming that compositions at the interfaces match those of local equilibrium. Furthermore, each phase is characterized by a composition independent interdiffusion coefficient.

At the interfaces conservation of matter must be obeyed. Hence, the movement of an interface is determined by the balance of related currents according to

$$\frac{\mathrm{d}x_k}{\mathrm{d}t} = \frac{j_k - j_{k-1}}{c_i^{(k)} - c_f^{(k-1)}} \,.$$ (1)

(For a definition of the variables see fig. 1.) Growth of a layer is defined by the relative position of its two interfaces. In consequence, the growth of a phase
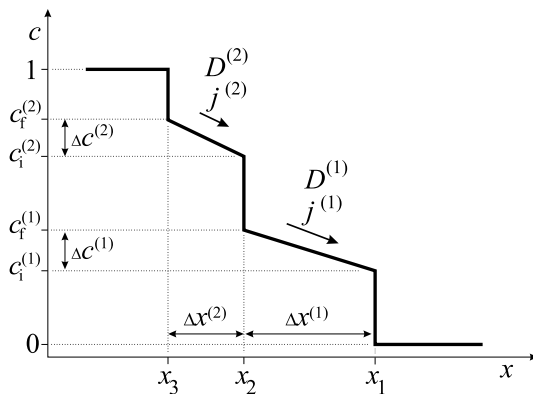

Figure 1: Schematic composition profile through a reaction zone with two reaction products. For the sake of simplicity, the solubility of the terminating phases is assumed to be negligible.

depends not only on the transport through itself, but also on that through its neighbors, which indicates the competitive nature of phase formation. In other words, although stable in equilibrium, a phase may shrink inside the diffusion zone, because of the overwhelming growth of its neighbors.

Let us consider the simple situation sketched in fig. 1 to discuss this competition in further detail. Two intermetallic phases have formed. The solubility in both terminating phases is assumed to be negligible to avoid lengthy formulas. In this case, the growth of the compound layers is given by[1]

$$\frac{\mathrm{d}\triangle x^{(1)}}{\mathrm{d}t} = \frac{\mathrm{d}x_1}{\mathrm{d}t} - \frac{\mathrm{d}x_2}{\mathrm{d}t} = C_{1,1} \cdot j^{(1)} + C_{1,2} \cdot j^{(2)} \tag{2}$$

$$\frac{\mathrm{d}\triangle x^{(2)}}{\mathrm{d}t} = \frac{\mathrm{d}x_2}{\mathrm{d}t} - \frac{\mathrm{d}x_3}{\mathrm{d}t} = C_{2,1} \cdot j^{(1)} + C_{2,2} \cdot j^{(2)} , \tag{3}$$

where

$$C_{1,1} = \frac{1}{c_{\mathrm{i}}^{(2)} - c_{\mathrm{f}}^{(1)}} + \frac{1}{c_{\mathrm{i}}^{(1)}} \tag{4}$$

$$C_{2,2} = \frac{1}{c_{\mathrm{i}}^{(2)} - c_{\mathrm{f}}^{(1)}} + \frac{1}{1 - c_{\mathrm{f}}^{(2)}} \tag{5}$$

$$C_{1,2} = C_{2,1} = -\frac{1}{c_{\mathrm{i}}^{(2)} - c_{\mathrm{f}}^{(1)}} . \tag{6}$$

The growth competition between both compounds is conveniently expressed by the current ratio $r := j^{(1)}/j^{(2)}$. It is seen from Eq. 2 that growth of compound (1) requires

$$r > r_1 := -C_{1,2}/C_{1,1} . \tag{7}$$

Likewise

$$r < r_2 := -C_{2,2}/C_{1,2} \tag{8}$$

is needed for the growth of compound (2) according to Eq. 3.

The most important point to notice here is that a diffusion controlled kinetics will never predict a phase to shrink away. As r_1 is always smaller than r_2, we face a situation as sketched in fig. 2. Assuming initially a current ratio $r < r_1$ (situation I. in the figure), at first compound (1) will shrink. But at the same time $j^{(1)}$ gradually increases according to Ficks law $j^{(1)} = -D^{(1)}/\triangle x^{(1)}$. Thus, before the compound can disappear the current ratio will reach r_1, where the compound starts growing again. Finally, a steady state of constant current ratio is reached. The analogous behaviour is expected for the opposite initial situation (II.). Thus, in the steady state all compounds will grow according to a parabolic time law. Apart from geometrical factors of the order of unity, which take into account the peculiarities of the underlying phase diagram, the relative thickness of a compound is fixed by its characteristic product $D^{(k)} \cdot \triangle x^{(k)}$ [11].

---

[1]The general case of an arbitrary number of compounds is formulated by a similar linear equation with a tri-diagonal matrix (C_{ij}) [11]
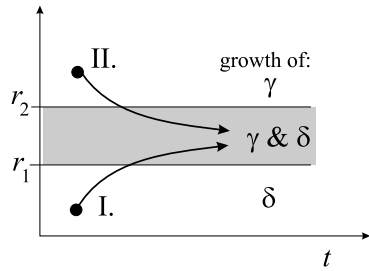
Figure 2: Development of the current ratio during diffusional growth

This concomitant parabolic growth is certainly one of the best confirmed laws of material physics. It is of similar generality as the Ostwald ripening controlling decomposition reactions. However, like the latter, it is only valid in late reaction stages. In reaction of thin films, the steady state is usually never reached, because of the limited supply of unreacted material. Furthermore, experimental time exponents deviate from the parabolic growth law and frequently, expected compounds fail to appear.

The shortcoming of any diffusional ansatz in the limit of thin foils is quite general, since infinite transport rates are predicted at the very beginning. This failure may be overcome, if reaction barriers at the interfaces are taken into account, which limit the maximum atomic current [12]. For that, the first Ficks law is modified to

$$j = -\frac{D\triangle c}{\triangle x + D/\kappa},$$ (9)

where the reaction constant κ describes the average transport properties at both interfaces of a layer. Thus, in the very early stage, when $\triangle x$ is still negligible in the denominator of Eq. 9, j is predicted to be constant and phase growth should be proportional to the annealing time. Linear growth regimes are indeed observed experimentally, particularly in the case of oxidation reactions [12] and the formation of some silicides (eg. VSi_2, WSi_2[13]).

In a famous analysis, Gösele and Tu [14] demonstrated that interfacial barriers are sufficient to explain the suppression of phases in early reaction stages. This is seen immediately from Eqs. 2 and 3, if atomic currents of the form of Eq. 9 are introduced. In the case that the transport through the boundaries of compound (1) is very sluggish, so that

$$\frac{\kappa^{(1)}\triangle c^{(1)}}{\kappa^{(2)}\triangle c^{(2)}} < r_1,$$ (10)

compound (1) is at first suppressed. Only after compound (2) has grown to reach the diffusion controlled regime ($\triangle x^{(2)} > D^{(2)}/\kappa^{(2)}$), j_2 may slow down sufficiently that

$$r = \frac{\kappa^{(1)}\triangle c^{(1)}\triangle x^{(2)}}{D^{(2)}\triangle c^{(2)}} = r_1.$$ (11)

Thus, compound (2) must have reached a critical thickness

$$\triangle x_{\text{cr.}}^{(2)} = r_1 \, D^{(2)} \triangle c^{(2)} / \kappa^{(1)} \triangle c^{(1)} \tag{12}$$

before compound (1) can start growing.

In spite of the remarkable success in explaining the suppression of phases, one must not overlook that an experimental proof of the theory is rather difficult. Numerous parameters must be known for a quantitative check. Particularly, interfacial reaction constants are hard to determine and in addition seem to depend on actual preparation conditions [14]. Nevertheless, in the case of Ni silicide formation, the necessary reaction constant could be estimated from the linear growth regimes; a critical thickness of about $2\,\mu$m was derived, which roughly corresponds to the experimental observation that for diffusion widths larger than $10\,\mu$m all equilibrium phases are usually present.

By contrast, for reactions between metals, the effect of interfacial barriers is still a matter of controversy. Diffusion coefficients of the compounds in a metallic system often differ by several orders of magnitude. Regarding the phase thicknesses predicted for the steady state of diffusion, fast growing phases may reach a thickness of several microns before slower ones become visible in the reaction zone. According to d'Heurle [15], the very simple rule that the phase of highest diffusivity is formed first, yields a correct prediction in the overwhelming number of cases. Thus, a pronounced difference in the diffusivity of the compounds dominates other minor factors like different thermodynamic driving forces or interfacial reaction barriers.

Furthermore, in most metallic reaction couples no clear regime of linear growth is observed, indicating that the atomic re-arrangements required at the interfaces proceed very fast. Interfacial barriers may limit the diffusional transport only below a phase thickness of at most a few nanometer [4]. In these early stages, it is doubtful whether a dense layer has actually formed, as will be demonstrated later in this thesis. In addition, nuclei of the product phase are expected to have a comparable size. Thus, it is suggested that nucleation effects play a more important role in determining the phase sequence than interfacial barriers (see also [16]). As the analysis by Gösele and Tu can be formulated only for the case that a local equilibrium between adjacent phases is established, the model cannot explain the kinetic stabilization of metastable phases in general (see [17]). For that, either nucleation rates [18] or kinetic arguments concerning the overall transformation rate [19] must be considered.

2.2   Phase selection rules

Since it depends on numerous, mostly unknown parameters, the growth kinetic approach is of limited use in predicting the first product of an interreaction.

Therefore, several attempts were undertaken to develop simple rules, which rely only on phase diagrams and basic thermodynamic data (see e.g. [20]). The presently most advanced selection rule was proposed by Pretorius [21, 22]. As its predictions are remarkably reliable, it must be mentioned here, although a sound physical justification is still lacking. Nevertheless, the rule probably indicates the two major factors of a future general theory, as it combines thermodynamic with kinetic arguments.

Following Pretorius, the compound forming first in a metal-metal reaction *has the most negative effective heat of formation at the composition of the lowest liquidus* [22]. The principle of this rule is best explained using a concrete example: figure 3 shows the phase diagram of Al-Au (a) and the heat of formation of the different intermetallics under consideration (b). The heat of formation is taken as an approximate measure for the driving force to form a particular compound[2]. Assuming that the diffusivity of an alloy is scaled with its melting point, Pretorius postulates the formation of a thin reaction layer with the composition c_r of the system's lowest melting point, at which intermixing should be most effective. In this reaction layer, the compound having the highest driving force is nucleated. To calculate the driving force, the maximum volume fraction of a compound, which can be obtained according to the 'lever rule', must be taken into account. Thus, the heat of formation is reduced to an effective one, if the composition of the reaction layer deviates from that of the compound. For example for the case that c_r is lower than the stoichiometric composition c^* of the compound, we have

$$\triangle H_{\text{eff}} = \frac{c_r}{c^*} \cdot \triangle H \, . \tag{13}$$

In fig. 3, this 'effective heat of formation' is indicated by straight lines connecting the data of the compounds with the corners of the pure elements. In Al-Au, the lowest melting point is found at the eutectic of 78 at% Au. At this composition, two intermetallics, Au_2Al and Au_5Al_2, have a similar effective heat of formation significantly larger than that of the other compounds. Because of the very small difference between these two intermetallics, both are indeed observed as first forming phases depending on the exact experimental conditions [24, 25].

The example of Al/Au is quite remarkable, as it emphasizes the interplay of kinetic and thermodynamic factors. From the thermodynamic stability of the different compounds, the formation of AuAl would be expected. Relying on the other hand on kinetic arguments, the formation of Au_4Al is predicted erroneously, as this phase is closest to the lowest eutectic (Walser-Bené rule [20]). Only the combination of both factors as proposed by Pretorius seems to yield the correct prediction.

---

[2]Strictly the difference in the Gibbs free energy has to be used, but data for the heat of formation are more easily achieved by calorimetric measurements or even estimated by empirical models [23]
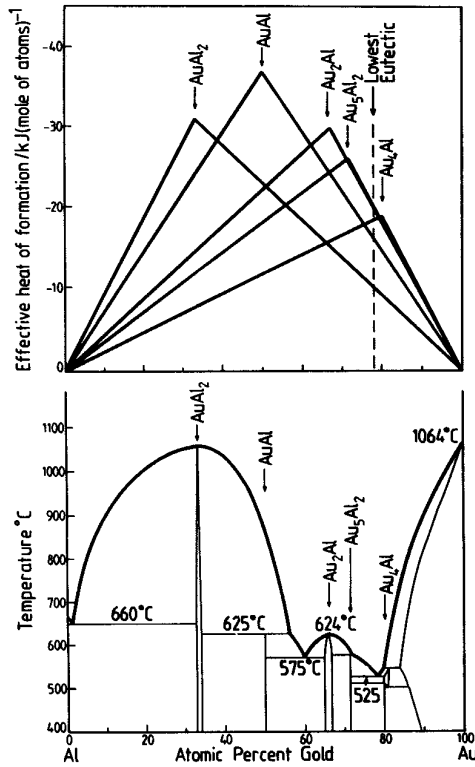
Figure 3: Phase diagram of Al-Au (a) and the heat of formation of the expected compounds (b). The straight lines connecting the data of the stoichiometric compounds to the corners of the diagram represent the effective heat of formation, as defined by Pretorius [22].

2.3 Influence of microstructure

The aforementioned physical models of the reaction rely on a very simple approach, describing the occurring phases as homogeneous layers, which are characterized by a few thermodynamic and kinetic parameters (see fig. 4a). There are many examples, particular in covalent materials, where this point of view is indeed a suitable approximation; and furthermore, for many applications growth of planar layers is an important goal. However, in at least as many other examples, the impression of a layered morphology is just an artefact of the analysis method and cannot bear a closer microscopic examination. Especially for metals, a more realistic description is often provided by fig. 4 b. Heterogeneous nucleation at tripel-junctions of the grain structure and transport along fast grain boundary paths produce a very rough morphology. In addition, local stress and its plastic relaxation or deviations of the vacancy density from equilibrium may play a role. The influence of the microstructure becomes particularly clear in cases, where the phase sequence or the reaction kinetics depends on a particular deposition method of nominally identical layer systems [26]. Grain boundaries inside nanocrystalline Zr were shown to play an important role for the amorphization reaction in Ni/Zr couples [27]. Furthermore, the microstructure controls the annealing of non-equilibrium vacancies and by that the kinetics of the reaction [28]. By emphasizing these effects, the present thesis takes the view point of
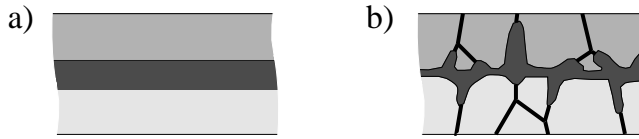
Figure 4: Interreactions seen from different points of view: a) 'macroscopic' view: homogeneous layers, b) microscopic view: 3D-morphology.

classical physical metallurgy, which has elucidated the connection of macroscopic properties to the arrangement and dynamics of structural defects.

The most obvious defects in thin films are grain boundaries. Hence, it is not surprising that their dominant effect on the low temperature reaction of metallic thin films was pointed out early [29]. In simple cases, the presence of grain boundaries will just accelerate the atomic transport through the product layer, which can be accounted for by an increased diffusion coefficient. But what happens if the grain structure itself is unstable during the reaction? Assuming the dominant transport along grain boundaries, the current through the product layer is estimated by

$$j = \frac{D_{\mathrm{GB}}\triangle c.}{w} \cdot \frac{2\delta}{r} \,, \tag{14}$$

where D_{GB}, $\triangle c$, and δ denote diffusion coefficient, composition variation across the product phase, and effective width of the grain boundary, further variables see fig. 5a. Let us assume that the grain size increases proportional to the layer thickness. Thus, we have for the layer growth

$$\frac{\mathrm{d}w}{\mathrm{d}t} \propto \frac{2\delta D_{\mathrm{GB}}\triangle c}{w^2} \,, \tag{15}$$

which yields a time exponent for the layer growth of 1/3 instead of the 1/2 expected for ordinary parabolic growth. If the grain size is connected to the layer thickness by a different power law, almost arbitrary time exponents for the layer growth may be predicted. For example, in the case of the technological important[3] $TiSi_2$, a time exponent of only 1/4 was attributed to considerable grain growth during the reaction [30].

A very impressive example for the importance of grain boundaries has been given recently by Kosevich et al. [31, 32] in a very detailed study on the interdiffusion of unsupported Ag/Pd bi-layers. In this case, the mixing of both components proceeds in a discontinuous mode as sketched in fig. 5b. Interdiffusion takes place along grain boundaries and mixing of the specimen volume is achieved in a discontinuous reaction by chemical induced migration of the boundaries as indicated in the figure. This way, a fast reaction is achieved although the volume diffusion is almost frozen at the low reaction temperature. It is quite obvious, that in this case any time exponent derived from a layer growth approach

---

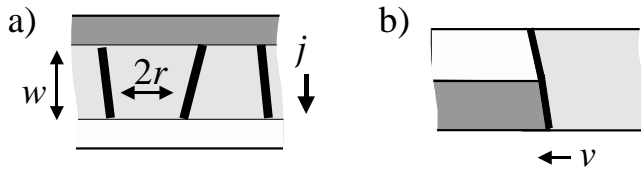[3]Drain and source contact of field effect transistors.

Figure 5: Influence of grain boundaries a) introduction of fast transport paths, b) volume transformation by grain boundary migration

becomes meaningless. Such severe transformations of the microstructure are by no means restricted to unsupported thin films, where no constraint is imposed by adhesion to the substrate. As will be demonstrated later in this thesis at the interdiffusion of Cu/Au, they may be induced by the size mismatch of the diffusing elements.

It is remarkable that thin film reactions often proceed very fast, much faster than could be understood by ordinary volume diffusion. In the case of nano-crystalline films, grain boundary diffusion is always an obvious explanation. However, there are also cases, where epitaxial growth of quasi-single crystalline layers is proven, but nevertheless unexpected fast diffusion is observed (see e.g [33] for Pd/Si). This can only be explained by other non-equilibrium defects accelerating the transport. During the formation of Ni_2Si silicide, Tu et al. [34] observed a significant composition gradient across the Ni_2Si layer, although this phase is in equilibrium strictly stoichiometric and long range ordered. The authors suggest that a vacancy supersaturation on the Ni sublattice might explain the observed asymmetry between Ni and Si diffusion and furthermore the increase of the overall reaction rate. Thus, it is indicated that the fast transport during the early reaction might force phases away from equilibrium to accelerate the reaction. Effects like that are more subtle and certainly not that obvious as the formation of new metastable phases. They are finally not proven yet.

2.4 Nucleation of product phases

Without doubt, a nucleation is required, whenever a previously non-existent phase should be formed. However, the question arises, whether nucleation will become the important step controlling the reaction kinetics or at least the microstructure of the transformed volume. Still in 1988, d'Heurle could point out that for interreactions between pure components driving forces are usually too high that noticeable nucleation barriers will hinder the formation of the primary product [35]. At that time only a few examples of significant nucleation processes were known, mostly regarding the formation of secondary silicides. However, since then the situation has remarkably changed, as several experiments with metallic reaction pairs have indicated the importance of heterogeneous nucleation for the formation of the primary product.

Surprisingly, the evidence for that arises from macroscopic calorimetric mea-
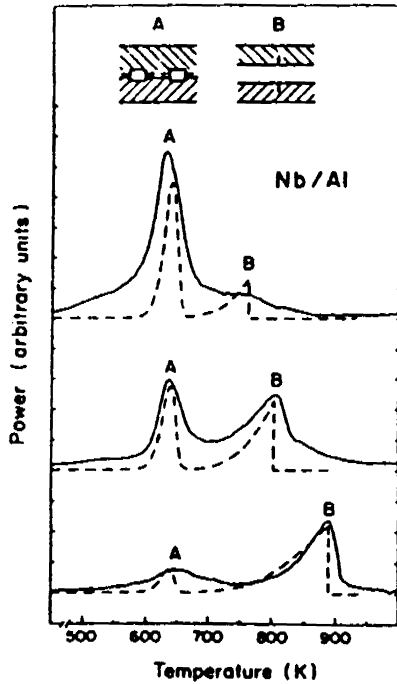
Figure 6: Thermograms obtained during the interreaction of Nb/Al layers, from Coffey et al. [36]. Dashed lines are calculated using the two stage reaction model. (layer thickness from top to bottom: Nb_{109nm}/Al_{34nm}, Nb_{98nm}/Al_{45nm}, Nb_{342nm}/Al_{158nm})

surements, where mixing reactions are noticed by characteristic heat releases. Even in cases where X-ray analysis or electron diffraction reveal a single product, two well distinguished exothermic peaks emerge in related thermograms. As the most clear example, thermograms of the Nb/Al interreaction are shown in fig. 6, as published by Coffey et al. [36]. Similar results have been published for Ni/Al, Ti/Al, Ni/a-Si, V/a-Si [37] and Al/Ag [38]. The systematic shift of the heat release from the first to the second peak with increasing layer thickness allows to relate peak A to an interfacial reaction and peak B to thickness growth. In order to explain the calorimetric measurements, Coffey et al. proposed a two-stage reaction as sketched in the upper part of fig. 6. At the first stage (A), nuclei are formed at heterogeneous nucleation sites and grow laterally until a dense layer is formed. During the subsequent stage (B) this layer grows in thickness, until the available pure material is consumed. According to this ansatz a quantitative model of the transformation rate was proposed as

$$\frac{dX_V}{dt} = \frac{dX_A}{dt} \cdot \frac{z_0}{z_{max}} + X_A \frac{D_l}{z} \cdot \frac{1}{z_{max}}, \tag{16}$$

where X_A, z_0, z_{max}, and D_l denote the interface fraction already covered by the product, thickness of the interfacial particles at coalescence, the maximal reaction width as defined by the layer thickness in the as-deposited state, and a suitable diffusion coefficient of the product layer, respectively. The first term on the

right hand side describes the nucleation stage and the second thickness growth. Assuming the nuclei as cylindrical disks, the coverage of the interface is described by a Johnson-Mehl-Avrami kinetics

$$\frac{dX_A}{dt} = 2n\pi r \cdot \frac{dr}{dt} \cdot \exp(-n\pi r^2), \tag{17}$$

where n stands for the area density of nucleation sites. As usual, the final exponential factor accounts for impingement of the growing nuclei. Both, diffusional transport through the product as well as lateral growth of the nuclei dr/dt are assumed to be thermal activated processes. This way, the dashed lines shown in fig. 6 are calculated. Required model parameters were determined by adapting simulated traces to the measurements. Obviously, the model reflects the essential features of the thermograms; remaining discrepancies may be addressed by geometrical refinements considering the interfacial roughness [39]. In addition, isolated $NbAl_3$ particles have been proven at the interfaces by electron microscopy [39], so that heterogeneous nucleation effects prior to the layer growth must be taken as a matter of fact.

On the other hand, the thickness at coalescence required to fit the experimental data amounts typically to a few tens of nanometer, so that the assumed two-dimensional growth of the nuclei has to be criticized. Also, grain boundary transport and the significant difference in the diffusivity of the initial reaction partners are neglected, although they probably control the nucleation. Hence, the model might experience further modifications as a consequence of detailed microscopic investigations.

These experiments demonstrate that nucleation is indeed an important reaction step controlling the kinetics, opposed to our intuitive expectation from a thermodynamic point of view. Naturally one has to ask for the reason which forces nevertheless significant nucleation barriers. In order to determine the shape of a nucleus and thereby its surface to volume ratio, conventional geometrical models used in the case of heterogeneous nucleation are certainly appropriate [35, 16], if the balance between different specific interface energies is taken into account by

$$\frac{\sigma_{\alpha\beta}}{\sin\omega_\gamma} = \frac{\sigma_{\beta\gamma}}{\sin\omega_\alpha} = \frac{\sigma_{\gamma\alpha}}{\sin\omega_\beta}, \tag{18}$$

where σ is an interfacial energy and $\omega_\gamma = \pi - \omega_\alpha - \omega_\beta$. For a definition of the remaining variables see fig. 7. However, quantitatively the different interfacial energies are hardly known so that rough estimates must be used. One point to notice here, is that the chemical contribution to the interfacial energy becomes negative in systems with strong mixing tendency. In consequence, the energy of the initial interface ($\sigma_{\alpha\beta}$ in fig. 7) is expected to be very low [16], which might explain, why homophase grain boundaries inside nano-crystalline layers become that effective as nucleation sites.
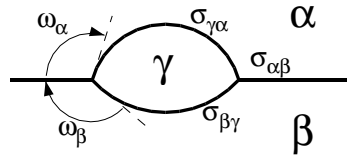
Figure 7: lens-shaped nucleus at the initial α/β interface.

Apart from these minor modifications, no principal difference in the surface contribution exists compared to solidification or decomposition reactions, that could explain the presence of nucleation barriers despite enormous driving forces of several 10 kJ/mol. Thus, it is suggested that only a fraction of the total free energy gain of compound formation is effective at the 'saddle point' of nucleation. To give an example, fig. 8 shows Gibbs free energies of the phases of the Ni-Al system as determined by CALPHAD methods [16]. The first equilibrium phase observed during the interreaction of Ni and Al is NiAl$_3$. A total free energy gain of 34 kJ/mol drives this reaction. But this total driving force is reduced to only 4 to 5 kJ/mol, if an fcc solution has already formed by intermixing when the equilibrium phase is nucleated.

In general the driving force may be significantly reduced by any precursor reaction proceeding prior to the formation of the equilibrium compounds. Often, the detection of these precursors are an experimental challenge, as compositional variations or metastable phases on the length scale of a few nanometer have to be determined. Even the apparently simple question whether a noticeable intermixing precedes the compound formation has not been definitely answered by experiment. Again, Ni-Al gives an instructive example. In early measurements using energy dispersive X-ray spectrometry with a spatial resolution of about 10 nm, Ma et al. [40] claimed to have observed an intermixing zone, but later, advanced analysis has evidenced the formation of a distinct phase in these early stages [41, 42], as will be discussed later in this thesis.

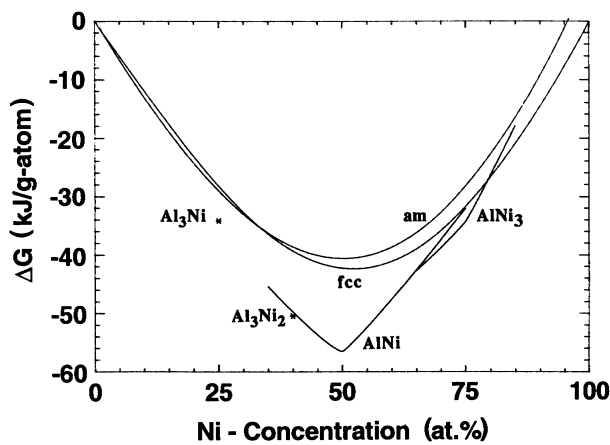From a very different point of view the driving force of nucleation was ad-

Figure 8: Gibbs free energies of phases in the NiAl system, after Bormann [16]

dressed by Desré and Yavari [43] and by Gusak [44], who independently considered the free energy change caused by a nucleus formed in a composition field of a steep gradient. Both postulate that the driving force to form a nucleus vanishes, if the composition gradient exceeds a critical limit. The concept was also generalized to determine equilibrium shapes of the nucleus [45].

However, a careful consideration shows that the derived critical gradient results from severe constraints imposed on the internal structure of the nuclei. Let us study for instruction the treatment proposed by Gusak. To avoid complicated geometrical factors, a nucleus of cubic shape is embedded into a steep composition field. Gusak considers the nucleus to form by a polymorphic transformation, i.e. the structure is transformed without changing the local composition. Schematic free energy curves in relation to the composition field are depicted in fig. 9. Because of the compositional variation inside the nucleus, nucleation is driven by a negative contribution to the energy change stemming from the central part of the nucleus (light grey) and hindered by a positive contribution from the outer parts (dark grey). Assuming that the nucleus is centered at a composition c_0, a quantitative formulation of the related energy change is given by[4]

$$\triangle G = 24\sigma r^2 + 4r^2 \int_{-r}^{r} [g_c(c(z)) - g_s(c(z))]dz\,, \tag{19}$$

where $2r$, σ, g_c, and g_s denotes the edge length of the nucleus, average interface energy and the Gibbs free energy per volume of compound and solution (negative quantities), respectively. If the free energies are expanded at the stoichiometric composition c^*, Eq. 19 transforms to

$$\triangle G = 24\sigma r^2 + 4[2\triangle g + (g_c'' - g_s'')(c_0 - c^*)^2 - 2g'(c_0 - c^*)]r^3 + \frac{4}{3}(g_c'' - g_s'')(\nabla c)^2 r^5\,, \tag{20}$$

where $\triangle g$ denotes the change of free energy for the polymorphic transformation at stoichiometric composition. The driving force $-\triangle G$ is maximized for a nucleus centered at $c_0 = c^* + g_s'(g_c'' - g_s'')$, so that we have finally

$$\triangle G = 24\sigma r^2 + 4[\,2\triangle g - g_s'^{\,2}/(g_c'' - g_s'')\,]\,r^3 + \frac{4}{3}(g_c'' - g_s'')(\nabla c)^2 r^5\,. \tag{21}$$

The positive first and third term on the RHS destabilize the nucleus. According to their different power in r, they hinder the formation of a nucleus for

$$r < r_1^* = -\frac{6\sigma}{2\triangle g - g_s'^{\,2}/(g_c'' - g_s'')} \tag{22}$$

and

$$r > r_2^* = \sqrt{-\frac{3(2\triangle g - g_s'^{\,2}/(g_c'' - g_s''))}{(g_c'' - g_s'')(\nabla c)^2}}\,. \tag{23}$$

---

[4]In the original treatment of Gusak, additional gradient energy terms according to Cahn and Hilliard were taken into account, but are negligible for the final result.
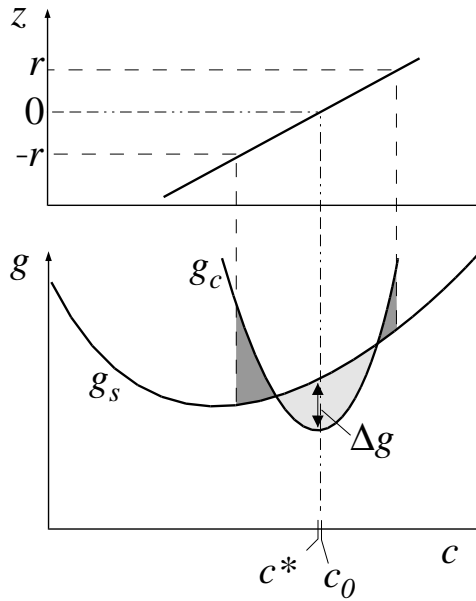
Figure 9: Schematic composition profile (top) and free energy curves (bottom) defining a nucleus of size $2r$ in a steep composition gradient.

If ∇c gets high enough that r_2^* falls short of r_1^*, a stable nucleus can no longer be formed, no matter what its size be. Thus, the formation of the product phase is suppressed by thermodynamic reasons, until the initially sharp composition transition at the interface is sufficiently smoothed by interdiffusion.
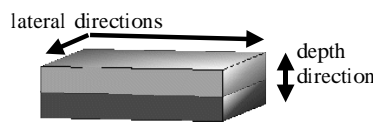
At first sight, this ansatz seems to be very attractive, as it might explain the suppression of phases in early reaction stages. However, one must not overlook that the disappearance of the driving force is related to the assumption of a polymorphic transformation, which does not allow any compositional adjustments inside the nucleus to optimize the gain in free energy. This becomes immediately clear in fig. 9. If the composition inside the nucleus is equalized to c_0, a gain in energy is always achieved no matter what the composition gradient might be. Desré and Yavari impose a less restrictive condition on the formation of the nucleus in allowing a compositional equalization at least normal to the initial gradient. They justify this restriction by the reduced diffusivity of the product phase which hinders diffusion in normal direction. However, arguing this way neglects that in classical nucleation theory, a nucleus is never formed by diffusion but by random composition fluctuations.

In conclusion, we have to state that up to now no nucleation theory is known for the interreaction of two materials. The dilemma lies in the fact that classical nucleation theory relies on a metastable equilibrium to determine nucleation rate and also shape and size of the nucleus. However, such an equilibrium is never established in the interreaction of two materials, where the composition profile at the interface develops continuously by diffusion.

3   Methods of microscopic analysis

The physical phenomena discussed throughout this thesis develop on a length scale of several nanometers so that their investigation requires the application of advanced experimental methods. Often, X-ray diffractometry or calorimetry have been applied to determine the kinetics of thin film interreactions. These methods need comparatively little effort in specimen preparation. However, it must not be overlooked that always an a-priori model is required as a base for data interpretation. Thus, in a strict sense, the reaction mechanism is not concluded from the measurements but merely postulated as a working hypothesis. Because of a lack of sufficient microscopic information, a simple, layered reaction geometry was often assumed in the past, which later turned out to be inadequate. In addition, depth profiling techniques such as Rutherford backscattering (RBS) or secondary ion mass spectrometry (SIMS) are frequently used. These techniques have a rather high depth resolution normal to the prepared interfaces. However laterally, they do not yield sufficient information, since the lateral resolution is very limited as indicated by the numbers allocated in table 1. Thus, microscopic processes, such as grain boundary transport, formation of of small nuclei, or recrystallization are hardly detected.

Direct information on the microstructural development will be only provided by microscopic imaging or analysis, that yields spatially resolved data in at least two independent directions. The increased effort in often very tedious specimen preparation is well justified by the very detailed information obtained. As a first choice, the various methods of transmission electron microscopy are considered. High resolution electron microscopy (HREM) yields the structural information to understand the processes on the atomic scale. In addition, chemical information is obtained by various methods of analytical electron microscopy. These methods are usually based on the inelastic interaction of electrons with matter, which is determined by dedicated detector systems via the generated X-rays or the energy loss of the electron beam. Besides, also the scattered electron intensity may be directly interpreted in terms of local specimen composition. This idea forms the

	spatial resolution	
	depth	lateral
RBS	10 nm	~
SIMS	2 nm	200 nm
Analytical Electron Microscopy	1 nm	1 nm
Atomprobe Tomography (TAP)	0.2 nm	0.5 nm

Table 1: Typical spatial resolution of common analytical methods.

basis of the Z-contrast microscopy, which we will have to discuss in more detail below. Transmission microscopy uses very thin electron transparent specimens, so that beam broadening inside the specimen, which severely limits the resolution in the case of conventional scanning electron microscopy, can be almost neglected. In consequence, the spatial resolution of analysis is determined by the size of the electron probe. Using modern instruments with field emission sources, this size certainly reaches the 1 nm range; in the case of so-called dedicated STEMs even atomic resolution is achieved [46].

In spite of these unquestionable advantages, one must not neglect that electron microscopy is in principle a two-dimensional technique. The specimen volume is always projected onto a two-dimensional image plane, which has severe consequences to the accuracy of analysis. As soon as microstructural features become smaller than the specimen thickness of 10 to 20 nm, they can only be resolved, if they are perfectly aligned along the electron beam. Thus, analytical electron microscopy can be certainly applied to planar quantum well structures obtained in the case of covalently bound semi-conductors. But, if a three-dimensional, very fine grained morphology should be investigated, it will be almost impossible to distinguish in the image projection a chemical intermixing at a planar interface (fig. 10a) from a chemically sharp but structurally rough surface (fig. 10b).

Beside electron microscopy, field ion microscopy is a well established tool of physical metallurgy, which yielded in the past important data to understand decomposition and segregation processes in alloys. Analytical field ion microscopy does not suffer from the two-dimensional projection, since it is based on a local chemical analysis of the specimen surface. The specimen volume is made accessible by the continuous removal of the surface material. In the last decade, the technique made a substantial progress by the introduction of so called 3D-atomprobes, which became possible by the development of spatially sensitive time of flight detectors [47, 48, 49]. Detailed information on field ion microscopy and the possibilities of 3D-analysis may be found in recent text books and reviews [50, 51].

The principle of such an instrument is illustrated in fig. 11. Needle shaped specimens of extremely small tip radius are investigated. Applying high voltage pulses, single atoms are removed from the specimen by field evaporation and detected after a flight path of about 50 cm at a position sensitive detector. The evaporated atoms are chemically identified by time of flight spectroscopy. In
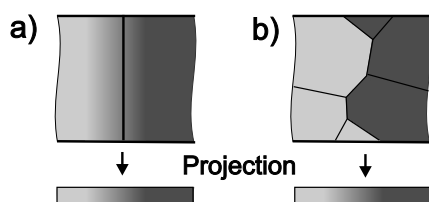

Figure 10: Two different structures yielding same chemical mapping in electron microscopy: a) intermixing, b) rough interface.
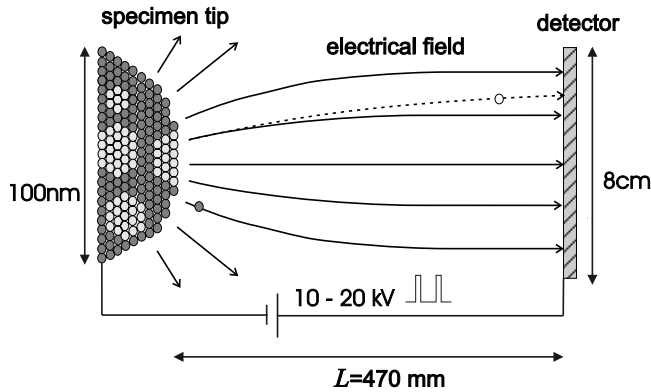
Figure 11: Principle of 3D atomprobe.

addition, the hitting position on the detector is recorded. The flight path of the evaporated ions is well approximated by a point projection using a projection center inbetween those of the stereographic and the central projection (see fig. 12). Thus, the lateral position of the atom at the specimen surface is easily determined from its hitting position. The depth scale along the tip axis is concluded from the number of detected atoms, regarding the atomic density inside the specimen.

This way, a typical measurement yields the time of flight (TOF) and 3D position data of 10^6 atoms representing a volume of roughly $15 \times 15 \times 100 \, \text{nm}^3$. The accuracy of the lateral positioning is found to be in the $0.5 \, \text{nm}$ range. In depth direction along the tip axis, in many favorable cases atomic resolution is achieved, which allows to determine even the stacking sequence of differently occupied lattice planes in ordered superalloys [52]. Its outstanding feature to analyse and to position single atoms makes the 3D atomprobes especially suitable for the chemical analysis of nanocrystalline metallic films. However, the positioning accuracy is not sufficient to obtain detailed structural data, and furthermore, the requirement to prepare needle-shaped tips of sufficient mechanical stability converts the atomprobe analysis of thin film specimens into a challenge. The concomitant use of electron microscopy is therefore necessary to obtain structural information and to support the microscopic results by better statistics.

As the presented work especially addresses the microstructural development, a state-of-the-art nanoanalysis is most important. Therefore, the study of the material physical problems was accompanied by the refinement of experimental methods. A new 3D-atomprobe and instruments dedicated to the thin film preparation for field ion microscopy were constructed. Regarding analytical electron microscopy, an image analysis scheme was derived, which allows to determine composition maps inside the reaction zone from images taken under hollow cone illumination. In the following two sections these methical developments and setups by the author of this report are described and considered in more detail.
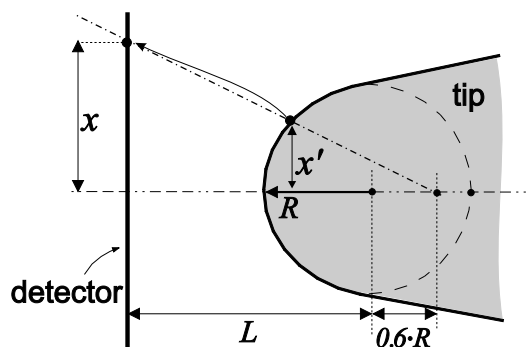
Figure 12: Reconstruction of the atom position by a point projection.

3.1 Chemical analysis by hollow cone illumination

Already the fundamental elastic interaction underlying conventional electron microscopy depends on the charge number and thus on the chemical nature of the scattering atoms, so that attempts to interpret image intensities in terms of composition are quite obvious. But owing to dynamical diffraction, the contrast caused by local variations of specimen orientation or thickness is usually much stronger than the desired mass contrast, so that very controlled specimen and imaging conditions are needed to obtain a reliable analysis. Therefore, early attempts of chemical analysis relied on electron probe scanning techniques, where annular ring detectors allow to sample electrons scattered at high angles. This way coherent diffraction effects are largely suppressed. The technique attracted considerable attention since sufficiently fine electron probes became available to produce Z-contrast images in atomic resolution [46]. On the other hand, the signal-to-noise ratio of scanning methods is notoriously bad and the quantitative understanding of the image intensities is still discussed.

In the nineties of the last century the so-called chemical imaging introduced by Ourmazd and co-workers [53] became an exciting alternative. In this case high resolution phase contrast images are used, which avoids the disadvantages of scanning techniques. The experimental fringe pattern of an area of unknown composition is compared to templates determined at calibration points of known composition. For that, specialized projection algorithms have been developed [53, 54, 55]. In the case of quantum well structures, which show an ideal quasi-single-crystalline structure with very low defect density, a reliable analysis was achieved. By contrast, the metallic thin films investigated in this work have a nanocrystalline microstructure with much higher defect densities which hinders the application of chemical imaging.

Therefore, based on own early work [56, 57] and experiments described in literature [58], an imaging and interpretation method was developed which com-

bines the advantage of the scanning mode Z-contrast with direct imaging. The method can be applied to nanocrystalline or even amorphous layers. Provided systems of sufficient mass contrast, a chemical sensitivity of a few at% and a spatial resolution in the one nanometer range [59] is achieved. These features are all the more remarkable, as the chemical information is acquired without any additional detector equipment.

3.1.1 Hollow cone illumination

In order to get a direct Z-contrast image of the specimen, electrons that are scattered by large angles have to be collected by the objective lens. As the aperture angle of electron optical lenses is very limited, this cannot be achieved with on-axis illumination. Instead, the specimen is illuminated along a hollow cone as sketched in fig. 13. By suitable control of the microscope's tilt coils, the electron beam is bent twice above the specimen and furthermore the bending point (B) rotates with a typical frequency of 10 Hz. This way, an incoherent illumination cone is achieved on the time average. Cone half angles θ up to about 150 mrad are realized after minor modifications of the circuitry of the microscope[5].

Using this illumination, high angle hollow cone dark field (HCDF) images are obtained, which differ significantly from ordinary bright or dark field images. This is demonstrated by the image sequence in fig. 14 [60] (A further impressive example concerning the contrast of small precipitates is published in [57]). A cross-section through a Cu/Au layer deposited on a single crystalline Cu substrate is shown, imaged with four different illumination angles. The specimen thickness increases roughly from the upper right to the lower left corner. With increasing cone angle, dynamical orientation and thickness contrast is suppressed and the
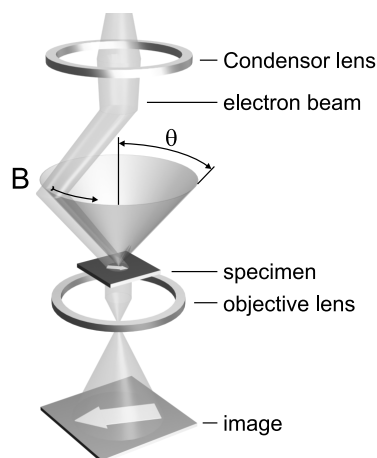
---

[5]Philips EM 420 ST

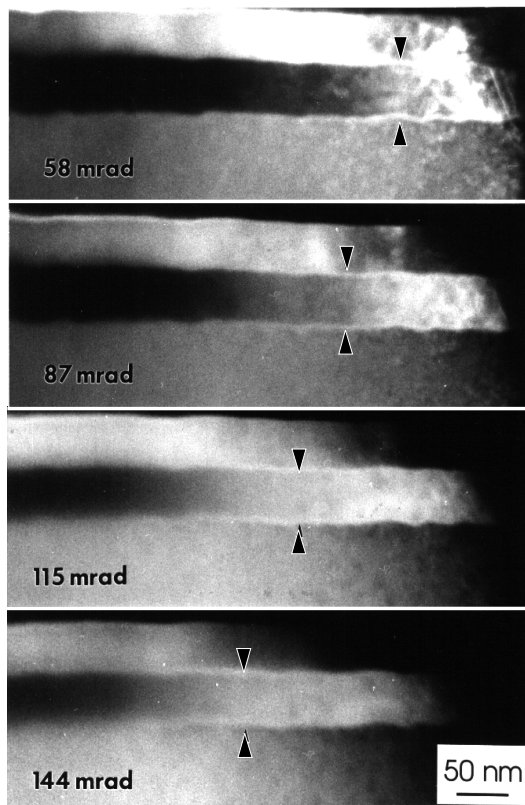Figure 13: Principle of hollow cone illumination.

Figure 14: Cross section of a Cu/Au/Cu sample as observed in HCDF images. The four micrographs show the same specimen area imaged with different cone angles. Foil thickness increases from the upper right to the lower left corner. The lower Cu layer is single-crystalline, while the Au and upper Cu layer are polycrystalline.

mass contrast between Cu and Au becomes emphasized. The intensity on the nanocrystalline Cu layer approaches that of the single crystalline substrate. In each metal, at first the intensity increases with the foil thickness, until it reaches a maximum. The position of the maximum shifts with the cone angle toward larger thickness. However, as the intensity maximum is reached in Au earlier than in Cu, a single contrast inversion is observed for all cone angles; Au, as the element of higher charge number, appears brighter than Cu in thin specimen areas, whereas in thick regions the reversed relation is observed. At specimen areas, where the contrast between pure Cu and Au almost disappears, the interface is remarkably emphasized by a brighter contrast line (marked by arrowheads).

3.1.2 Quantitative contrast description

A chemical interpretation of image intensities is only possible, if a quantitative contrast model is available. Therefore, experimental HCDF images were evaluated by densitometry. It was demonstrated, that the discussed image features are reproduced by an incoherent multiple scattering model; during their path through the specimen, the beam electrons are scattered several times in localized, independent collisions. If empirical high angle scattering cross sections are used to describe the probability of a single collision, even a quantitative model

is achieved [59]. The mathematical formulation is based on an early formulation by Goudsmit and Saunderson [61]

$$\frac{I_\vartheta(t)d\Omega}{I_0} = \frac{d\Omega}{4\pi} \sum_{n=0}^{\infty} (2n+1)P_n(\cos\vartheta) \exp\left(-\frac{t}{\lambda}\right) \left[\exp\left(\frac{t\,a_n}{\lambda}\right) - 1\right], \qquad (24)$$

where ϑ, t, $d\Omega$, I_0, P_n, λ, and a_n denote illumination angle, foil thickness, solid angle, intensity of the incident beam, Legendre polynomial of n-th order, mean free path of the beam electrons, and the coefficient to n-th order of the expansion of the cross-section in terms of the P_n, respectively. The parameters λ and a_n depend on the scattering material.

As independent collisions are assumed, the scattering in a binary alloy is easily deduced from the behaviour of the pure components. The probability for a collision at a given element is determined by its volume density and total cross section. Thus, the image intensity $I(t, c)$ is well predicted as a function of foil thickness and local composition, if λ and a_n are calculated from the data of the pure elements A and B according to

$$\lambda = \frac{N_V^A \lambda^A + N_V^B \lambda^B}{N_V} \qquad (25)$$

$$a_n = N_V \lambda \left[(1-c)\frac{a_n^A}{N_V^A \lambda^A} + c\frac{a_n^B}{N_V^B \lambda^B}\right], \qquad (26)$$

where N_V, N_V^A, N_V^B, and c denote the atomic density of the alloy, and the pure components and the atomic fraction of component B, respectively.

To determine scattering parameters of the pure elements, model curves are adapted to experimental intensity profiles. In order to reduce the infinite number of free parameters given by the series of expansion coefficients, we pre-define

$$a_n := \exp\left[-\left(\frac{n}{b}\right)^\gamma\right], \qquad (27)$$

where b and γ are material constants. Equation 27 is inferred from the behaviour of Wentzel type [62] cross sections. Thus, the scattering properties of component i are characterized by the remaining three parameters b^i, γ^i and λ^i. The first two determine the angular dependence of scattering and the last one the total cross-section. Numerical examples for three noble metals are compiled in tab. 2.

The important prerequisites for a chemical analysis are intensity composition maps, which are readily calculated with the presented formulas as shown in fig. 15 for the example of a Cu-Au alloy at an illumination angle of 144 mrad. The image intensity is plotted versus the composition for different thicknesses. In very thin specimens, the direction of the contrast follows the intuitive expectation from the different atomic numbers. In agreement with the experimental micrographs in

Cu			Ag			Au		
λ / [nm]	b	γ	λ / [nm]	b	γ	λ / [nm]	b	γ
6.0	58	0.87	5.5	40	0.90	4.8	25	0.91

Table 2: Model parameters to describe the high angle scattering cross section. Compared to a previous work [59] some parameters have been modified to improve the description over an extended range of cone angles in the thin foil regime [63].
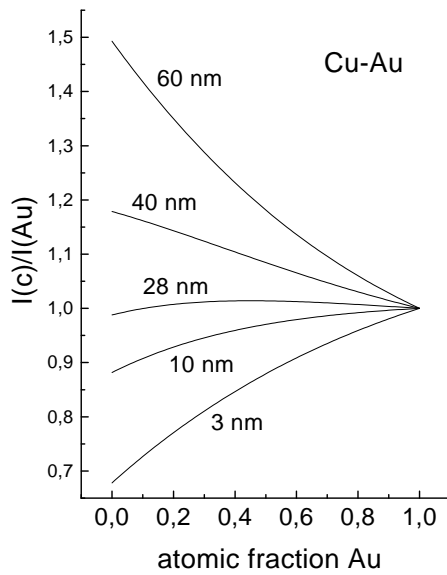

Figure 15: Chemical contrast of a Cu-Au alloy for several foil thicknesses calculated by the incoherent multiple scattering model.

fig. 14, a contrast inversion is predicted, with vanishing contrast at about 30 nm. Remarkably, at this thickness, an alloy is predicted to have a slightly higher intensity than both pure components.

From a theoretical point of view, the ansatz of incoherence must certainly be discussed into more detail. The experimental results are ambiguous regarding this aspect: Thickness oscillations which are expected from coherent diffraction vanish completely, but low-indexed specimen orientations are distinguished by an increased intensity, which is certainly not understood by isolated electron-atom collisions [59]. Thus at present, the incoherent multiple scattering model must be understood as an useful approximation, which allows to derive convenient formulas for image interpretation. Theoretical development to include thermal diffuse and inelastic scattering into electron optical simulations is actually done by Rose and coworkers [64].

On the other hand, the presented model describes most features of experimental images and yields reasonable quantitative analysis results. Even the
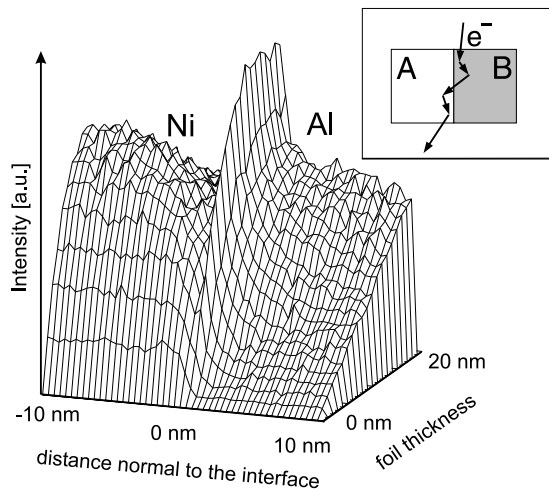
Figure 16: Contrast at an interface between Ni and Al. Result of a Monte Carlo simulation of incoherent scattering. The inset shows a schematic path of an electron multiply scattered at the interface.

aforementioned pronounced intensity at the layer interface is explained by the ansatz of independent collisions. This is proven by a Monte-Carlo simulation of electron scattering, where the free path and the scattering angle is chosen randomly, according to the probability defined by the scattering cross section. Thus, the Monte-Carlo model is equivalent to the analytical model. The result for an interface between Ni and Al, two elements with a similar atomic contrast as Au and Cu, is shown in fig. 16. During their path through the specimen, electrons at the interface 'see' an apparent alloy. As, at the thickness of contrast inversion, an alloy will produce a higher intensity than both elements, it is not surprising that the interface appears indeed with a bright contrast line.

3.1.3 Experimental examples

Using the described illumination conditions and the introduced model for image interpretation indeed a local chemical analysis is obtained. This shall be demonstrated by the interdiffusion at an Ag/Au interface [65]. A cross-section micrograph of a specimen is shown in fig. 17. Because of the very small stacking fault energies (σ_{SF}(Ag)=40 mJ/m², σ_{SF}(Au)=20 mJ/m²), a high density of coherent twin boundaries are observed in the conventional bright field image. However, after orienting the specimen to kinematic conditions in on-axis illumination, the hollow cone illumination will completely suppress these diffraction contrasts, so that they no longer disturb the chemical evaluation. (See the corresponding HCDF image in the inset). As the image intensity depends on the local composition as well as on the specimen thickness, an analysis is only possible, if the specimen thickness is known. This difficulty is overcome by choosing calibration points outside the diffusion zone, where the composition is known, as sketched in fig. 18. This way, even an eventual selective etching during the specimen preparation is detected. Between the calibration points a linear thickness variation is assumed. The typical error made by this assumption can be estimated in ad-
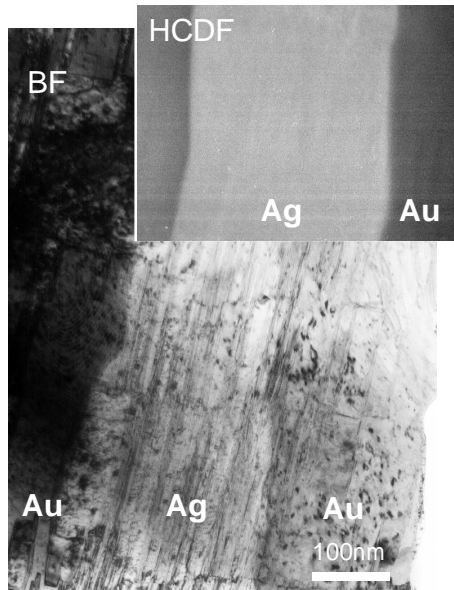
Figure 17: Cross-section image of Ag/Au multilayer. The parallel line contrasts stem from lattice twins. In addition, irradiation defects caused by ion milling are visible as black dots. The HCDF image shown in the inset was taken at a thicker area, where Ag appears brighter than Au.
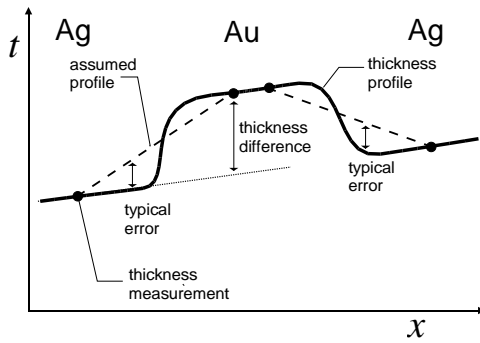

Figure 18: Schematic thickness profile normal to the layers. The thickness is measured at calibration points at areas of pure Ag and Au, inbetween a linear variation is assumed as indicated by the dashed lines.

dition. Very thin specimen areas with a relative thickness variation below 10% are selected for the quantitative analysis. Experimental composition profiles are shown in fig. 19 for three different stages. The determined profiles agree with the thick film solution

$$c(x,t) = \frac{1}{2}\operatorname{erfc}\left(\frac{x}{2\sqrt{Dt}}\right)\,, \tag{28}$$

As is indicated by the solid lines. A diffusion coefficient of $8 \cdot 10^{-20}\mathrm{m}^2/\mathrm{s}$ is determined at $350\,^{\circ}\mathrm{C}$, which agrees well with the extrapolation of the available literature data [66, 67, 68, 69]. Regarding possible applications the chemical and spatial resolution of the method are a point of interest. Corresponding quantitative estimates have been worked out in [59].
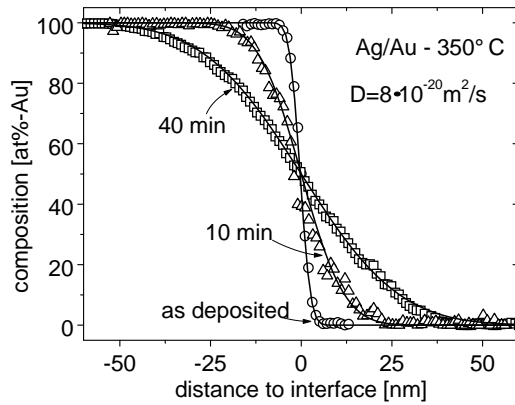
Figure 19: Microscopic composition profiles determined by HCDF imaging at Ag/Au interfaces in the as deposited state and after 10 and 40 min annealing at 350 °C.

3.2 Atomprobe tomography at thin film interreaction couples

Since its invention by E. W. Müller in 1951, field ion microscopy, especially *analytical* field ion microscopy, has been established as a valuable tool in surface physics and physical metallurgy. Owing to its high resolution chemical analysis, the method could solve several critical problems of reaction kinetics [50]. However, early analytical instruments, so called atom probes, were equipped with a single time-of-flight detector to perform a one-dimensional analysis along a specimen cylinder of a few nanometer in diameter. Only some 10^4 atoms were counted during a typical measurement, so that the statistical significance of the data always was very limited. This situation has recently changed dramatically by the development of two-dimensional detectors [47, 48, 49], which allow to register a much larger specimen volume and to improve the lateral resolution at the same time. By a reconstruction of the tomographic data, the 3D-distribution of the atoms inside a volume of typically $15 \times 15 \times 100\,\mathrm{nm}^3$ is determined in an accuracy that was not achievable before.

3.2.1 New 3D atom probe in Göttingen

In order to take advantage of this development, a new 3D atom probe was constructed at the 'Institut für Materialphysik' in Göttingen. A schematic drawing of the instrument is shown in fig. 20a. Its design is based on the tomographic atomprobe (TAP) detector developed by Blavette and coworkers [48]. To obtain a robust instrument, standard ultra high vacuum components are used and the amount of mechanics inside the vacuum is kept at minimum. By a five-fold load lock and an intermediate storage chamber, specimens can be exchanged quickly to obtain a high measurement throughput. All chambers are isolated by plate valves and pumped independently by turbo molecular pumps. A high voltage pulser to produce the evaporation pulses was build around a commercially available tran-

a)

Specimen storage chamber

Fast entry load lock

TAP Detector

47 cm

Specimen stage

10°

20 cm

Measurement chamber

b)

Cooling shroud

4mm

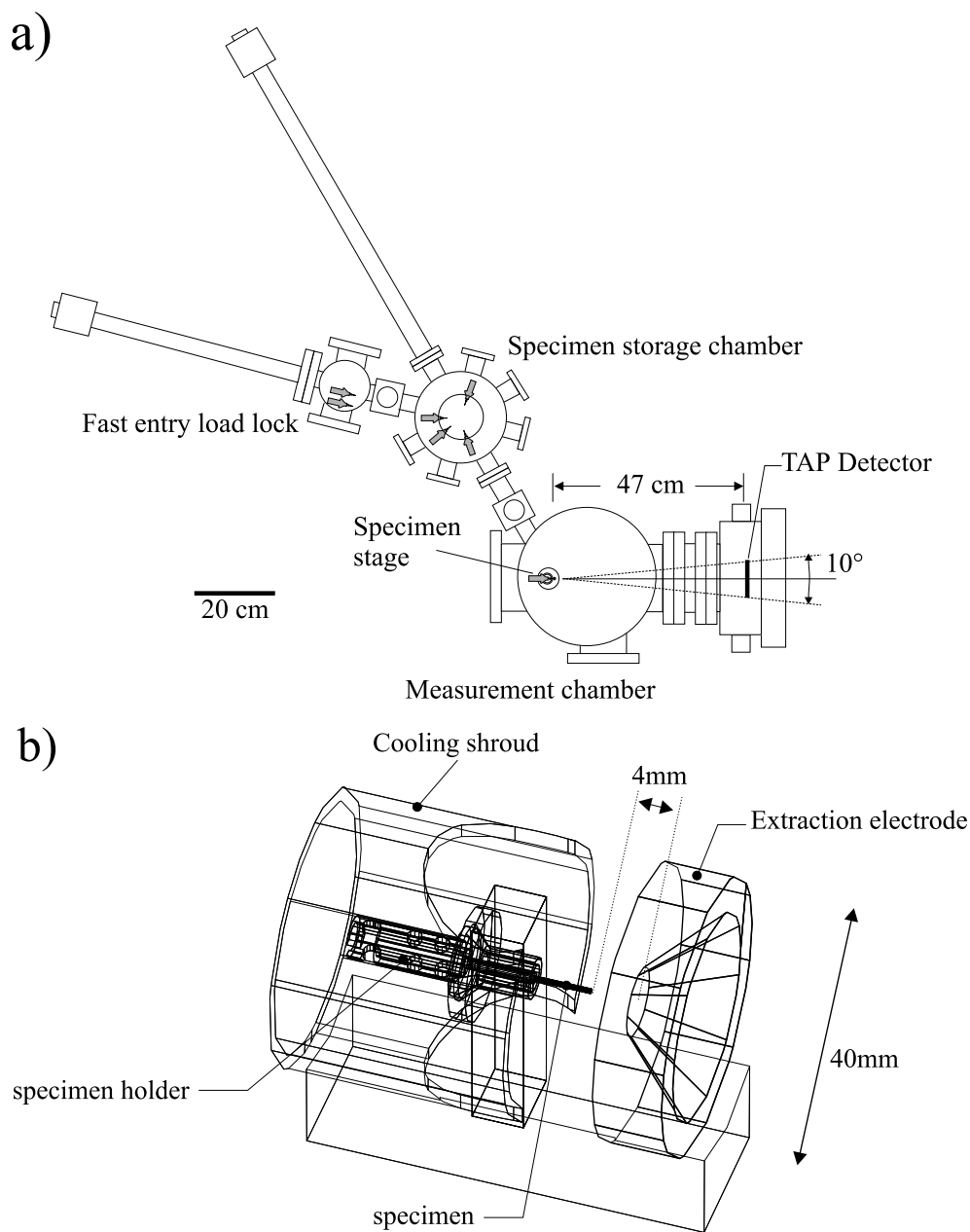Extraction electrode

specimen holder

40mm

specimen

Figure 20: Layout of the new 3D atomprobe at the 'Institut für Materialphysik' in Göttingen a) top view of the complete vacuum system, b) geometry of the specimen stage (inner diameter of the conical electrode bore: 4 mm, tip to electrode distance: 4 mm)

sistor switch[6]. Base and pulse voltage are automatically controlled during the measurement to keep the data rate of counted atoms per high voltage pulse constant. Further important technical data of the instrument are compiled in table 3.

background pressure	
measurement:	$5 \cdot 10^{-8}\,\mathrm{Pa}$
specimen storage:	$5 \cdot 10^{-7}\,\mathrm{Pa}$
minimum specimen temperature:	$\approx 25\,\mathrm{K}$
base voltage:	$0 \ldots 20\,\mathrm{kV}$
pulse voltage:	$500 \ldots 5\,\mathrm{kV}$
pulse rate:	$2000\,\mathrm{Hz}$
data rate:	$50\,000 \ldots 200\,000\,\mathrm{atoms/h}$

Table 3: Technical data of the 3D atom probe at the 'Institut für Materialphysik' in Göttingen.

The specimen stage of the instrument is shown in fig. 20 b. Field evaporation is triggered by negative pulses applied to an extraction electrode in front of the specimen to improve the mass resolution. The geometry of the electrode follows a published design [70]. Using a tip to electrode distance of 4 mm and an inner electrode diameter of 4 mm, the requirements to the accuracy of tip positioning are only moderate. After aligning the specimens in standardized holders outside the vacuum system, any mechanical adjustment inside the chamber becomes obsolete, which makes measurements very easy.

3.2.2 Preparation of thin films for analytical field ion microscopy

Compared to conventional specimens made from bulk materials, the atomprobe analysis of thin film reaction couples requires particular effort, since the layer interface of interest must be prepared into tips of at most 100 nm radius of curvature. The evaporation fields induce considerable mechanical stress during the measurement, so that the stability of the samples becomes the most crucial issue in improving the output of successful measurements. Several preparation methods are developed and applied, which produce different specimen geometries as sketched in fig. 21.

Since 1980 [71, 50], the deposition of one or several metallic layers on suitable substrate tips is known, but applied only rarely because of difficult specimen handling. For the presented studies, two different deposition techniques were applied, for which dedicated deposition chambers had been constructed. Clean
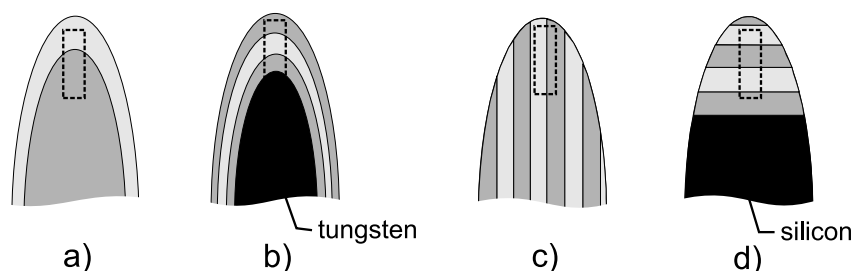
---

[6]Fa. Behlke

Figure 21: Specimen geometries obtained with different preparation methods. a) reaction couple of tip and deposited layer, b) multilayer deposited on tungsten substrate tip, c) tip cut lithographically out of a planar multilayer, d) multilayer deposited on the planar face of a silicon post. The analysed volume is indicated by a rectangle at the tip apex.

interfaces and a smooth layer morphology are very important to achieve the required stability.

a) To investigate the reaction between the substrate tip itself and a top layer, as indicated in fig. 21 a, an electron beam evaporator was attached to a field ion microscope dedicated to preparation [72]. Prior to coating, the substrates are field developed to a best image voltage of 8 to 9 kV, which yields a reproducible spherical shape and a clean surface. Without breaking the vacuum, deposition of the second material is started within 30 s after turning off the evaporation voltage. Maintaining a low background pressure (p $< 10^{-6}$ Pa) and a low growth rate of 1 to 2 nm/min are essential to obtain sufficient adhesion [72].

b) Thin films are deposited by ion beam sputtering on substrate tips, to study the reaction between several deposited nanocrystalline layers (fig. 21b). Substrates are usually made of tungsten, which has ideal properties for field ion microscopy and furthermore, a high melting point so that it does not take part in the studied reactions. As with the previous method, the substrates are pre-developed in a field ion microscope. Subsequently, they are transferred into a separate sputter chamber where the tips are cleaned by ion etching and subsequently coated. The geometric layout of the chamber is shown in fig. 22 [73]. Mounting the tips on a rotatable, water-cooled stage, a single ion beam produced by a Kaufmann ion source is sufficient for tip cleaning (1.) and for sputtering (2.) as well. Up to four different targets are attached to a water-cooled holder, which allows to switch between different materials within less than a second. Before deposition, the chamber is pumped to a base pressure better than 10^{-5} Pa. Substrates are cleaned by a 500 V Ar beam of 1 mA/cm^2 intensity for 20 s. Layers are deposited with a growth rate of 10 nm/min under an Ar partial pressure of 2×10^{-2} Pa.

As the major axis of the analyzed volume is approximately aligned along the tip axis, a reaction width of up to 50 nm normal to the interface is easily
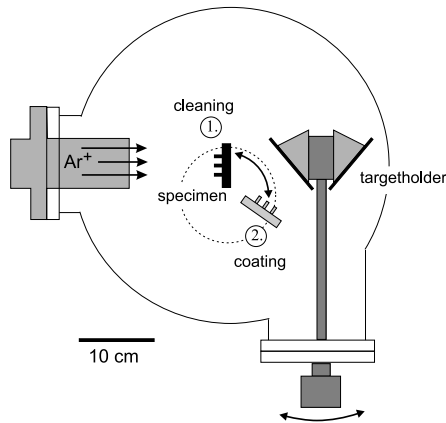
Figure 22: Geometry of the ion beam sputter chamber used for tip preparation

investigated in the specimen geometries shown in fig. 21 a and b, which is a major advantage of the direct deposition on substrate tips. However, other experimental methods and many technical applications deal with planar multilayers. Thus, it is always a matter of concern, whether results obtained at the curved tip coatings may be generalized to those planar systems.

c) To avoid this difficulty a lithographic preparation method was developed which allows to prepare FIM tips out of planar multilayer systems [74] (see fig. 21c). The method is based on early work on single layers of FeCr alloys published by K. Hono and coworkers [75]. Planar multilayers are deposited onto a soluble separation layer and coated by a photoresist. After exposure and development of the resist, tips are cut out by ion etching. For that, the chamber in fig. 22 is used with specimens fixed in position (1.). After solving from the substrate, tips are additionally sharpened to a radius of 50 to 100 nm by a focused beam of Ga ions, if required (see for details [76]).

To achieve the necessary field concentration at the tip apex, the radius to length aspect ratio of the tip must be at least about 1:100, so that lithographically cut specimens are always aligned parallel to the interfaces, as indicated in fig. 21c. Thus, with these specimens the TAP measurement is especially suited to determine lateral fluctuations. The measurement depth normal to the interfaces is limited to about 15 nm.

d) This latter limitation is overcome by a further method recently reported [77], which must be mentioned for the sake of completeness. Multilayers are deposited on the planar face of silicon posts of about $1 \times 1 \mu$m cross section. A final tip sharpening is then performed by a focused ion beam to obtain the geometry shown in fig. 21d, with a sufficiently small tip radius.

3.2.3 Atom probe analysis of thin film specimens

Atomprobe tomography has proven to yield reliable analysis data in many examples, where small precipitates are embedded into a matrix, see for example [52, 78, 79]. However, compared to the microstructures of those examples, layered thin film specimens are heterogeneous on a much coarser scale, which has severe consequences to the design and evaluation of experiments in cases where the layer materials are distinguished by a pronounced difference in the evaporation field strength (see also [42]).

i) During the measurement, the evaporation rate is usually kept constant, controlled by the tip voltage. If in one of the geometries shown in fig. 21 a, b, or c, a layer of high evaporation field strength is deposited on top of a material of lower field strength, the measurement gets in an unstable situation when the interface is reached. As soon as the easily evaporating material becomes uncovered, the data rate increases dramatically. Often, this cannot be compensated by a quick reduction of the tip voltage, resulting in the specimen's break-off. Thus, if possible, the deposition of the layer materials should always be planned in the order of decreasing evaporation field strength to improve the probability of successful measurements.

ii) In order to obtain a reliable reconstruction of the atom positions, it is advantageous to keep the evaporation rate homogeneous along the specimen surface during the measurement. This requirement is best achieved by a careful pre-development of the substrates, which shapes the tip to obtain an iso-field surface. Provided that the deposited layers do not become too thick, this property is transferred to all interfaces of the deposited multilayer. During the subsequent measurement, the iso-field surface is always maintained, so that a new layer with different evaporation properties becomes completely uncovered at once. In consequence, the curved geometry in fig. 21b is more favorable than the planar geometry of fig. 21d, if materials with very different evaporation properties shall be analyzed.

iii) For the reconstruction of the atom distribution based on the point projection shown in fig. 12, the actual tip radius must be known. In the established reconstruction scheme introduced by Blavette and coworkers [80], the radius is determined from the evaporation voltage V_e according to

$$R = \frac{V_e}{\beta F_e},\tag{29}$$

where β and F_e denote a geometrical factor of the order $5 \ldots 7$ and the evaporation field strength, respectively. Usually, βF_e is determined by calibration measurements and assumed to stay constant during the measurement. In the case of decomposed alloys this approximation is often well justified and yields reliable reconstructions. However, for thin film experiments, this practice may result in
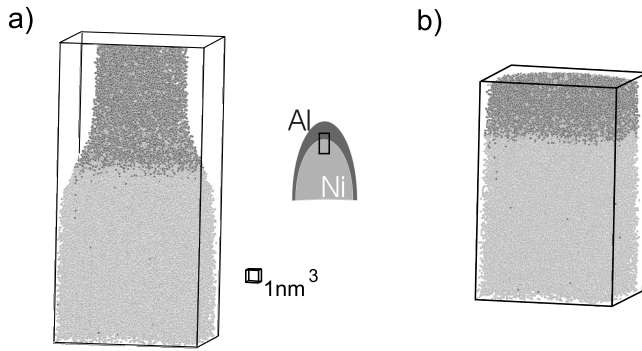
Figure 23: Atom probe tomography at an Al/Ni interface. Reconstructions based on Eq. 29 (a) and Eq. 30 (b).

severely distorted volumes as demonstrated by fig. 23, where the example of an Al layer deposited on a Ni tip is shown. Both materials differ significantly in their evaporation field strength (F_{Al}= 19 V/nm, F_{Ni} = 35 V/nm). If this variation is neglected and the parameters of pure Ni are used for reconstruction, a bottle-neck shape of the interface region is obtained, where inside Al, the lateral dimension is under- and the z-dimension along the tip axis severely overestimated. As the evaporation fields of intermetallics or alloys of intermediate composition are not known, this problem cannot be overcome using Eq. 29.

Instead, the tip radius may be estimated by the geometrical relation

$$\frac{\mathrm{d}R}{\mathrm{d}z} = \frac{\sin\gamma}{1 - \sin\gamma} \tag{30}$$

where γ is the shaft angle of the specimen. The expression Eq. 30 follows immediately from the geometric situation shown in fig. 24. This way, the reconstruction shown in fig. 23 b is obtained, where now correct dimensions are achieved also for the Al layer. In order to use Eq. 30, the initial radius and the shaft angle of the tip need to be known. These parameters can be obtained by electron microscopy. But it is also feasible to take them as free parameters. After reconstructing the volume, the evaporation field is calculated by a reversed version of Eq. 29, knowing the experimental voltage and the radius from the reconstruction. Initial radius and shaft angle are then adapted, until the evaporation fields known from calibration measurements are obtained inside the remaining pure material. This way, even the composition dependence of the evaporation field strength is determined from the experiment [42].
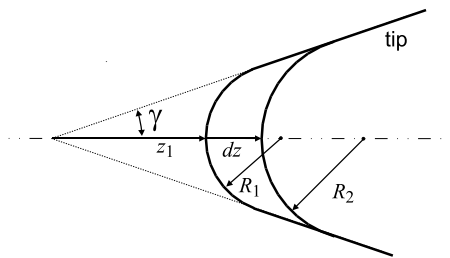

Figure 24: Truncated cone model of the tip. By field evaporation, the tip radius increases continuously with a rate determined by the shaft angle.

3.2.4 Influence of curved substrates

Although in principle the preparation of planar multilayers is possible, the necessary steps combining lithography and sophisticated ion cutting are very tedious and time consuming. Therefore, the majority of successful atomprobe measurements presented in this thesis were obtained at thin film specimens deposited on substrate tips. Often it is argued that reactions observed in such specimens will be very different from those in planar systems, because of the influence of the interface curvature. However, a straightforward quantitative consideration clarifies that the direct contribution to the driving force of the reactions is so small that it can be neglected in most cases.

Let us assume as the worst case the mere interdiffusion of two metals, so that the thermodynamic driving force per volume is quantified by

$$\triangle G_V \;=\; \frac{kT}{\Omega}[c \ln c + (1 - c)\ln(1 - c)] \tag{31}$$

$$\approx\; \frac{kT}{\Omega}\ln(1/2) \tag{32}$$

$$\approx\; 3 \cdot 10^5 \, \text{kJ/m}^3 \,, \tag{33}$$

at a reaction temperature of $500\,\text{K}$. Considering the formation of an incoherent nucleus, its critical radius is estimated to

$$R = \frac{2\sigma}{\triangle g_V} = 5\,\text{nm} \,, \tag{34}$$

where a specific interface energy of $750\,\text{mJ/m}^2$ is assumed. Thus, even in this somewhat unrealistic case — in the studies presented later, the driving force is much higher and early product phases probably form coherently — the radius of a nucleus is at least one order of magnitude smaller than the tip radius.

Furthermore, one has to keep in mind that in most experiments the reaction width is considerably smaller than the tip radius. And finally, the edge density at the substrate surface is not very different from that expected for conventional planar substrates. Usually, a low-indexed set of lattice planes is located at the apex of the substrate tip, so that a flat, terminating plane of about $10\,\text{nm}$ diameter is found inside the analyzed volume. In the case of a planar substrate, a comparable edge spacing of $10\,\text{nm}$ results already from a misorientation of only one degree. In consequence, the author believes that the curvature of the interface will not influence the observed reactions directly. However, their is certainly an indirect influence, as the shape of the substrate and the deposition geometry will control the initial microstructure and by that also the reaction mechanism.

3.2.5 Experimental examples

Applications of the giant-magneto-resistance (GMR) in metallic films attract considerable attention, because they offer the possibility to improve data storage and magnetic sensoric. Beside obvious parameters such as thickness and layer sequence, the magneto-resistivity certainly depends on microstructural features like interface roughness or pinholes through the layers. This becomes especially clear, if the behaviour under thermal annealing is studied. The thin film analysis by atomprobe tomography yields information, which is hardly achieved by other methods. This shall be demonstrated by the nano-analysis of a 'spin-valve' layer sequence [81].

A soft magnetic $Ni_{81}Fe_{19}$ ('permalloy'), a paramagnetic Cu, and a hard-magnetic Co layer were deposited on tungsten substrate tips using preparation method (b) of fig. 21. Specimens are heat treated in a vacuum furnace at a pressure of 10^{-7} Pa. The atomprobe measurement is performed at a specimen temperature of 30 K with a puls frequency of 2 kHz, a pulse fraction of U_{pulse}/U_{dc} of 17% and a data rate of 0.015 atom/puls. Mass spectra obtained at the beginning of the measurement at the Co/Cu interface and later at the Cu/NiFe interface are shown in fig. 25. Although the metals are close neighbors in the periodic table, the mass resolution of the TAP is sufficient to distinguish them, apart from an overlap of Co with the minor ^{59}Ni isotope. In fig. 26, atomic reconstructions of the specimen in the as prepared stage (a,b) and after 30 min annealing at 350 °C (c,d) are presented. Since the detection probability of the detector systems is about 0.6, roughly the position of every other atom is represented by a colored dot inside the analysed volume. The tip radius is much larger than the measurement width. Hence, the prepared interfaces between Co and Cu (fig. 26a) and between Cu and permalloy (fig. 26b) appear to be flat. A chemical intermixing on a depth of 1.5 nm is determined at both interfaces. In the measurement after the heat treatment, a two-dimensional defect of decreased atomic density is noticed inside the Cu layer, which is identified as a grain boundary by
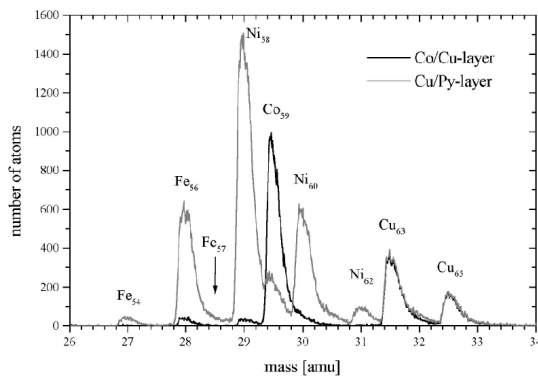

Figure 25: Mass spectra as obtained during the measurement of a Co/Cu/NiFe triple-layer.
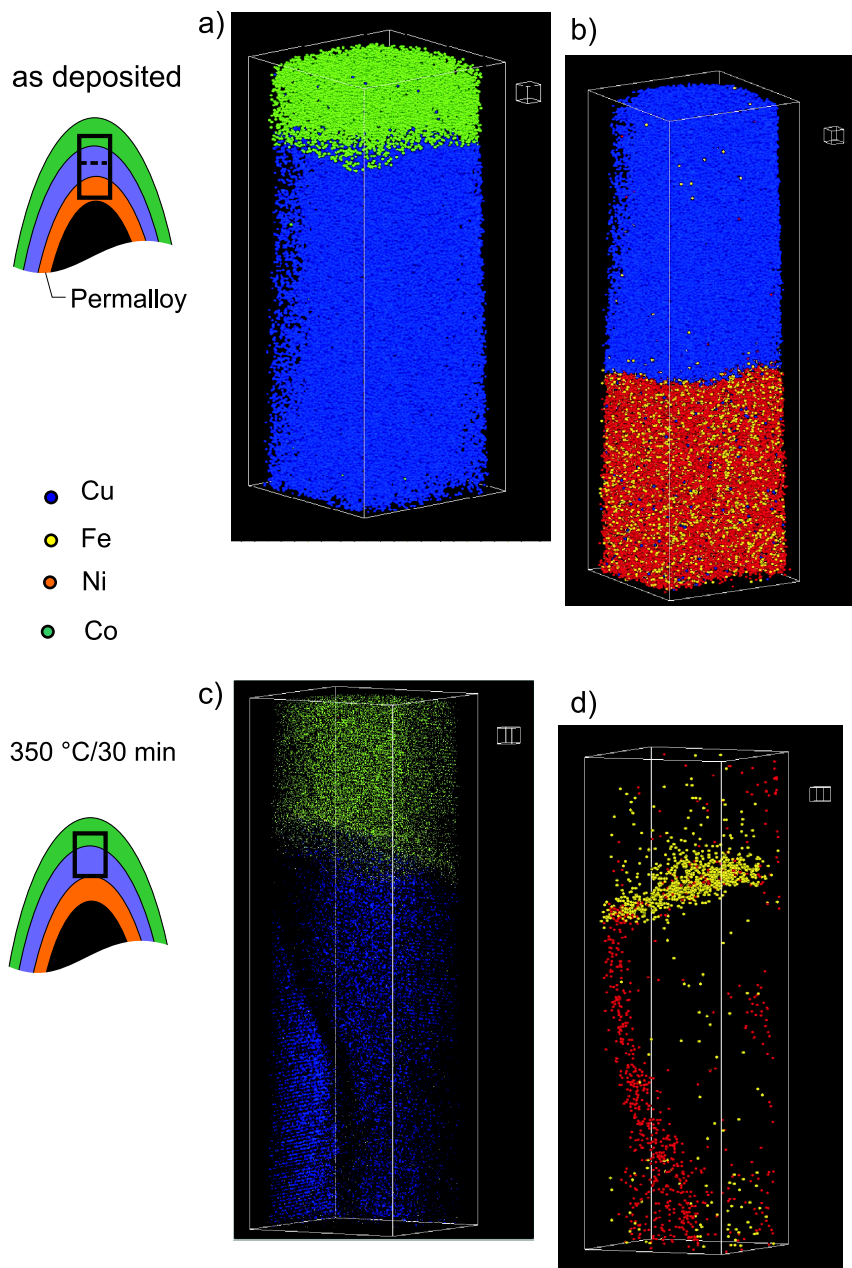
Figure 26: Analysis of a Co/Cu/NiFe triple layer. a,b) Reconstructions of the as-prepared state. The continuous measurement is split into two parts as indicated in the sketch at the left. c,d) Reconstruction of a specimen after 30 min annealing at 350 °C(c,d). Only the upper Co/Cu interface is shown. (d) shows the same measurement as in c) but only the positions of Ni and Fe are plotted. The scale of each reconstruction is indicated by the small cube with an edge length of 1 nm.

the different orientation of resolved lattice planes at both sides (fig. 26c). If only the Ni and Fe atoms are plotted (fig. 26d), the segregation of Ni at the grain boundaries of Cu and that of Fe at the interface to the Co layer is observed in as much clarity as can be desired.

The second example demonstrates the investigation of interfaces in planar systems prepared by lithography. A $(Cu_{10nm}/permalloy_{3.5nm}/Cu_{10nm}/Co_{10nm})_n$ multilayer was deposited on a planar glass substrate. Tips are prepared by electron beam lithography. In fig. 27 the reconstruction of a permalloy layer surrounded by Cu (a) and a composition profile determined normal to the interfaces (b) is shown. With increasing number of deposited layers, a considerable waviness of the interfaces develops, so that the interfaces are no longer planar. However, because of its local analysis, atomprobe tomography can distinguish between chemical mixing and surface roughness even on these small length scales.

Regarding the GMR effect, one might ask whether the observed Ni segregation at the Cu grain boundaries is a precursor to the formation of ferromagnetic bridges through the Cu layer. Or, does the interface dusting of the Co influence the magneto-resistivity? What about the influence of interface intermixing on the resistivity compared to that of interface roughness? Questions like this can be studied systematically only if the chemical evolution is determined in sufficient detail. Atomprobe tomography offers the possibility to do so.
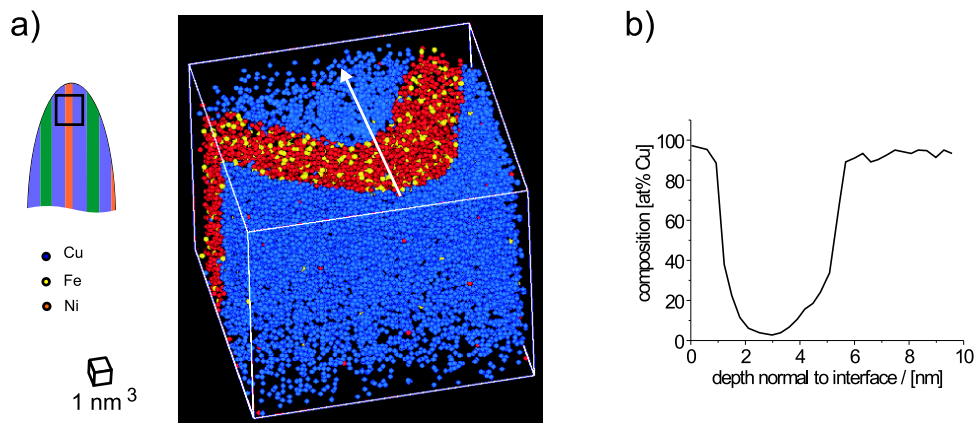

Figure 27: Analysis of a $(Cu/NiFe/Cu/Co)_n$ multilayer deposited onto a planar substrate. Specimen prepared by electron beam lithography. a) reconstructed atom distribution, b) local composition profile through the permalloy layer as indicated by the arrow in the reconstruction.

4 Microstructural effects on interdiffusion [63]

In 1958, Cahn and Hilliard extended the thermodynamics of homogeneous phases by a gradient energy term, in order to describe heterogeneous systems in a general field theory [82]. Although originally developed to explain spinodal decomposition, their theoretical work initiated numerous studies on interdiffusion, as the gradient energy should cause additional driving forces on diffusion lengths of a few nm [83, 84]. To measure mixing on such a small distance, usually X-ray diffraction is performed, a method based on early experiments of DuMond and Youtz [85]. Multilayers are prepared with an oscillation period of a few nm and the decay of the composition amplitude is determined by the intensity of satellite reflections. In a systematic study, Hilliard and coworkers could prove the importance of the gradient energy in the case of Cu/Pd [86] and Ag/Au [67]. The latter measurements have been confirmed recently[87]. Interdiffusion coefficients down to 10^{-24} cm^2/s are determined nowadays, so that the interdiffusion coefficient of Ag/Au is known over 15 orders of magnitude. The influence of the gradient energy becomes noticeable at multilayer periods below about 1 nm. In agreement to the attractive interaction of Ag and Au, the effective diffusivity is decreased at short wavelengths. Ag/Au turns out to be an ideal system to test this theory. Similar mobilities of both species and negligible lattice mismatch avoid additional complications caused by grain boundaries, non-equilibrium vacancies and elastic stress. In other cases, induced stress must be taken into account as reviewed by Larché and Cahn [88, 89]. More recently, Stephenson considered in addition plastic relaxation, described by a general viscosity of the material [90]. The model was successfully applied to explain interdiffusion measurements on amorphous Ni/Zr multilayers [91].

All the mentioned works take it for granted that a planar geometry is preserved during all interdiffusion stages, so that one-dimensional equations are sufficient to describe the reaction. Usually, vacancy equilibrium is tacitly assumed, which allows to define a unique interdiffusion coefficient, depending only on the local composition. According to the interest in microstructural aspects, we address the problem from a different point of view. We especially concentrate on the microstructural processes accompanying interdiffusion, which might have important consequences at very low temperatures [92] or in lattice-mismatched systems.

In the following study, the interdiffusion of two noble metals is considered. At first sight, this seems to be a very simple situation. Since atoms can exchange their position on a common fcc host lattice, a simple random walk might be expected. However the reaction turns out to be very fascinating, if the reacting metals are distinguished by a significant lattice mismatch. As the lateral dimensions of the layers are fixed by adhesion to the substrate, the interdiffusion is hindered by the different size of the intermixing atoms as sketched in fig. 28. How does nature achieve in this case a fast reaction to get rid of the considerable chemical energy
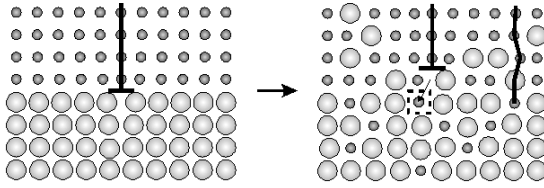
Figure 28: Interdiffusion of size mismatched materials. How does the induced stress influence composition profiles and overall kinetics? What are preferred mechanisms to relax misfit stress?

stored in the initial layers? What are preferred defects to relax the coherence stress and how are they formed?

To address these questions, the behaviour of Cu/Au is compared to that of the above mentioned reference system Ag/Au. With a lattice mismatch of about 12 %, Cu/Au represents an example of the situation in fig. 28. The importance of microstructural effects such as diffusion induced grain boundary migration (DIGM) was already indicated in early studies with less sensitive methods. The phase diagram of Cu-Au shows several ordered intermetallics at low temperatures. Thus, diffusion experiments are restricted to temperatures above 410 °C, to prevent the formation of any compound. Compared to the above mentioned effect of gradient energy, the studied microstructural phenomena develop on a coarser scale of several tens of nanometer. Therefore, cross section electron microscopy is very convenient, since different length scales are easily accessed. In order to determine the local mixing of the elements, Z-contrast microscopy by hollow cone illumination is used. Structural transformations are determined by high resolution microscopy.

In the following, at first macroscopic investigations by secondary neutral particle mass spectroscopy (SNMS) and XRD are discussed to demonstrate that the diffusion in both reaction pairs proceeds indeed very differently. Then the reaction of Cu/Au is analyzed microscopically. It will be shown that in epitaxial systems the most important influence of the coherency strain might not be a direct but an indirect one causing a deviation from vacancy equilibrium.

4.1 Macroscopic analysis of interdiffusion in Ag/Au and Cu/Au

To obtain an overview on the specimen behaviour and to define suitable temperatures, the interdiffusion of both reaction couples was investigated by depth profiling with secondary neutral particle spectrometry. Tri-layers of Au/Cu/Au and Au/Ag/Au were deposited on Cu and Ag single crystalline substrates by sputter deposition. Isothermal heat treatments were interrupted several times to perform an analysis. Further experimental details are found in [63, 65].

As an example, composition profiles are shown in fig. 29, which were obtained
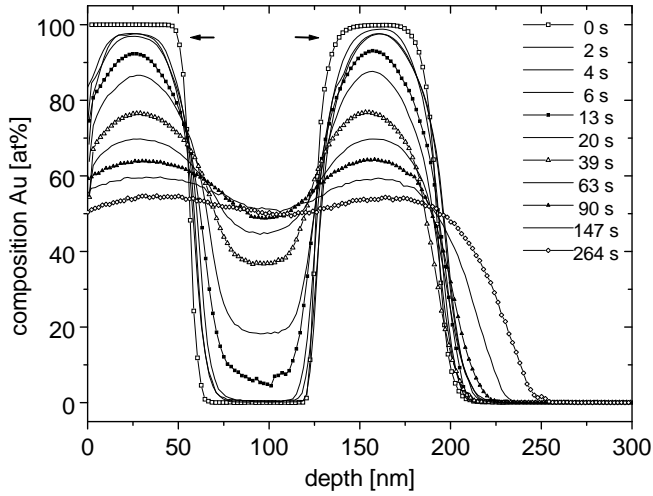
Figure 29: Compositional depth profiles of a Au/Cu/Au/Cu specimen obtained by SNMS during annealing at 430 °C.

during the annealing of a $Au_{60nm}/Cu_{60nm}/Au_{60nm}$ layer deposited on a Cu single crystal. Comparing the development of the composition profiles in Cu/Au and Ag/Au specimens a remarkable difference is seen. For that, the change of the peak compositions determined at the center of the various layers versus the annealing time is presented in fig. 30. Since it is probably influenced by the free surface, we disregard the final Au layer which covered the specimen surface. Dashed lines indicate the behaviour expected for volume diffusion according to Ficks' laws.

In the case of Ag/Au annealed at 350 °C (fig. 30a), the peak compositions change monotonously. At later stages, the kinetics is understood by ordinary volume diffusion. The very fast mixing in the early stages is explained by grain boundary diffusion, which is quantitatively discussed elsewhere [63]. However, the influence of the grain boundaries can be separated, if composition profiles are determined locally at positions far away from any grain boundary. Profiles of this kind have been determined by Z-contrast electron microscopy. Examples have already been presented in section 3.1.3, see figures. 17 and 19. Composition profiles in agreement with the thick film solution of Ficks' laws are obtained and the determined diffusion coefficient agrees with reported bulk values. With electron microscopy we do not observe any microstructural evolution. The grain and layer structure is preserved during all diffusion stages, which is not surprising because of the ideal atom matching, even though a different result was reported at very low temperatures [93].

The data of similar experiments with Cu/Au demonstrate a very different behaviour, see fig. 30b. Again a very fast interdiffusion (I) takes place at the beginning, which leads to the solution of two to three at%-Cu inside the Au layers. However, this first reaction stops already at 2 s annealing. A further development (II) is only noticed after a resting period of roughly 12 s. This way, the Cu/Au data point at a two-step reaction mechanism which is probably caused
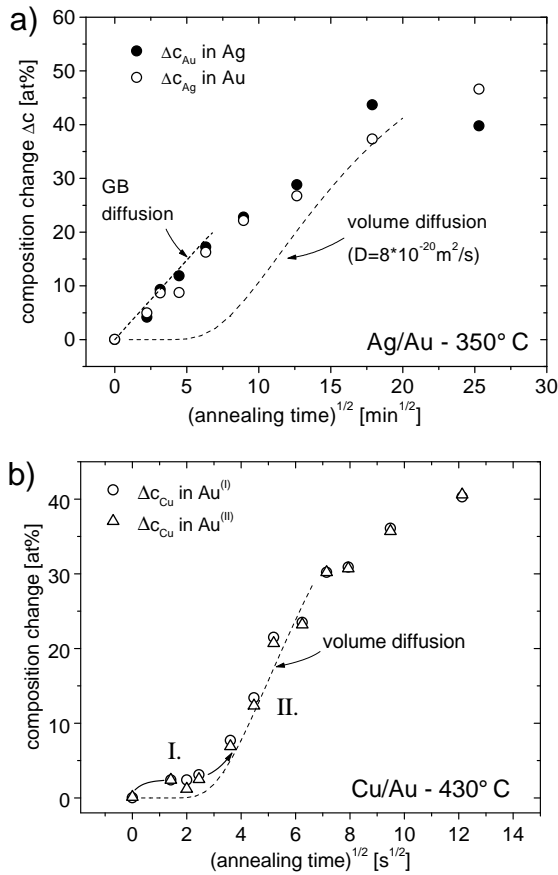
a)

composition change Δc [at%]

$\bullet$ Δc_{Au} in Ag
$\circ$ Δc_{Ag} in Au

GB diffusion

volume diffusion
($D=8*10^{-20} m^2/s$)

Ag/Au - 350° C

(annealing time)$^{1/2}$ [min$^{1/2}$]

b)

composition change [at%]

$\circ$ Δc_{Cu} in Au$^{(I)}$
$\triangle$ Δc_{Cu} in Au$^{(II)}$

volume diffusion

II.

I.

Cu/Au - 430° C

(annealing time)$^{1/2}$ [s$^{1/2}$]

Figure 30: Variation of peak compositions in the center of the layers. a) Ag/Au at 350 °C and b) Cu/Au at 430 °C.

by the large lattice mismatch, as this is the most prominent difference between both diffusion couples.

Another remarkable behaviour of the Cu/Au system is seen by X-ray diffractometry. As both components possess a very different lattice parameter, the composition of the binary alloy may be deduced from the diffraction angle of a given set of lattice planes. In fig. 31, X-ray spectra are shown as obtained during the annealing of a $(Au_{60nm}/Cu_{60nm})_n$ multilayer. Only the angle range containing the (111) peaks of Au and Cu is shown. As expected, the reflections of both pure components are found in the as-deposited state. We would expect these reflections to broaden because of the continuous composition profiles established by interdiffusion, and finally to meet into a central new reflection, corresponding to the completely intermixed alloy. By contrast, the experimental spectra develop several intermediate maxima, which point at the formation of regions inside the diffusion zone distinguished by different preferred compositions. This result is all the more striking as the diffusion temperature was chosen significantly above the highest order transition to prevent the formation of any ordered intermetallic phase, which is confirmed by the absence of superlattice reflections in the XRD spectra and electron diffraction patterns.
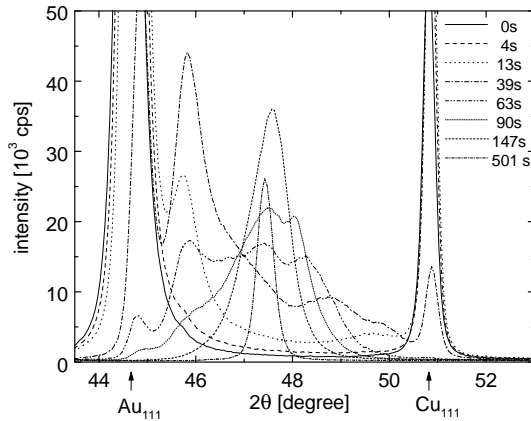
Figure 31: X-ray spectra of a Cu/Au multilayer obtained in $\theta - 2\theta$ geometry during annealing at 430 °C.(Co K_α radiation: $\lambda = 0.1790\,\text{nm}$)

4.2 Characterization of the initial interfaces

Very likely, the specific microstructure of the prepared specimens will influence the reaction mechanism and kinetics so that the initial state shall be characterized carefully. For TEM, layer structures were sputter deposited comprising 2 to 5 single layers, each 60 to 150 nm in thickness. To facilitate correct orienting of the specimens for HREM, single crystalline substrates were used. In addition, these substrates favor a very coarse grained microstructure of the metallic films.

With 12 % the lattice mismatch of Cu/Au is so pronounced that one is tempted to deny the possibility of epitaxial growth. Nevertheless, we do observe in the deposited layers a strong texture corresponding to the orientation of the Cu substrates. Epitaxial growth in this layer system was also reported previously [94]. By microscopy, a coarse grained microstructure with a lateral grain size exceeding 150 nm is determined. Using HREM, two dominating interface types are identified, the direct lattice transition between both fcc lattices (fig. 32a) and the twin relation (fig. 32b). As a consequence of the considerable lattice mismatch, misfit dislocations are introduced at the interfaces. However, their theoretical spacing amounts to only 2 nm, so that individual dislocation cores are hardly identified. For example, the Burgers' circuit sketched in micrograph (a) indicates already two additional {111} layers on the Cu side but the exact localization of the dislocations inside the circuit remains difficult. Beside these dislocations, we usually observe in the direct transition case a slight misorientation. Both lattices are twisted by 2 to 3° around a ⟨011⟩ axis, which probably allows a further relaxation of the mismatch strain.

In the twin case (b), the structural interface appears to be broadened to a thickness of 1 nm. Two layers of increased defect density, marked in fig. 32b by a pair of dashed lines, appear by a blurred fringe contrast. They are separated by a zone of more perfect lattice order. Although no individual dislocations can be localized in the micrograph, this observation allows the conclusion, that
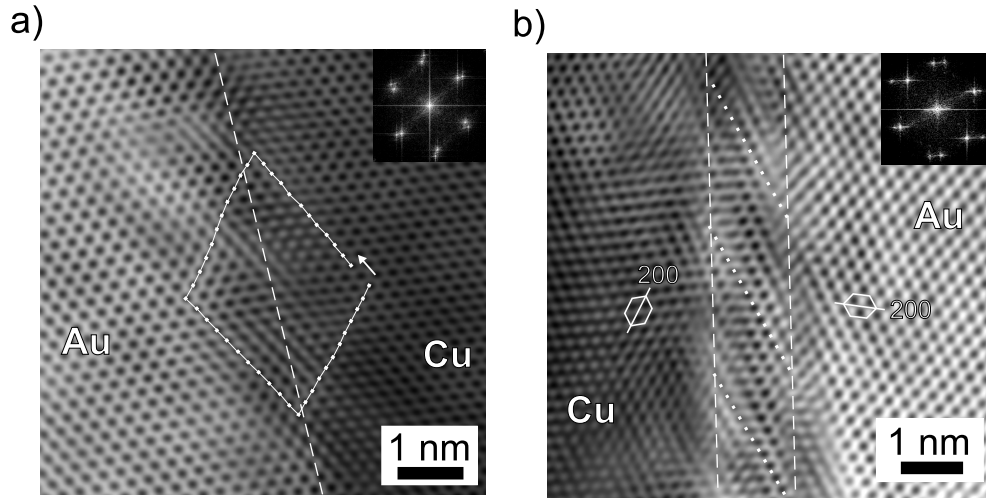
Figure 32: HREM of the interface between Cu and Au, a) direct lattice transition 'Σ1' with a Burgers' circuit, b) twin relation 'Σ3'

part of the misfit dislocations glide or climb out of the geometric interface plane. When an extended region of the interface is evaluated, a periodic variation of the fringe contrast along the interface becomes obvious which is indicated in the figure by dotted lines. The oscillation length amounts to 2 nm, in good agreement to the theoretical dislocation spacing. This periodicity suggests to consider the observed interphase boundaries similar to high angle grain boundaries in homogeneous materials, which consist usually of building units repeated periodically along the interface. Generalizing the coincidence site lattice (CSL) description to our hetero phase boundary let us define the observed interface types as 'Σ1' and 'Σ3'. The strong preference of these two relations is indeed understood by geometric matching of lattice sites [65]. This is proven using a generalized CSL approach proposed by Pirouz and coworkers [95], which considers the overlap of adjacent lattices in the reciprocal space.

Beside the structural characterization of the prepared interfaces, also their chemical properties are of interest. The spatially resolved analysis allows to characterize both interface types independently. Figure 33 shows composition profiles determined normal to the interfaces. The broader structural width of the twin boundary is reflected by a slightly increased intermixing. However, the difference is only minor. Roughly, for both interface types the depth of initial solution amounts to 2 nm, which is slightly larger than that measured in Cu/Au by Gladyszewski [96] or that typically found by atomprobe tomography in similar sputter-deposited specimens [42, 73, 97]. However, regarding the resolution limit of HCDF imaging of about 1 nm and potential misorientation or roughness of the interface, this discrepancy may not be significant. The initial microstructure of the Ag/Au specimen used for comparison is very similar regarding grain size
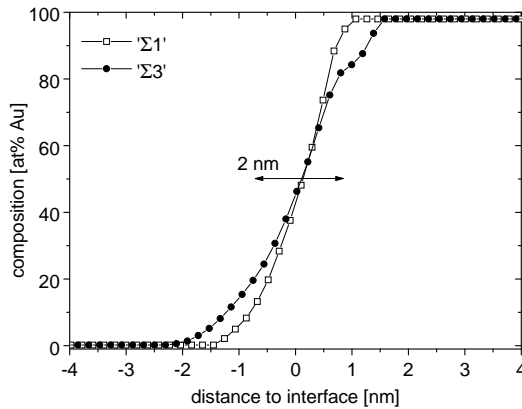
Figure 33: Composition profiles determined by HCDF imaging at as-prepared Cu/Au interfaces.

and orientation relation. Because of the low stacking fault energy of Ag and Au ($40\,\mathrm{mJ/m^2}$ and $20\,\mathrm{mJ/m^2}$, respectively), lattice twins are formed in high density as is seen in fig. 17. By the parallel alignment of the coherent twin boundaries, the epitaxial relation between different layers becomes obvious.

Summarizing one has to state that the overwhelming fraction of the interphase boundary consists of only two interface types. In both, the adjacent lattices have at least one set of densely packed {111} planes in common. In the case of Cu/Au, about every eighth of these planes is bounded by a dislocation close to the interface to accommodate the difference in the lattice parameters.

4.3 Microscopic analysis of the interdiffusion of Cu/Au

The aforementioned depth profiling indicates, that the interdiffusion of Cu/Au may proceed by two subsequent reaction steps. However, only microscopic investigations are able to prove this hypothesis and to detect the mechanism on the atomic scale.

4.3.1 Mechanism of first reaction stage

In fig. 34, a Cu/Au reaction couple deposited onto a Cu substrate is shown after 5 s annealing at 430 °C. This aging condition falls well into the regime of the proposed first reaction stage. If the annealed specimen is compared to an as-deposited one (BF and HCDF images of the initial stage have been published in [98]), plate-like defects, appearing as needles in the 2D projection, have developed at the interface. This becomes particularly clear at the twin type boundary where the defects are oriented parallel to the common {111} plane set. See interface at (a) in fig. 34. The image at the right shows a part of such a defect zone in increased magnification. The defects are found inside a band along the original interface with a homogeneous thickness of 17 nm.
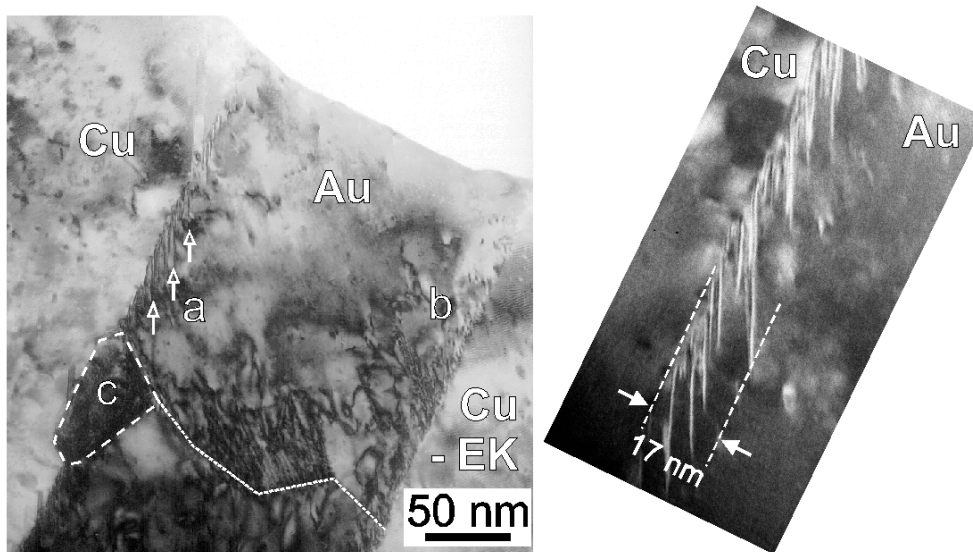
Figure 34: BF cross sections images of a Cu/Au/Cu(s.c.) specimen after 5 s annealing at 430 °C. Interface types at mark (a) 'Σ3', at (b) 'Σ1'. A nucleus of a new grain formed already at (c). The dotted line emphasizes a small angle grain boundary across the Au layer. Imaging was performed under two beam condition to optimize the contrast of structural defects. The detail at the right side shows part of the interface (a) in higher magnification.

By compositional analysis based on HCDF images, it is demonstrated that the formation of the observed defects is indeed related to an intermixing of both components. Data of the analysis are shown in fig. 35. The points represent measurements at different lateral positions along the interface. However, a well defined continuous profile across the defect band is obtained on the average. The position of the structural defects relative to the diffusion profile is indicated by dashed lines. Obviously, they are introduced when the intermixing exceeds about 10 at% at the Au and the Cu side as well.

The atomic nature of the observed defects is elucidated by high resolution microscopy. In fig. 36a, a phase contrast image of a twin type interface is shown after 5 s heat treatment at 430 °C. The adjacent lattices are mirrored at the common $(11\bar{1})$ plane, so that both are distinguished easily, as shown by the white line. The needle like defects noticed in the conventional bright field images correspond to spikes of Cu lattice orientation growing into the Au crystal. This way, the original planar interface becomes extremely rough.

How is this lattice transformation achieved? To answer this question the fringe contrast was analyzed in detail by comparison to electron optical simulations performed with established simulation software [99]. Technical details of this procedure are described elsewhere [63]. The essential results explaining the reaction mechanism are illustrated by three enlarged details shown in the lower
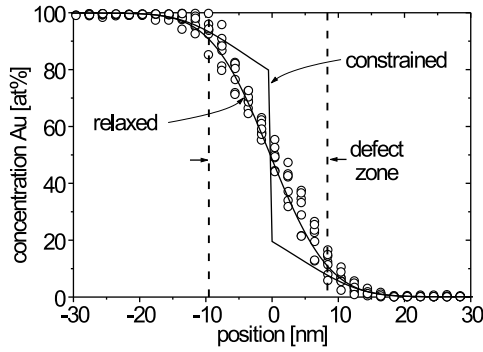
Figure 35: Composition profile at a Cu/Au interface after annealing 430 °C/5 s determined by HCDF imaging. Solid lines are calculated by Eq. 28 (relaxed) and Eq. 38 (constrained). Dashed lines indicate the extension of structural defects.

part of fig. 36.

At the needle's tip, a densely packed plane is inserted ending in a Frank type prismatic dislocation, $b = [11\bar{1}]a/3$, as is demonstrated in fig. 36b. Because of the additional lattice plane, the stacking sequence is locally transformed into that of the related twin, which is shown in fig. 36c. By comparison with different simulated structures it is proven that the additional plane is bounded by a prismatic dislocation; no further relaxation by another Shockley partial, transforming the sessile prismatic dislocation into a glideble one, is found. In the figure, part of a simulated image showing the best matching to the experimental one is inserted.

Towards the Cu side, the needles grow in thickness, which means on the atomic scale that further lattice planes are 'switched' into the stacking sequence of the Cu crystal, as shown in the figure 36d. This is achieved by conservative motion of Shockley partials with Burgers vectors $b_1 = [112]a/6$ or $b_2 = [2\bar{1}1]a/6$ which are able to glide on the common $(11\bar{1})$ plane. In addition, further lattice planes are inserted by the described climbing mechanism to accommodate the difference of the lattice constants.

In the case of a '$\Sigma 1$' boundary, the introduction of additional lattice planes is observed in the same manner. Their habit plane is chosen randomly out of the existing four possibilities. However, as in this case no rotation of the lattice is required, the defects show much weaker contrast, see fig. 34, interface at (b). Beside partials, which are needed to restore the previous stacking sequence at the inserted planes, now complete lattice dislocations contribute also to the relaxation of the misfit stress.

4.3.2 Mechanism of the second reaction stage

Surprisingly, the described semi-coherent reaction shows no development with further annealing. The defect band as well as the diffusion profiles are observed between 2 s, the shortest time which could be realized in the experiment, and
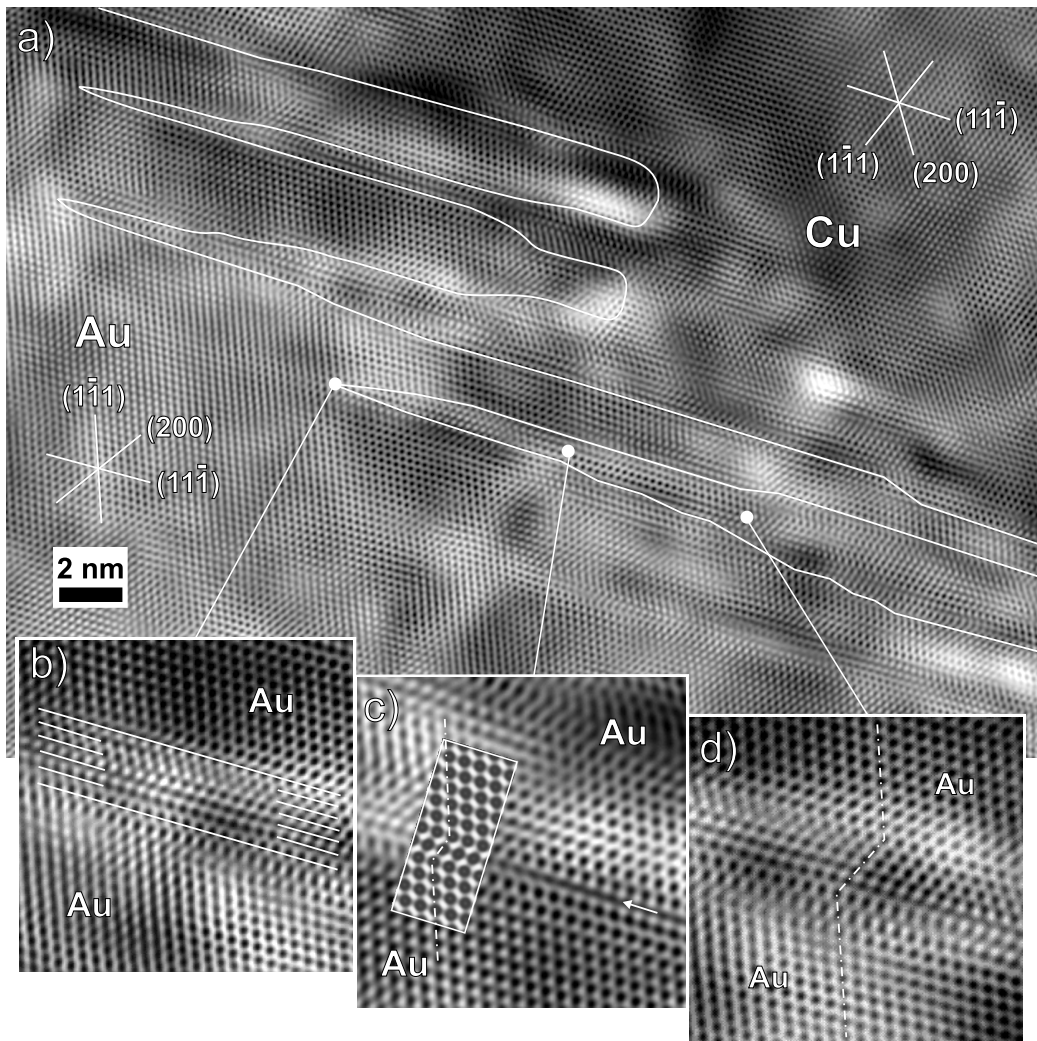
Figure 36: a) Phase contrast image of the structural defects formed at a Cu/Au interface by 5 s annealing at 430 °C. The adjacent lattices are oriented in twin relation. Both lattices are imaged in (011) zone axis orientation, defocus chosen close to Scherzer focus. b) to d) several details observed along one needle-like structure. Locations as indicated in a). A noise filter was applied to improve the reproduction.

15 s with a comparable width, which leads to the conclusion that this first reaction step proceeds very fast initially, but ceases when a depth of 15 to 20 nm is reached. Instead a second process comes into play which dominates the interdiffusion process after about 15 s annealing. It is seen to be initialized already after 5 s annealing in the micrograph of fig. 34. At the position marked with (c), a grain of only 30 to 50 nm size is observed, which extends somewhat into the Cu lattice and has not developed the needle-like defect structure at its boundary. As grains of this size are not observed in the as-deposited stage, obviously, a new grain has nucleated at a triple point, where a small angle grain boundary previously met

the interface.

Further stages of this process are shown in fig. 37 where BF images (a,c) are compared to the corresponding HCDF images (b,d). Again, by means of HCDF images the chemical transport related to the structural transformation is detected. In fig. 37 a and b, a new grain nucleated at the interface. Without doubt, the formation of the new grain is related to a transport of Au into the Cu lattice.

A specimen after 10 s annealing is shown in fig. 37 c and d. At this intermediate reaction stage, the newly formed grains are organized in clusters, heterogeneously distributed along the interface as seen at the right and left side of the figures. Large angle grain boundaries are found in high density inside the clusters. Outside, the planar interface still exists, revealing defect bands formed by the first, semi-coherent reaction mechanism. Overviews representing larger interface regions after different annealing times are reproduced in fig. 38. The early interdiffusion stages of Cu/Au are by no means understood as a planar layer reaction. This becomes particular clear by the extremely rough interfaces and surfaces induced by heterogeneous nucleation and transport during 20 s annealing.

Two important aspects of this recrystallization mechanism must be empha-
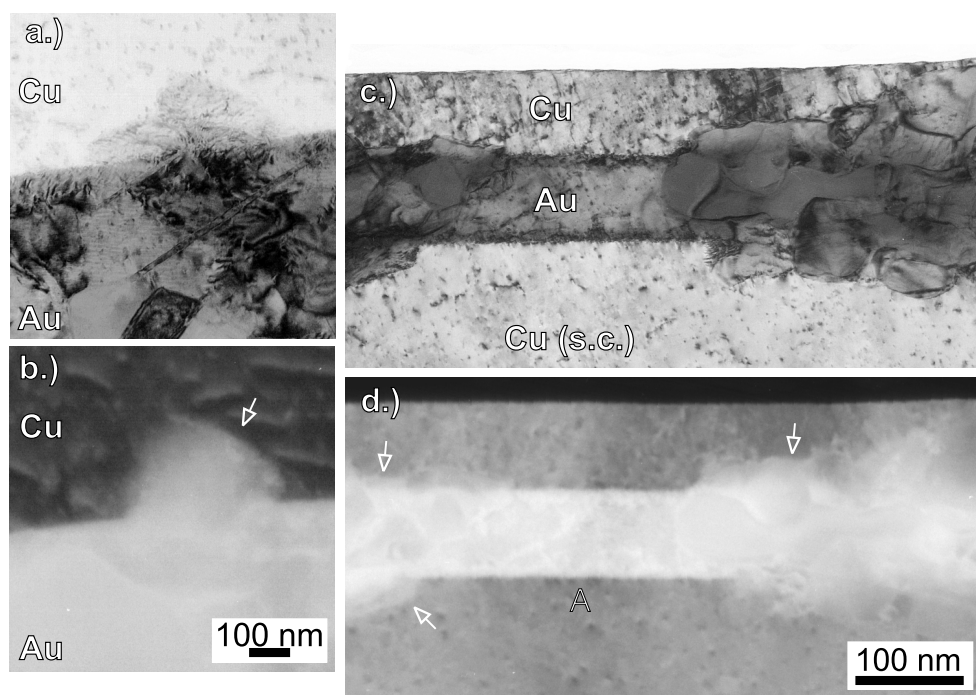

Figure 37: BF (a,c) and HCDF (b,d) images of a Cu/Au reaction couple after annealing at 430 °C for 5 s (a,b) and 10 s (c,d).
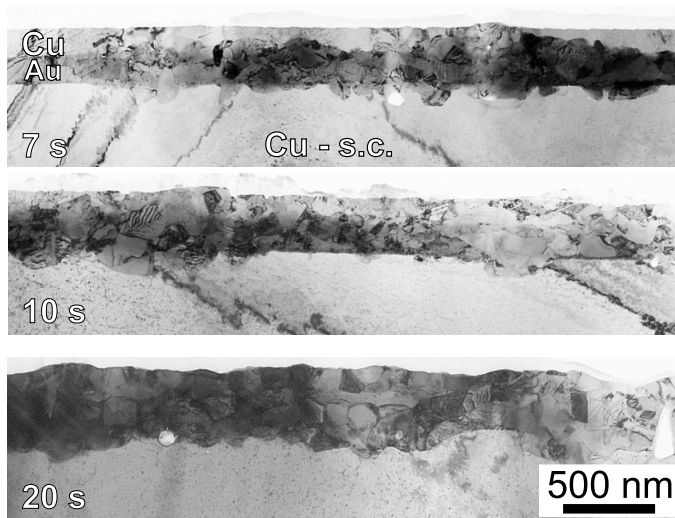
Figure 38: Cross section images of a Cu/Au/Cu(s.c.) specimen after annealing at 430 °C for several times as indicated.

sized. i) In HCDF images such as fig. 37, discontinuous composition profiles are noticed across the grain boundaries. This becomes particular clear at the positions marked by arrows. Probably, most of the other boundaries are not aligned parallel to the optical axis, so that apparently continuous profiles result as an artefact of image projection. Therefore, we conclude that discontinuous composition steps are likely to represent the general rather than the exceptional case at the boundaries.

ii) The observed second reaction step is not sufficiently described as diffusion induced grain boundary migration (DIGM). Instead new grain orientations are nucleated which is particularly obvious inside the Cu substrates, where the single crystal is broken into many grains of different orientation. Thus, we are faced to a recrystallization which is, compared to conventional metallurgy, driven in the inverse direction; an initially single crystalline or very coarse grained microstructure is transformed into a nanocrystalline one.

4.4   Discussion

The presented experimental study yields clear evidence that the early interdiffusion of the size-mismatched metals Cu and Au proceeds by two subsequent reaction stages as sketched in fig. 39. In the first semi-coherent step (a), the epitaxial lattice relation is preserved. Relaxation of diffusion induced strain and, in the case of the twin type boundary, the required rotation of the lattice is achieved by climbing and gliding of dislocations. The second incoherent reaction step (b) is characterized by nucleation of new grains and migration of high angle grain boundaries.
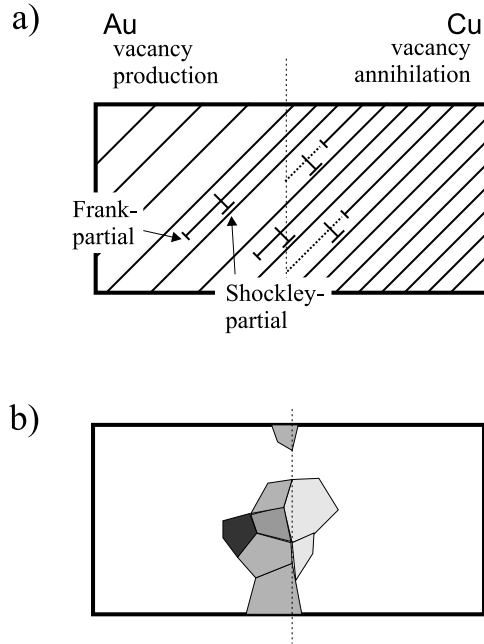
Figure 39: The two stages of interdiffusion in Cu/Au: a) semicoherent reaction by volume diffusion, b) discontinuous reaction by recrystallization and grain boundary migration.

4.4.1 Semi-coherent reaction stage

Several features of the planar diffusion zone established during the first reaction stage are quite remarkable. The measured composition profiles develop symmetrically between Cu and Au and no Kirkendall voids are observed, although bulk diffusion data [100] predict a higher diffusion rate inside the Au layer with Cu being the more mobile element. This may indicate, that the vacancy density is far from equilibrium in this very early reaction stage, which is characterized by very high composition gradients and diffusion lengths much smaller than the typical distance between efficient vacancy sinks.

Furthermore, the profiles vary continuously across the composition range, which is only understood if most of the diffusion induced stress relaxes by the observed structural defects. This is clarified by the following quantitative consideration: Let us assume for the moment a Au layer which is perfectly fixed to the Cu substrate, so that no relaxation occurs along the lateral directions (x and y axis). In consequence, the chemically induced variation of the lattice parameter is counteracted by a dilatational stress (see [101])

$$\sigma_{xx} = \sigma_{yy} = \frac{E}{1 - \nu} \eta \, c_{\text{Cu}} \,, \tag{35}$$

which adds the elastic contribution

$$e = \frac{E}{1 - \nu} \Omega \, \eta^2 c_{\text{Cu}}^2 \tag{36}$$

to the system's free energy. In these equations, E, ν, η, and Ω have their usual meaning Youngs modul, Poisson's ratio, misfit parameter $\eta = (a_{\text{Cu}} - a_{\text{Au}})/a_{\text{Au}}$

and atomic volume of Au, respectively. Thus, the interdiffusion potential $\partial f/\partial c$ must be modified by an elastic correction, which leads to the transport equation

$$j_z = -\frac{Dc_{Cu}(1-c_{Cu})}{kT}\left(\frac{\partial^2 f}{\partial c_{Cu}^2}+\frac{2\Omega\eta^2 E}{1-\nu}\right)\frac{\partial c_{Cu}}{\partial z} \tag{37}$$

$$= -D\left(1+\frac{c_{Cu}(1-c_{Cu})}{kT}\cdot\frac{2\Omega\eta^2 E}{1-\nu}\right)\frac{\partial c_{Cu}}{\partial z}, \tag{38}$$

where the second term inside the brackets at the right hand side accounts for the stress effect. The case of a Cu layer is formulated analogously; only the sign of the stress must be inverted and the material parameters adapted. Integrating Eq. 38 with appropriate elastic constants $E_{Au} = 0.70 \cdot 10^{11}\,\text{N/m}^2$, $\nu_{Au} = 0.428$, $E_{Cu} = 1.1 \cdot 10^{11}\,\text{N/m}^2$, and $\nu_{Cu} = 0.356$ [102], composition profiles are calculated as that shown by the solid line (constrained) in fig 35. Because of the very pronounced lattice mismatch, an elastically stabilized miscibility gap is predicted, ranging from about 20 to 80 at% Cu. Similar discontinuities in the composition profile are also predicted in the more sophisticated analysis by Stephenson. See for example simulated profiles in recent work on interdiffusion of amorphous Ni/Zr [91].

By contrast, in none of our experimental data we do observe any indication of such a compositional gap. Instead, the nanoanalysis always yields profiles in agreement to the conventional thick film solution of Ficks' laws as indicated by the solid line (relaxed) in the fig. 35. Obviously, before reaching the elastic solubility limit of 20 at% at either side of the profile, misfit dislocations move out of the interface, thereby reducing the stress efficiently. Based on the nanoanalytical data the critical composition for structural relaxation is determined to about 10 at% (see the boundaries of the defect band in fig. 35). For this composition, a stress of 1.5 GPa is calculated by Eq. 35. This value exceeds the typical shear stress $\sigma_c = 10^{-4}$ to $10^{-5}E$ of single crystalline metals [103] already by two orders of magnitude, which indicates that stress levels required to induce the predicted miscibility gap are hardly achieved.

Most surprisingly, after a few seconds of annealing, the semi-coherent reaction retards in a way that cannot be explained by ordinary parabolic growth. Either diffusion induced stress or a non-equilibrium density of vacancies may be made responsible for this behaviour. But, according to the presented estimates, the stress is probably not sufficient to explain such a drastic change of diffusion behaviour like a complete stop of the reaction. Furthermore, neglecting relaxation, which would only decrease the elastic back stress, the expense of elastic energy scales proportional to the diffusion width as does the gain of chemical energy, so that the existence of a limiting thickness cannot be understood by elastic effects.

Therefore, the observed retardation is very likely caused by a decrease of the vacancy density within the first few seconds of annealing. Further evidence for

the important role of vacancies is seen in the different diffusion widths observed at the interface between the single crystalline substrate and a deposited layer and that between two deposited layers, as presented in a previous publication [104]. Although not directly influenced by grain boundary diffusion, the latter diffusion zone is observed twice as thick as the former one, which is presumably due to an initial supersaturation of vacancies or their faster equilibration inside the deposited, poly-crystalline layers.

To explain such a vacancy depletion one might consider the annealing of non-equilibrium vacancies introduced during film deposition. However, it is doubtful whether the initial supersaturation could be sufficient to yield an apparent reaction stop. Therefore, it is suggested that in addition the semi-coherent diffusion mechanism itself provides an effective sink, which annihilates vacancies inside the diffusion zone. This is justified by the following model calculation.

As revealed by HREM, climbing of prismatic dislocations provides the dominant plastic relaxation mechanism. Dislocations which climb towards the Au side generate vacancies, those climbing towards the Cu side annihilate them. If these two processes are not balanced, a total loss of vacancies may appear. For the sake of simplicity, we assume a simple cubic lattice with a microstructure similar to that sketched in fig. 39a, but the set of common lattice planes aligned normal to the interface. Let us consider the limiting case of complete relaxation where the lattice mismatch along the x-axis is immediately accommodated by climb of dislocations. Thus, we expect for the number M of planes stacked along the x-axis over a distance of L

$$M\left(c_{\mathrm{Cu}}\right) = \frac{L}{a_{\mathrm{Au}}\left(1 - \eta c_{\mathrm{Cu}}\right)}\,,\qquad(39)$$

if the lattice parameter of the alloy follows Vegard's law, a reasonable approximation to the behaviour of disordered CuAu alloys [105].

Remarkably, this relation is by no means linear with respect to the composition, which has an important consequence to the vacancy balance. Regarding the variation with local composition

$$\frac{\partial M}{\partial c_{\mathrm{Cu}}} = \frac{L\eta}{a_{\mathrm{Au}}(1 - \eta c_{\mathrm{Cu}})^2}\,,\qquad(40)$$

it is quite obvious, that the insertion and removal of lattice planes proceeds asymmetrically at the Au and Cu side, respectively. A variation of M within a slab of thickness $\triangle z$ changes the number of vacancies by

$$\mathrm{d}N_{\mathrm{Vac}} = \frac{L\,\triangle z}{a_{\mathrm{Au}}^2(1 - \eta c_{\mathrm{Cu}})^2}\cdot\frac{\partial M}{\partial c_{\mathrm{Cu}}}\,\mathrm{d}c_{\mathrm{Cu}}\qquad(41)$$

causing a change of the local vacancy fraction

$$\mathrm{d}c_{\mathrm{Vac}} = dN_{\mathrm{Vac}}\frac{a_{\mathrm{Au}}^3(1 - \eta c_{\mathrm{Cu}})^3}{L^2\,\triangle z}\qquad(42)$$

$$= \frac{a_{\mathrm{Au}}(1 - \eta c_{\mathrm{Cu}})}{L} \cdot \frac{\partial M}{\partial c_{\mathrm{Cu}}}\, dc_{\mathrm{Cu}} \tag{43}$$

$$= \frac{\eta}{1 - \eta c_{\mathrm{Cu}}}\, dc_{\mathrm{Cu}} . \tag{44}$$

If the composition profile develops symmetrically in the sense that $dc/dt|_c = -dc/dt|_{1-c}$, obviously more vacancies are annihilated at the Cu side than produced at the Au side. To determine the behaviour also in the case of asymmetric atomic mobilities, we have to solve the diffusion problem inside a bi-layer specimen. The outer boundaries are assumed to be impermeable, which corresponds to a multilayer, where the flux of all species vanish in the middle of the layers, as required by the specimen's symmetry. Independent site exchanges of Cu-Vac and Au-Vac pairs are considered, which results in the following ansatz for the particle flux

$$\begin{pmatrix} j_{\mathrm{Cu}} \\ j_{\mathrm{Vac}} \\ j_{\mathrm{Au}} \end{pmatrix} = \begin{pmatrix} -D'_{\mathrm{Cu}}c_{\mathrm{Vac}} & D'_{\mathrm{Cu}}\,c_{\mathrm{Cu}} & 0 \\ D'_{\mathrm{Cu}}c_{\mathrm{Vac}} & -D'_{\mathrm{Cu}}\,c_{\mathrm{Cu}} - D'_{\mathrm{Au}}\,c_{\mathrm{Au}} & D'_{\mathrm{Au}}c_{\mathrm{Vac}} \\ 0 & D'_{\mathrm{Au}}\,c_{\mathrm{Au}} & -D'_{\mathrm{Au}}c_{\mathrm{Vac}} \end{pmatrix} \frac{\partial}{\partial z} \begin{pmatrix} C_{\mathrm{Cu}} \\ C_{\mathrm{Vac}} \\ C_{\mathrm{Au}} \end{pmatrix} \tag{45}$$

and the evolution of the atomic densities

$$\frac{dC_{\mathrm{Cu}}}{dt} = -\frac{\partial}{\partial z} j_{\mathrm{Cu}} \tag{46}$$

$$\frac{dC_{\mathrm{Au}}}{dt} = -\frac{\partial}{\partial z} j_{\mathrm{Au}} \tag{47}$$

$$\frac{dC_{\mathrm{Vac}}}{dt} = -\frac{\partial}{\partial z} j_{\mathrm{Vac}} + \frac{\eta}{1 - \eta\, c_{\mathrm{Cu}}} \left(c_{\mathrm{Cu}} \frac{\partial}{\partial z} j_{\mathrm{Au}} - c_{\mathrm{Au}} \frac{\partial}{\partial z} j_{\mathrm{Cu}} \right) . \tag{48}$$

In these equations, capital letters C_i denote concentrations per volume, whereas small letters c_i denote atomic fractions. The second term on the right hand side of Eq. 48, accounting for vacancy production and annihilation, was derived from Eq. 44 obeying $c_{\mathrm{Cu}} \approx C_{\mathrm{Cu}}/(C_{\mathrm{Cu}} + C_{\mathrm{Au}})$. The diffusivities $D'_{\mathrm{Cu}} = D_{\mathrm{Cu}}/c_{\mathrm{Vac}}^{(eq)}$ and $D'_{\mathrm{Au}} = D_{\mathrm{Au}}/c_{\mathrm{Vac}}^{(eq)}$ may vary with composition, depending on the metallic system under consideration. In order to limit the computing time, the equilibrium vacancy fraction is chosen to 10^{-5}, which is artificially high compared to the experimental value.

In fig. 40, two examples of model calculations are presented. For the example (a), $D_{\mathrm{Cu}} = D_{\mathrm{Au}} = D = const$ is assumed. At the very beginning of the reaction (atomic diffusion length $10^{-4}w$, with w thickness of the sample), still a vacancy supersaturation at the Au side evolves, but soon the annihilation of vacancies at the Cu side dominates the reaction and an overall vacancy depletion results. In calculation (b), $D_{\mathrm{Cu}} = D(1 + 100c_{\mathrm{Au}})$ and $D_{\mathrm{Au}} = D(1 + 10c_{\mathrm{Au}})$ is assumed, which resembles the behaviour of AuCu expected from bulk diffusion data; compared to pure Cu, the bulk diffusion in pure Au is much faster and furthermore Cu atoms are more mobile than Au atoms [100]. In this case, at first a vacancy
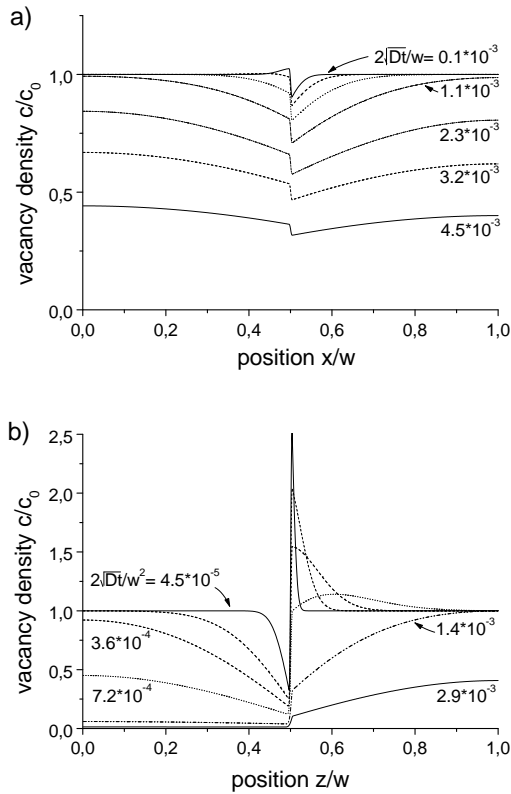
Figure 40: Model calculation of vacancy density during the semi-coherent reaction stage. The reaction time is characterized by the diffusion length of the atomic transport. w denotes the thickness of the sample, the interface is located at $z = w/2$. The initial vacancy fraction c_0 was chosen to 10^{-5}. a) equal mobility of the species in both phases, b) faster diffusion inside the Au layer, with Cu being the more mobile element.

supersaturation develops at the Cu side because of the difference in the atomic mobilities. But similar to the former example, the reaction zone is depleted of vacancies in later stages. Similar calculations were performed for several other choices of the relative diffusivities. In all cases the vacancy density is finally controlled by the predominant annihilation at the Cu side.

Certainly, the real situation is more complex than assumed in our simplified model. Vacancy densities deviating from equilibrium will produce itself an osmotic climbing force to dislocations [106] which counteract the elastic climbing force. Eventually, the prismatic dislocations follow the interdiffusion with a certain delay, so that our assumption of instantaneous and complete stress relaxation is only a crude first approximation. In addition, other neutral vacancy sinks or sources, like glideble edge dislocations or grain boundaries are neglected and the initial vacancy density is overestimated. But despite these limitations, at least the existence of a significant driving force to vacancy annihilation induced by the coherency constraint can be inferred. This way, the presented calculations support the hypothesis that the reaction stop is caused by vacancy depletion. In consequence, the reaction is not as much effected directly by coherency stress as indirectly by a stress-induced non equilibrium of point defects.

4.4.2 Incoherent reaction stage

As the coherent reaction slows down after very short annealing, an effective re-
duction of the system's free energy is only possible by the onset of a second
mechanism. Grains are nucleated at the interface introducing high angle grain
boundaries, which allow to restore the vacancy equilibrium and to relax induced
stress. As concluded from HCDF images, the previously continuous diffusion
zone splits into homogeneous regions of different composition. This interpreta-
tion is further supported by the X-ray diffractograms presented in fig. 31. Using
Vegard's law to interpret the position of the intensity maxima, the preferred com-
positions of newly formed grains are inferred as shown in fig. 41. At about 10 s
annealing, a first generation of grains nucleates at both sides of the interface
having a composition difference of about 20 at% to the surrounding pure Cu and
Au. After further annealing for 30 s, a second generation of grains forms, show-
ing roughly the same composition difference to their surroundings comprised of
grains of the first generation. Later, the grains of first generation disappear while
those of second generation continuously equalize their composition to merge fi-
nally at the average composition of the specimen. It should be pointed out that
the number and the absolute values of the observed compositions 20, 43, 69, and
82 at%-Au are incompatible with the ordered compounds known in the system at
lower temperatures. This makes particularly clear that the described behaviour
is controlled by kinetic rather than thermodynamic factors.

Regarding the considerable chemical driving force provided by the chemically
abrupt interface, a nucleation process with a clear incubation period and het-
erogeneous nucleation sites is surprising. By calorimetry, the mixing enthalpy of
equal amounts of Cu and Au is determined to 5.3 kJ/mol. Hence, assuming a
regular solution, the chemical driving force to form the observed grains with a
composition of 20 at% is estimated to $f_v = 7.4 \cdot 10^{-5}$ kJ/m^3. If a specific inter-
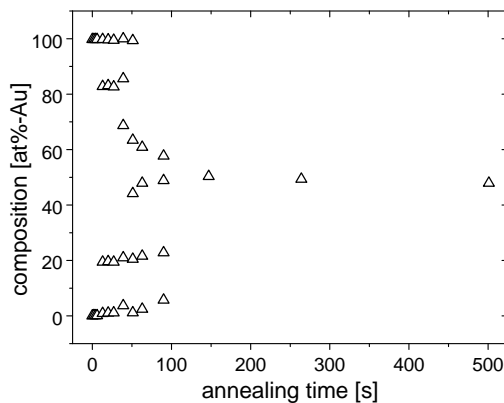face energy of $\gamma = 600$ mJ/m^2 is assumed, a typical value of large angle grain

Figure 41: Dominant compositions
inside the reaction zone as derived
from the peak intensities of the X-
ray spectra in fig. 31.

boundaries in Cu, the diameter of a nucleus is predicted to

$$d = \frac{4\sigma}{f_v} = 3\,\mathrm{nm}\,. \tag{49}$$

This value is indeed too small to explain the observed heterogeneous nucleation and the average grain size of the observed grains in the recrystallized regions. However, by analogy to DIGM, where the question of the appropriate driving force was already addressed by careful experiments [107], it is suggested that not the total gain of chemical energy, but only the contribution of the strain field and structural defects may be considered to drive the microstructural transformation.

In this case, the size of a nucleus may be estimated by comparing i) a stressed rectangular volume $d \times d \times 2d$ containing a continuous composition variation of diffusion length $2d$ with ii) two relaxed grains at both sides of the interface with a different but homogeneous composition, see the schematic composition profile in fig. 42a. To avoid complex geometric factors, we assume a linear composition profile and cubic grains of edge size d. The elastic energy in case i) is determined by

$$
\begin{aligned}
E_{\mathrm{elast}} &= 2d^2 \frac{E}{1-\nu} \eta^2 \int_0^d \triangle c(z)^2 \mathrm{d}z \tag{50} \\
&= 2d^2 \frac{E}{1-\nu} \eta^2 \int_0^d \frac{1}{4} \left(1 - \frac{z}{d}\right)^2 \mathrm{d}z \tag{51} \\
&= \frac{d^3}{6} \frac{E}{1-\nu} \eta^2\,, \tag{52}
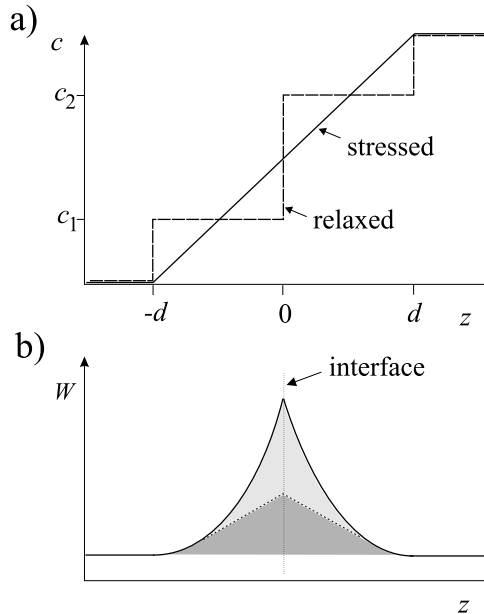\end{aligned}
$$

Figure 42: Schematic composition profile through the diffusion zone (a) and stored energy of the stressed case (b).

where we made use of Eq. 36. This has to be compared to the expense for the grain boundaries in case ii)

$$E_{\mathrm{GB}} = 12d^2\gamma\,, \tag{53}$$

so that the nucleus size is determined by

$$\frac{\partial}{\partial d}\left(12d^2\gamma - \frac{1}{6}\frac{E}{1-\nu}\eta^2 d^3\right) = 0\,, \tag{54}$$

which yields

$$d = 48\frac{\gamma(1-\nu)}{E\eta^2}\,. \tag{55}$$

Inserting average material constants, $\gamma = 0.6\,\mathrm{J/m^2}$, $E = 0.9 \cdot 10^{11}\,\mathrm{N/m^2}$, $\nu = 0.39$, the size of a critical grain is predicted to $\approx 15\,\mathrm{nm}$. In this calculation still plastic relaxation has been neglected. Relaxation would reduce the quadradic composition dependence of the stored energy to a linear one, as soon as $\triangle c$ exceeds the observed elastic limit of about $10\,\mathrm{at\%}$, see the pointed line in fig. 42b. Thus, as indicated by the area below the energy curve in the figure, the total driving force might be further decreased to one half. In consequence, a nucleus size of a few tens of nm is quite realistic and in agreement to the early grains observed in the micrographs (see e.g. fig. 34). Furthermore, it makes clear, that the onset of the second reaction step is only possible after an incubation period of $10\,\mathrm{s}$ during which the necessary driving force is build up by interdiffusion on a depth of 15 to $20\,\mathrm{nm}$.

By nucleation of grains, mobile high angle grain boundaries are introduced into the former epitaxial microstructure. This is reflected by very fast reaction rates and low activation energies seen by calorimetry. A value of $E_{\mathrm{act}} = 1.18\,\mathrm{eV}$ is found [63], which is significantly smaller than the $\approx 2\,\mathrm{eV}$ determined for volume diffusion in massive Cu or Au [108, 109], but more close to the 0.87 and $1.09\,\mathrm{eV}$ measured for grain boundary diffusion in both metals [110, 111]. Obviously, beside the relaxation of stress and vacancy density, the introduced grain boundaries provide transport paths along which Cu and Au can intermix quickly. A complete transformation of the volume is achieved by the migration of these boundaries (DIGM), so that the boundary mobility becomes the dominating factor to control the kinetics. Regarding this boundary migration mechanism, the described second interdiffusion stage develops quite similar to the intermixing observed in nano-crystalline Pb/AgPd [92] and Ag/Pd layers [31, 32], where grain boundaries were existent from the very beginning. However in our epitaxial specimens, the reaction takes an additional important step in producing the necessary transport paths by itself to accelerate the kinetics. This has an important consequence to the design of diffusion barriers, where it is an accepted rule to avoid grain boundaries. In the case of lattice mismatched systems this might not be sufficient.

It is remarkable that already in 1983 den Broeder et al. [112] compared the interdiffusion in the reactive systems Cu/Al and Au/Al, where the respective

lattice mismatch is quite similar to that of the Cu/Au and Ag/Au studied here. They noted that only in Cu/Al migration of grain boundaries is observed, but could not work out a clear reason for the difference between both systems. From the actual point of view, it is quite clear that the lattice mismatch between the reacting materials is the important factor.

It was already pointed out that the preferred compositions observed in the reaction zone are not stabilized by thermodynamic reasons but must be controlled by the kinetic process. It seems to be quite clear, that the composition inside the newly formed grains must be controlled by the balance between the grain boundary migration velocity and the transport of atoms through the grain boundary [93]. However, it is striking that the finite composition difference between the pure materials and grains of first generation and that between grains of first and second generation are almost identical, although in the latter case the grain boundary diffusion should be already significantly slowed down as part of the driving force is already degraded. The close correspondence between the composition difference and the elastic solubility limit of about 20 at% predicted by Eq. 38 suggests that these two phenomena are somehow related, but no clear relation could be worked out yet.

4.4.3 Consequences to the formation of ordered compounds

All data presented so far were addressed to the interdiffusion of Cu and Au at temperatures that exclude the formation of ordered compounds. However, the identified two-stage reaction mechanism is also effective at lower temperatures, where the ordered compounds Cu_3Au, CuAu and $CuAu_3$ may form. Studying the isothermal reactions at 230 °C and 350 °C by TEM and XRD yields a very similar microstructural development, characterized by the initial planar defect zone and the 'inverse' recrystallization mechanism [63]. Remarkably, the maximum width of the defect zone developed at 230 °C amounts to 15 nm, almost identical to the width determined at 430 °C, which confirms the existence of a maximum diffusion length in the first reaction step. Only the time scale must be adjusted to the reduced atomic mobility. The incubation period of the second reaction step is determined to > 1 min and > 220 min at 350 °C and 230 °C, respectively. Thus, the influence of the phase formation on the mixing kinetics seems to be negligible.

This behaviour can be elucidated by the thermograms presented in fig. 43 which were obtained during first (solid line) and second (dashed line) heating of Cu/Au multilayers of 30 nm single layer thickness. The exothermic peak A is related to mixing and the endothermic peak B to disordering. Comparing the related peak areas, it is quite obvious that the ordering enthalpy amounts to at most one third of the mixing enthalpy, $\triangle H_{mix} = 40.4$ J/g, $\triangle H_{order} = 13.6$ J/g (see also data by B. Sundman et al. [113]). Thus, the dominating driving force
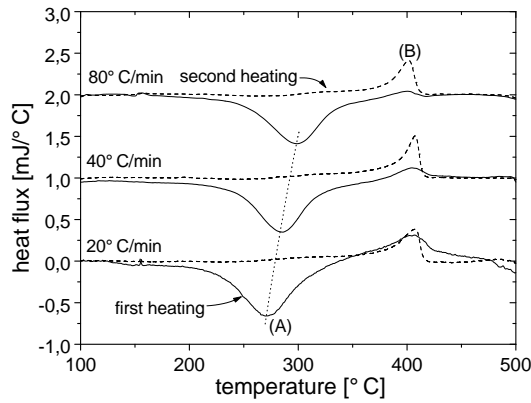
Figure 43: DSC measurement of the reaction of a Au/Cu multilayer (50 nm single layer width). First heating is shown by solid lines, second heating by dashed lines. The shift of the exothermic peak (a) with heating rate is emphasized by a dotted line.

of the reaction is due to mixing while the lattice order provides only a minor contribution. Furthermore, comparing the mixing and disordering peaks of first heating with 80°C/min, it is seen that intermixing is almost completed after heating to 400 °C, whereas ordering is significantly suppressed. Obviously, instead of being concomitant, mixing and ordering are subsequent processes, where the major gain of free energy is already achieved by the first mixing reaction. Thus, it is not surprising, that above and below the ordering transition temperature, a very similar structural transformation is observed.

Already very early, Tu and Berry [114] studied the interreaction of Cu/Au thin films by X-ray diffractometry and Borders [115] by Rutherford backscattering. Both experimental techniques do not provide lateral information on the required scale of 10 to 100 nm. Furthermore, the existence of ordered reaction products was not explicitly proven e.g. by superlattice reflections, but only concluded from the composition of the reaction zone. Because of insufficient lateral information, both studies could only assume the formation of planar product layers. However, our microscopic investigation demonstrates that this assumption is certainly not valid. As his RBS analysis averaged laterally on regions of different reaction progress, Borders observed a continuous transition instead of different plateaus in composition profiles normal to the interface. Tu and Berry derived from reflection intensities in their X-ray spectra a reaction kinetics linear in time which they claimed to be caused by a kinetic barrier at the interface between ordered and disordered phases. Beside the drawback that their data analysis relied on a persistent layer geometry, our results demonstrate, that the overwhelming part of the mixing reaction proceeds without pronounced ordering. Thus, deviation from parabolic growth must be explained by the required nucleation, grain boundary transport and migration and the very complicated morphology of the reaction zone. As this factors are effective above as well as below the order transition temperature, no dramatic change in the mixing kinetics is seen between these two temperature regimes, in contradiction to the assumption of Tu and Berry.

4.5 Conclusions

The interdiffusion in the lattice mismatched system Cu/Au is accomplished by important microstructural transformations. With increasing diffusion length, a transition from a semi-coherent mechanism to an incoherent, discontinuous mechanism takes place. In particular we have to state that

- during the first semi-coherent reaction stage, the relaxation of mismatch stress and the required adaptation of lattice orientation is achieved by climbing and gliding of dislocations. Continuous composition profiles indicate, that misfit stress is efficiently relaxed. However, the coherency constraint induces a vacancy depletion, which cause the coherent planar interdiffusion to stop.

- during the second reaction stage, interdiffusion is achieved by recrystallization and diffusion induced grain boundary migration. Because of heterogeneous nucleation, the layer like geometry is destroyed. The size of the nucleated grains and the necessary incubation time is understood, if only the elastic contribution to the free energy is accounted as driving force for microstructural transformations.

- studies of the reaction at lower temperatures, at which the formation of ordered compounds is expected, demonstrate that the identified discontinuous mechanism is effective also in the case of reactive diffusion (see details in [63]). This is explained by the low ordering enthalpies of the compounds in CuAu. In consequence, also the interreaction of Cu/Au proceeds very heterogeneously, so that the initial layer geometry is destroyed.

5 Nano-analysis of the interreaction of Ag/Al

Until very recently, Al has been the preferred material for connecting lines in microelectronic devices[7]. At cross links, solder connections and electrodes these lines contact a variety of other metals. Hence, it is not surprising that especially metallic reactions with Al attracted considerable scientific attention, which triggered numerous measurements by Rutherford backscattering and X-ray diffraction. However, since the information limit of those methods has been reached, the interest diminished somewhat during the last decade. With the experiments presented in the following the subject is taken up again, as the progress in analytical field ion microscopy let us expect detailed insight into processes, which could be only concluded indirectly in the past.

The binary reaction couple Al/Ag qualifies as a particular clear model system to study the kinetics of interreactions. Both pure metals have an fcc structure of almost identical lattice parameter, so that stress effects as discussed at the previous example of Cu/Au are not expected to be important. Two stable intermetallic compounds are seen in the phase diagram (see fig. 44). Besides, a metastable fcc solution of 30 to 60 at% Ag is well known to appear as GP-zones in supersaturated AlAg alloys [116]. In thin film interreaction experiments, only the formation of the γ phase has been observed [117]. The existence range of this phase close to the 2:1 stoichiometry suggests an ordered superlattice structure. However, diffraction methods failed to prove any long range order, yet. The second equilibrium compound μ is kinetically suppressed, presumably because of its complicated cubic structure containing 20 atoms inside the unit cell.

In an early study at Ag/Al bi-layers, Weaver and Brown addressed the formation of the γ phase by a tricky measurement of optical reflectivity [118]. For layers thicker than about 100 nm, they observed ordinary parabolic growth, with a reasonable activation energy of 1.15 eV. Surprisingly, they noticed that the re-

---

[7]These days, Al is being replaced by Cu to prevent electromigration which gets increasingly important with decreasing line width.
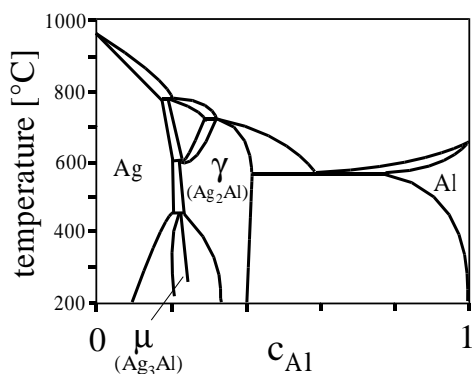

Figure 44: Phase diagram of AgAl

action proceeds an order of magnitude faster in very thin layers below about 50 nm single layer width. As no change in the corresponding activation energy is observed, the authors ruled out the eventual influence of grain boundary diffusion and explained their observation by an initial vacancy supersaturation. By RBS profiling, the parabolic growth in later stages has been confirmed [117] and also the fast initial reaction [119]. In addition, both RBS studies noticed that unexpected slopes in the backscattering spectra contradict a layer-like morphology of the compound in early reaction stages. Either precursory interdiffusion of Ag and Al or very rough layer interfaces are required to explain the experimental data. Furthermore, Bagley et al. [117] re-determined the activation energy of growth to 0.86 eV, which is close to the activation energy of grain boundary self diffusion in Ag. Hence, they suggest that the reaction takes place predominantly inside silver layers controlled by grain boundary diffusion. This is further indicated by a strong dependence of the growth rate on the grain size of the deposited Ag layers.

Evidence for the importance of microstructural effects stems also from calorimetric measurements by Roy and Sen [38]. Similar to several other metallic reaction pairs, a double-peaked heat release is observed. As the second release gets dominant with increasing layer thickness, the result is interpreted as evidence for the two reaction stages i) heterogeneous nucleation and lateral growth along the interface and ii) thickness growth after forming a dense product layer as proposed by Coffey et al. [36] (see section 2.4). However, applying this model quantitatively, the thickness of coalescence is determined to 50 nm, which is probably too large to be explained by nucleation taking place at the initial interface, exclusively.

All the cited experimental work suggests strongly that the early interreaction of Ag and Al deviates from a simple layer growth and that microscopic features are dominant in determining the reaction kinetics. However to prove this hypothesis, atomic transport paths must be verified by local chemical analysis.

5.1 Cross section electron microscopy

The reaction of sputtered Ag/Al multilayers has been studied by Schmitz and coworkers using Z-contrast electron microscopy [120]. HCDF images obtained at the as deposited specimen and after a low temperature heat treatment are compared in fig. 45. In the presented specimen area, silver rich regions are distinguished by an increased intensity. Indeed, a pronounced Ag segregation is observed at grain boundaries of the Al layers. The quantitative analysis of the image contrast revealed a composition amplitude at the boundaries of up to 30 at% Ag (see the quantitative composition profiles in fig. 45c). This value must be interpreted as a lower limit of the local Ag enrichment. Because of the complicated nanocrystalline microstructure, a proper alignment of the boundaries along the
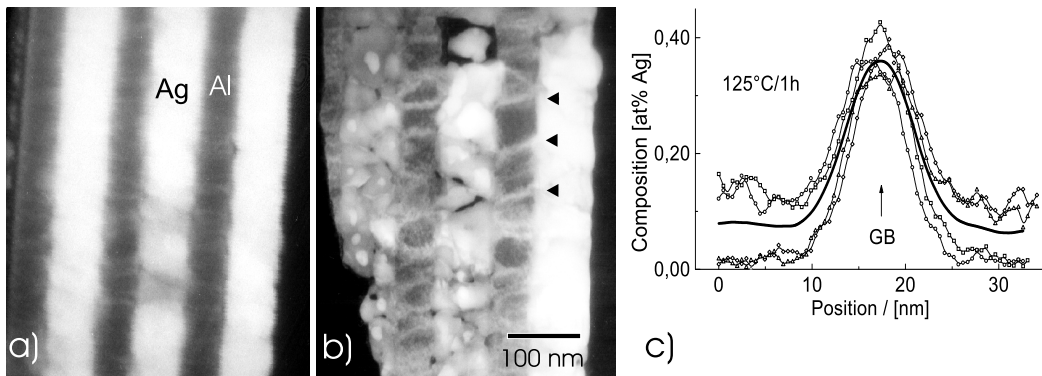
Figure 45: HCDF images of a cross section through a $(Ag_{90nm}/Al_{60nm})_3$ multilayer. a) as prepared state b) after 1 h heat treatment at 125 °C. Some Al grain boundaries are marked by arrow heads, c) exemplary composition profiles across grain boundaries inside the Al layer as determined from image intensities. (At the presented thickness range Ag rich regions are always imaged brightly.)

electron beam is almost impossible. Thus, the spatial resolution of the analysis might be very limited, so that the amplitude of the segregation is underestimated whereas the width gets overestimated.

In contrast to the Al layers, at the former Ag layers thinning becomes very heterogeneous after the heat treatment, so that a reliable analysis of the image intensity is impossible. But the mere fact of inhomogeneous etching indicates pronounced chemical or structural heterogenities, which have evolved during the heat treatment. Therefore, it is suggested in agreement to the conclusion of the cited RBS measurements that the reaction proceeds predominantly inside the Ag layer. This somewhat unsatisfying result regarding the Ag layers demonstrates typical difficulties with electron microscopy stemming from nanocrystalline microstructures and unfortunate specimen preparation. Therefore, the complementary atomprobe analysis is highly recommended, even though it requires tedious preparation work.

5.2 Results of atomprobe tomography [76]

Al/Ag-bilayers of about 40 nm double layer thickness were deposited on tungsten substrate tips by sputtering as described in section 3.2.3. The actual layer thickness varies somewhat with shaft angle and radius of the substrates. Both layers show a nanocrystalline structure. Various heat treatments were performed in an UHV furnace. In principle an isothermal measurement scheme restricted to a unique annealing temperature would be favorable to facilitate the physical understanding. However, it turns out that the kinetics of different reaction stages is too different to record the complete transformation at a unique temperature.
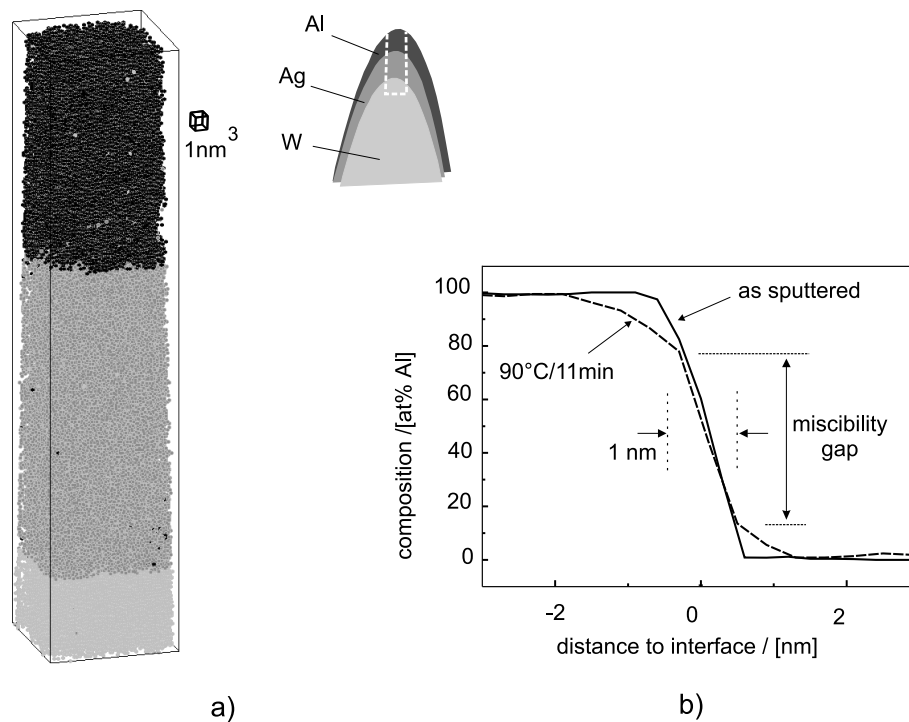
Figure 46: a) Reconstructed atom distribution of a Ag/Al bi-layer in the as-deposited state. b) composition profiles determined normal to the Ag/Al interface in the as-deposited state and after a short annealing treatment

A reconstruction of the atom distribution in the as-deposited state is shown in fig. 46a. Planar interfaces are found on the lateral dimension of the investigated volume. To evaluate the atom distribution in detail, composition profiles are calculated normal to the interface as shown in fig. 46b. The depth of the chemical transition from 10 to 90 at% Al is determined to 1 nm. After 11 min heat treatment at the very low temperature of 90 °C, no qualitative change is seen in the reconstructions. Nevertheless, comparing the composition profiles at the interface, significant differences are revealed because of the outstanding resolution of the atomprobe. Solution zones of about 2 nm and 1 nm width have formed at the Al and Ag sides of the interface, respectively. It is instructive to compare these diffusion lengths with those expected from bulk diffusion. Extrapolating literature data to the present annealing temperature, the maximum diffusion width is estimated to 2.5 Å and 0.002 Å inside the Al and Ag layer, respectively. Thus, the observed mixing is probably not explained by ordinary volume diffusion. Since no influence of grain boundaries is noticed within the analysed volume, one has to assume that diffusion is accelerated by an initial vacancy supersaturation stemming from layer deposition. In addition, if the shape of the profile after the heat treatment is compared to the initial one, a miscibility gap is indicated, ranging
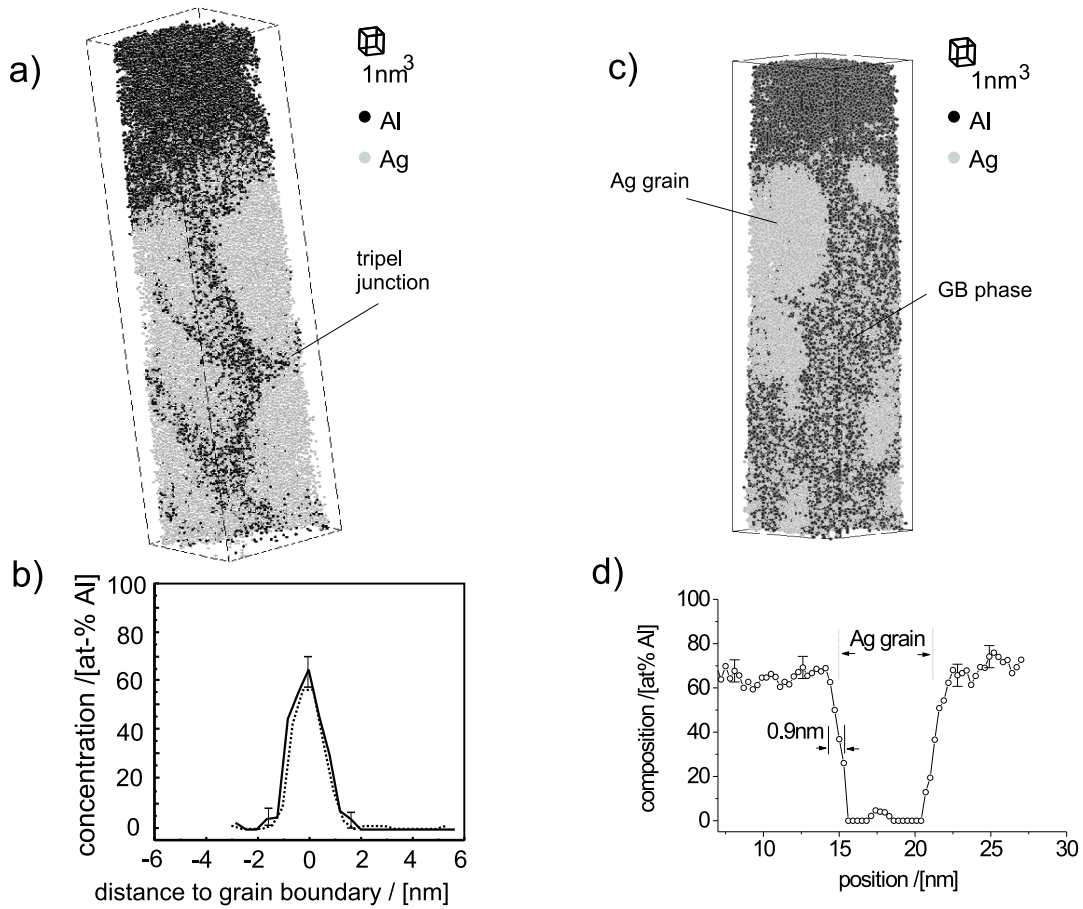
Figure 47: a) Reconstructed atom distribution of a Ag/Al bi-layer after annealing at 100 °C for 15 min. b) composition profiles across the grain boundaries determined close to the triple point marked in a. c) atom distribution after 15 min annealing at 115 °C.

from about 10 at% Al to 20 at% Ag. This is in agreement with the thermodynamics of the fcc phase, as the formation of Ag rich GP zones in supersaturated Al alloys points out a tendency of decomposition. It is remarkable that at least at the Al side, the solute concentration significantly exceeds the solubility limit of the equilibrium phase diagram. Thus, up to this point the reaction seems to follow exactly the nucleation scheme as discussed by d'Heurle; at first, a supersaturation is built up by interdiffusion to establish the driving force required for nucleation [15].

Surprisingly, the reaction leaves this ideal scheme in subsequent stages, as is seen in remarkable clarity by the volume reconstruction obtained after annealing at 100 °C for 15 min (fig. 47a). Al rich shells surround Ag volumes of 5 to 10 nm diameter. The agreement of this size to the grain size observed by electron microscopy, leads to the conclusion that Al diffuses along the grain boundaries of Ag. Very high Al concentrations are found, which exceed the Al content of
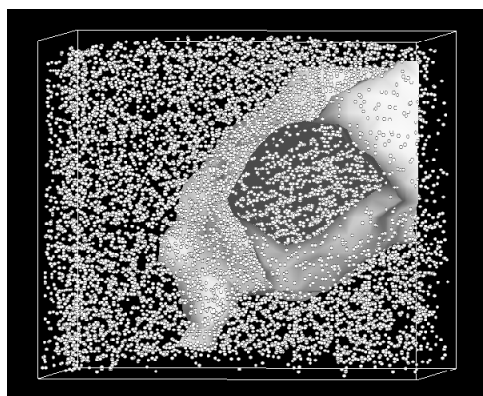
Figure 48: Enlarged detail of the measurement shown in fig. 47c). The iso-concentration surfaces at 90 at% Ag envelop the Ag grains. Inside a grain lattice planes are resolved. However, they are not continued into the Al rich product phase.

the expected equilibrium γ phase significantly. For example, the composition profiles in fig. 47b are determined close to the triple junction marked in fig. 47a. Up to 60 at% Al are proven, twice the content of the hexagonal γ phase. The Al rich shells grow towards the center of the Ag grains during further annealing (see fig. 47c, after 15 min annealing at 115 °C). The interface between the grain boundary phase and the remaining Ag appears always very sharp. The observed composition gradient is at least comparable to that measured at the initial layer interface, as shown in fig. 47d. Hence, this boundary must be interpreted as a real phase boundary. In some fortunate cases, the reconstructions indicate furthermore that this boundary is even an incoherent one. This is demonstrated by the reconstruction shown in fig. 48. Inside the Ag grains lattice planes are clearly resolved. However, the planes are not continued into the Al rich boundary phase.

By consumption of the Ag grains, a dense, Al rich layer is formed, which is seen in the two-dimensional composition map determined along a section through the tip apex after 30 min heat treatment at 140 °C(fig 49a). Beside the remaining pure Al and Ag, clearly a third intermediate layer is distinguished. The composition of this layer matches a stoichiometric ratio of Al_2:Ag_1 (see the corresponding concentration profile in part b of the figure); a phase of this composition does not appear in the equilibrium phase diagram. The formation of this phase was confirmed in eight independent measurements. In the remaining Ag layer (bottom of the composition map) again grain boundary transport of Al is observed.

The analysis of even later stages suggests, that the expected equilibrium phase is formed by a gradual adjustment of the average composition to the equilibrium of about 60 at% Ag[8] accompanied by a decomposition process taking place inside the layer. This is seen in the composition map obtained after a heat treatment 250 °C/30 min (see fig. 49c) and the cluster distributions shown in fig. 50. Globular Ag enrichments are observed in the composition map. To test the significance

---

[8]As both layers have been deposited in comparable thickness, the final state is given by an equilibrium of terminating Al and Ag_2Al.
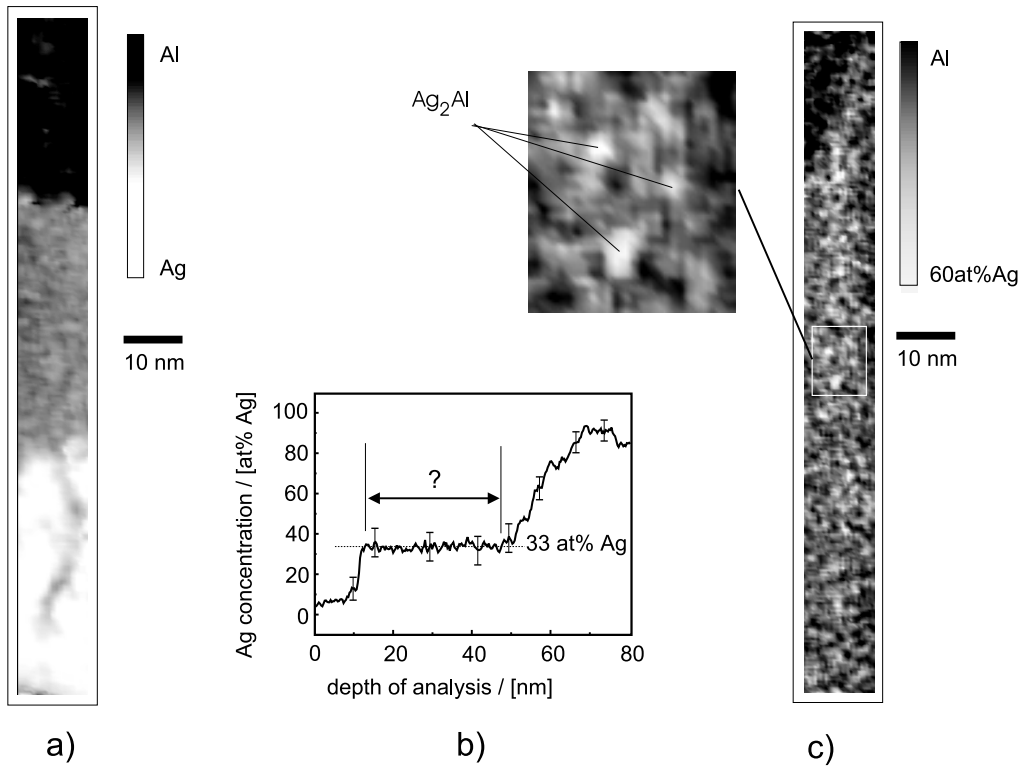
Figure 49: a) two-dimensional composition map (a) and composition profile (b) along the tip axis, obtained after annealing at 140 °C for 30 min. c) composition map after 30 min annealing at 250 °C.

of these compositional fluctuations, the reconstruction of the metastable layer is subdivided into small volumes containing 100 atoms each. The frequency of volumes with a given fraction of Ag atoms is plotted in fig. 50 for four different annealing stages. In the case of a homogeneous alloy, the cluster distribution should match a binomial one [50], which is plotted for comparison by a dashed line. The states after annealing at 140 °C and 300 °C are identified by a χ^2 test as homogeneous, even though with a very different composition. In the intermediate stages after heating at 200 and 250 °C, clusters of low and high Ag content are more, those with average composition less frequent than predicted by the binomial. The statistical test proves these cases indeed as significantly heterogeneous [73]. At the same time, the average composition of the clusters is shifted towards that of Ag_2Al during the heat treatment. Obviously, a continuous transition exists between the observed intermediate phase and the final equilibrium compound.

It is surprising, that the presented atomprobe analysis identifies the reaction as restricted to the Ag layer, although electron microscopy revealed significant diffusion of Ag into the Al layer along grain boundaries (see fig. 45). However,
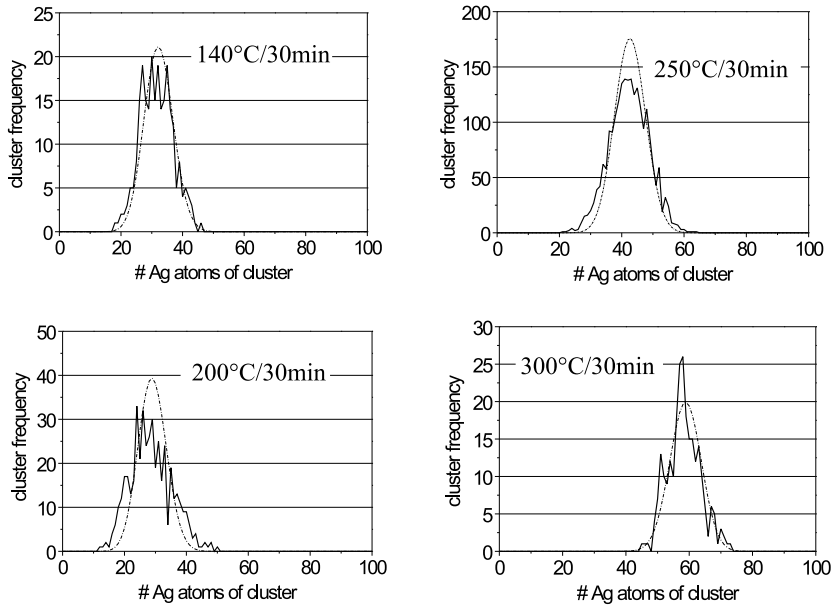
Figure 50: Composition distribution of atomic clusters inside the intermediate layer determined in four different reaction stages (Cluster size 100 atoms).

when comparing atomprobe results to electron microscopy, one has to keep always in mind that the volume analyzed by the atomprobe is still very small. Hence, the probability to observe a grain boundary might be very low, if the grain structure of the Al layer is somewhat coarser than the Ag microstructure. In addition, the growth condition on top of the curved substrates seems to favor the formation of one Al grain at the tip apex, so that just in the measurement volume no grain boundary is formed.

To overcome this difficulty, the layer sequence was modified, so that an Al layer of only 6 nm thickness is sandwiched between thicker Ag layers. This way, the formation of very small Al grains is forced. Although the experimental rule to deposit layers in the order of decreasing evaporation field strength is violated, a few measurements were successful. An example after 30 min heat treatment at 150 °C is shown in fig. 51. Indeed, a grain boundary is recorded inside the Al layer, as is indicated by the two-dimensional Ag enrichment spreading between the two Ag layers. Remarkably in this case, the segregation amplitude amounts already to 60 at% Ag. Obviously, opposed to the reaction inside Ag, at the Al grain boundaries the composition of the equilibrium γ phase is established directly, without the intermediate formation of an Al rich solution. On the other hand, the reaction proceeds much slower, which becomes pretty clear, when the thin segregation zone of fig. 51 is compared with the metastable layer of almost 40 nm thickness formed inside the Ag layer during a comparable heat treatment.
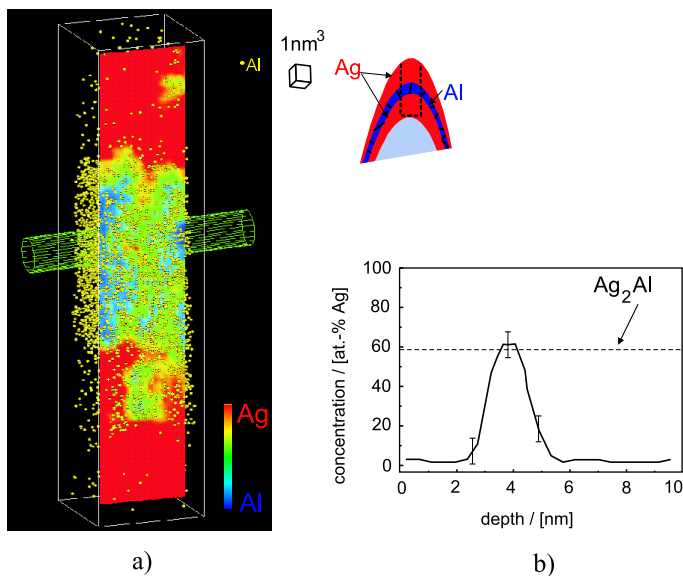
a)   b)

Figure 51: Analysis of a triple layer $Ag_{20nm}/Al_{6nm}/Ag_{20nm}$ after 30 min annealing at 150 °C. a) 2D-composition map superposed with detected Al atoms. b) composition profile through the grain boundary. The sketched cylinder in a) indicates the volume used to determine the profile in b).

5.3   Discussion

The presented experimental results demonstrate the significant gain of information that is obtained by the atomprobe analysis of thin film reactions. It is clearly shown that a three-dimensional reaction morphology develops, forced by the nanocrystalline nature of the thin films. The formation of an unexpected intermediate non-equilibrium phase is discovered and furthermore a remarkable asymmetry between Ag and Al layers is proven. On the other hand, apart from a few favorable cases[9], the atomprobe analysis yields only a reliable chemical analysis but no structural information, so that complementary methods must be applied to obtain a complete picture of the reaction. This disadvantage becomes especially obvious, if the metastable phase should be identified structurally. Thus before discussing potential reaction mechanisms, we have to consider at first the potential structure of this phase.

5.3.1   Structure of the intermediate phase

In order to identify the observed intermediate phase, results of field ion microscopy might be compared to those of X-ray diffractometry. A few X-ray measurements of Ag/Al are reported [117, 38, 120]. All these studies agree that beside fcc Ag and Al, only reflections of the disordered hcp phase Ag_2Al are found in significant amounts. Also, electron diffraction revealed these two structures exclusively [121]. As the nature of the intermediate phase is rather important for the understanding of the reaction mechanism, the X-ray diffractometry was re-confirmed

---

[9]A most impressive example was given by Blavette and coworkers, who were able to determine an edge dislocation in the reconstructed atom positions [122]

at planar multilayers. For that, the same deposition system as for the FIM prepa-
ration was used and in addition the single layer thickness was chosen comparable
to that on the tip-shaped substrates. Spectra obtained during an isothermal an-
nealing at 115 °C are shown in fig. 52a. Even in the earliest stages, all intensity
maxima are related either to the fcc or the hcp phase and no evidence for another
intermediate lattice structure is seen. Hence, the choice of possible structures
seems to be restricted to disordered fcc or hcp solutions. Because of the identical
atomic volume of Ag and Al, compositional changes within the phases cannot
be detected by a peak shift. The fraction of the hexagonal phase is determined
from the intensity ratio of the corresponding reflections, as shown in fig. 52b for
two different annealing temperatures. The formation of the hcp phase proceeds
with two well distinguished regimes; a quick first reaction with time exponents
exceeding 2 is followed by a very sluggish approach to the equilibrium. This sec-
ond stage of the reaction is so slow that elevated temperatures are necessary to
complete the transformation in a reasonable experimental time.

As a metastable fcc phase is known from decomposition experiments [116],
the assumption is quite obvious that the intermediate phase observed with atom-
probe tomography has an fcc structure, and this suggestion was made in an early
report[73] of the measurements. However, there are two important facts which
contradict this conclusion: i) the observed continuous transition of the metastable
layer into the equilibrium phase would be very unlikely, if the structure had to
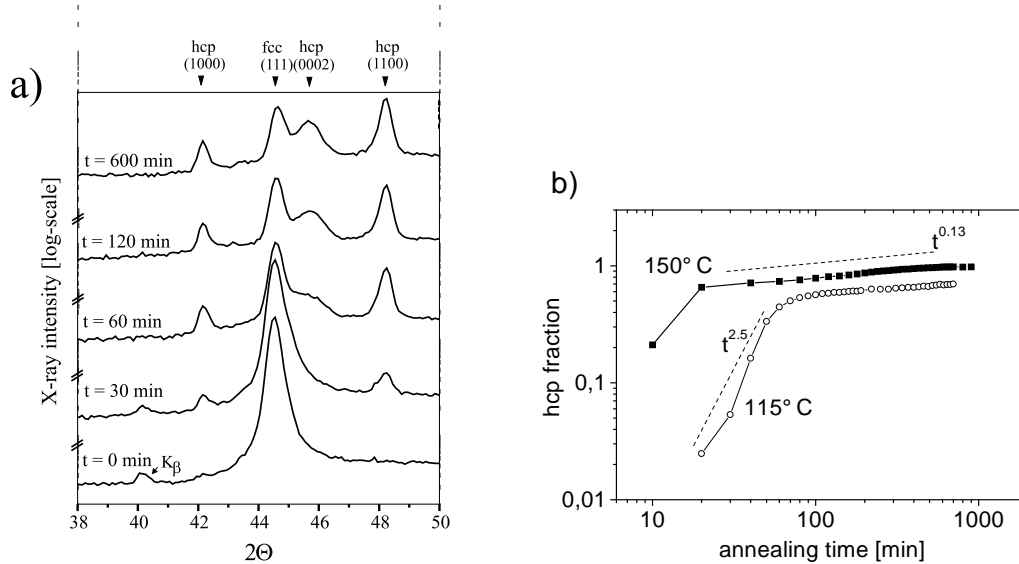

Figure 52: X-ray diffractometry of the interreaction of a Ag_{30nm}/Al_{30nm} multilayer.
a) Spectra obtained during annealing at 115 °C, b) development of the hcp fraction
determined from the relative intensity of fcc and hcp reflections during annealing at
115 °C. and 150 °C. (As the scattering cross section of Al is very low only Ag atoms are
'seen' by X-ray spectroscopy.)

be switched from fcc to hcp; ii) X-ray diffractometry reveals already considerable amounts of hexagonal phase at stages when atom probe tomography still indicates only the presence of the intermediate layer. Compare for example the cluster distribution in fig. 50 after 30 min annealing at 200 °C, with still an average composition of about 30 at%Ag, to the hcp fraction determined after the same annealing time at the even lower reaction temperature of 150 °C in fig. 52b. Considering these facts, only the hexagonal structure is a reasonable conclusion for the observed intermediate layer. This has important consequences to the description of the reaction mechanism. Obviously, the reaction leads directly to the formation of an hcp γ phase, which is naturally expected from the phase diagram; but the composition of this phase is kinetically stabilized way off the equilibrium. This behaviour is quite remarkable, as usually metastable intermediate phases are reported to differ in their lattice symmetry from the competing equilibrium products, as in the famous example of solid state amorphization. Only very little attention was devoted yet to deviations of expected products from their equilibrium configuration.

5.3.2 Reaction mechanism

The result of the nano-analysis and the identification of the first product allow to state the following reaction mechanism (an illustration is given in fig. 53). The early interreaction takes place predominantly inside the Ag layer. Fast grain boundary diffusion allows Al to diffuse deeply into the Ag layer and to envelop the grains by an Al rich shell. At the grain boundaries, the hexagonal γ phase is nucleated similar as observed during the decomposition sequence of supersaturated AlAg alloys [123], but forced by the fast transport, a non-equilibrium composition of about 66 at%Al is stabilized in the growing hcp layer. Only after consumption of the remaining Ag inside the grain, the transport of Ag through the γ phase ceases, so that the adjustment of the hexagonal phase to its equilibrium gets possible. For that, volume diffusion is required inside the already present hexagonal phase. This process might become very slow, if the diffusion rate in the hexagonal phase is decreased with increasing Ag content. Thus, the equilibrium is approached only slowly. Hence, either very long annealing times or elevated temperatures are required to reach the equilibrium state, as is confirmed by the X-ray measurement in fig. 52b.

It is remarkable, that this reaction scheme is very similar to that assumed already by Baglin et al. [117], to explain their RBS spectra. However, the essential additional feature is the stabilization of a very significant composition deviation inside the growing compound shells, which allows important conclusions on the physics of early reaction stages. Beside still justified scepticism regarding the structure of the compound [10], its composition far off the equilibrium must be

---

[10]X-ray diffraction could not be performed at the tip-shaped specimens. Hence, there is a
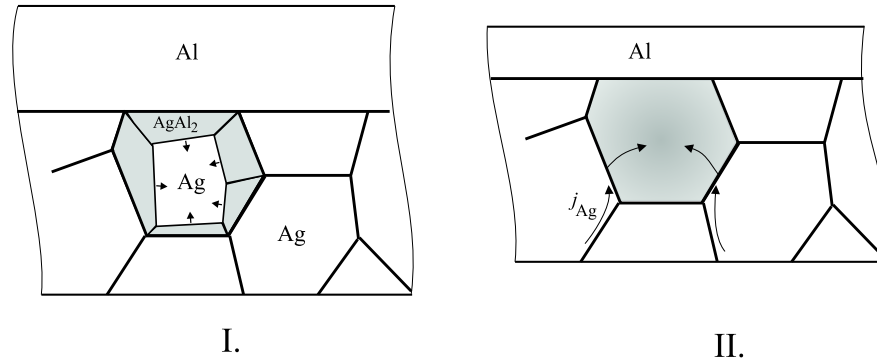
Figure 53: Schematic of the initial reaction in Ag/Al according to the nano-analysis. Only one grain is shown in detail. Grey shaded areas mark Al enriched regions. During the first stage, an Al rich intermediate phase is formed by a discontinuous reaction. In a later stage, this phase is adapted to the equilibrium by volume diffusion.

taken as matter of fact. Furthermore, all the cited previous studies do not contradict the determined off-equilibrium composition, as the 3D reaction morphology would always result initially in continuous RBS composition profiles, regardless of the actual composition inside the reacted regions.

The described reaction mechanism makes clear, that in the case of Ag/Al, double-peaked thermograms of the reaction must not be interpreted as nucleation and growth of a unique reaction product as was done by Roy and Sen [38]. Instead the first heat release observed at about 160 °C at a heating rate of 20 K/min, is more likely related to the formation of the off-equilibrium γ phase and the second at about 190 °C to the transition into the equilibrium phase superposed by thickness growth. Therefore, the surprisingly large thickness of coalescence (50 nm) determined by Roy and Sen must be considered as an artefact of an inappropriate model.

5.3.3 Towards a physical understanding

Certainly, the determined mechanism is considerably more complex than layer growth of equilibrium compounds, so that a quantitative description of the kinetics has not been achieved yet. Unfortunately, even very fundamental parameters of the Ag-Al system are rather unknown. In particular, the composition dependence of the diffusion inside the hexagonal γ phase has not been measured (see for reference e.g. [100]) and the free energies of the different phases are not modeled yet [124]. But nevertheless, the physical basis of the reaction process might be discussed regarding well known features of the binary system.

theoretical chance, that the reaction develops different in planar and curved layer geometries.
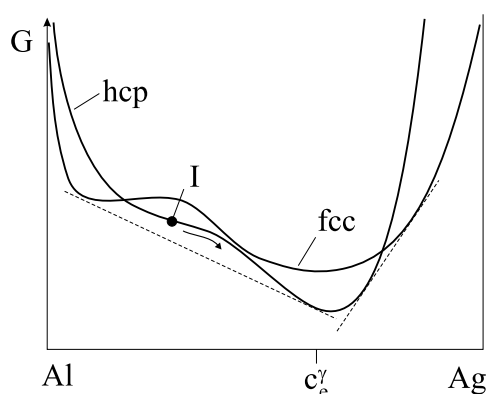
Figure 54: Schematic free energy curves of AgAl. Only the fcc and hcp phase are considered. The point at the hcp curve marks the state that is kinetically stabilized initially.

Phase stabilities Decomposition studies reveal the formation of metastable GP zones, having an fcc structure and a temperature dependent composition from about 35 at%-Ag at 300 °C to about 55 at%-Ag at 100 °C. Thus, the free energy of the fcc solution must certainly reflect a decomposition tendency. As the coordination of the fcc and the hcp structure are very similar, it is reasonable to assume that apart from the relative stabilization of the hcp structure at intermediate compositions, both free energy curves behave very similar. Hence, a miscibility gap is also expected for the hexagonal structure. Since the stacking sequence is essentially determined by weaker second neighbor bounds, presumably, the relative stability of the hcp phase is not that pronounced. This is indicated in addition by the broad existence range of the terminating Ag phase.

In fig. 54 schematic free energy curves are proposed accounting for the described situation. Both solutions are distinguished by a decomposition tendency on the Al-rich side. Especially within the miscibility gaps, the stability of both solutions might become very similar. However, no physical reason contradicts the assumption that there the hcp solution is still more stable than the fcc one. Thus, a driving force to form the hexagonal solution at the grain boundaries is present even though the average composition is driven to a non-equilibrium point (I) as marked in the figure. In later stages, when the transport rate decreases, this phase will start to decompose as indicated by the cluster analysis shown in fig. 50, eventually even by a spinodal mechanism. However, these decomposition will not proceed into its final heterogeneous state, since at the same time, the average composition of the intermediate layer shifts towards the equilibrium composition c_e^γ of the γ phase.

In the previous discussion, the term 'metastable' was carefully avoided to characterize the observed intermediate phase, as it is not sure, whether this state is really a metastable one, i.e. with a local minimum in the free energy, or just a steady state determined by the balance of atomic fluxes. The homogeneous composition of the intermediate layer observed after annealing at 140 °C, may be interpreted as evidence for a distinct metastable phase, on the other hand the ex-

perimentally proven continuous transition into the equilibrium state contradicts this interpretation. Furthermore, one should be reminded to the presented inter-diffusion study on Cu/Au, where distinct compositions in the reaction zone are found in disagreement with thermodynamic stabilities. Without detailed analysis of the thermodynamics by CALPHAD methods, this question cannot be finally answered.

Kinetic stabilization of the intermediate phase From a physical point of view, the stabilization of off-equilibrium compositions in the hexagonal phase is a most attractive aspect. It is really astonishing, that although the reaction starts inside pure Ag and the required Al must be transported into the reaction zone, nevertheless an Al rich precursor is formed. To consider the kinetic conditions, in fig. 55 literature data of volume diffusion [100] are shown, extrapolated to the low reaction temperatures. Most striking is the significant difference of the diffusion rates in Al and that in Ag, which is easily understood by the different melting temperature of both metals. Furthermore, in the terminating Al phase, the diffusion has been found to be only weakly dependent on the composition, whereas at the Ag side, the mobility increases significantly with increasing Al content [100]. No data of the composition dependence of the diffusion coefficient in the hexagonal solution are known, so that we are restricted to a plausible guess. Because of the identical first neighbor bounds in both structures, probably the composition dependence of the diffusion in the hexagonal solution is not that different from the fcc phases. In consequence, it is very reasonable to assume that the diffusivity of the hexagonal structure increases also significantly with the Al content.

By Bené, the principle of *'maximum gain in free energy'* was formulated [19] to explain the formation of amorphous phases by solid state interreactions. Applying this principle to the case under consideration, it is suggested, that an Al rich composition is stabilized in the hcp compound, since this way the transport and thus the overall reaction rate is significantly accelerated. In this context, it is quite remarkable that the composition initially observed in the intermediate phase is close to the eutectic point of the system, where, according to the basic assumption of Pretorius' phase selection rule, the highest mobility is expected. This general principle is useful to summarize a general trend of early interreaction stages. However, one has to be aware that a real microscopical justification of the ansatz is still lacking.

The nano-analysis and the presented considerations lead us to the statement, that already the interreaction of Ag and Al, although initially thought to be a particularly clear and simple model case, raises very attractive problems regarding phase stability, which must be addressed by a theoretical modeling beyond near equilibrium thermodynamics. In addition to the discussed points other aspects are even more unclear and await a detailed kinetic explanation. Most prominently
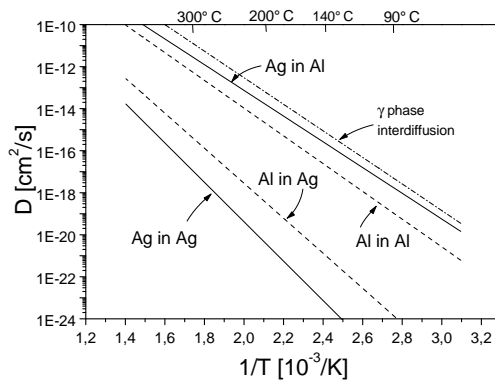
Figure 55: Expected diffusion rates in the Ag-Al system, as calculated from data in [100]

one might ask for the reason of the remarkable difference of the reaction rates inside the Al and Ag layers. Even though the grain boundary diffusion of Al is expected to be significantly faster [117], the reaction proceeds very slowly compared to the Ag layer. According to the nano-analysis, the obvious reason is that in the case of Al, the reaction product is formed directly with the equilibrium composition, which slows down thickness growth as a Ag rich solution, be it fcc or hcp, has only a low mobility. But how is this asymmetry between Ag and Al understood kinetically? Very likely, the answer to this question will improve our general understanding of nucleation at grain boundaries which is an important prerequisite for the reaction also in other couples. For example, in the case of the solid state amorphisation of Ni/Zr, grain boundaries inside Zr have been shown to initiate the reaction [27].

5.4   Conclusions

Atomprobe tomography of the interreaction of Ag/Al reveals important microstructural features that control the kinetics of the reaction. It is shown that

- a complicated three dimensional reaction morphology develops because of the nancrystalline nature of the metallic films. The reaction is not described appropriately by a planar layer geometry as long as the thickness of the reacted zone is below about 100 nm.

- an appreciable amount of early reaction products forms predominantly inside the nano-crystalline Ag layer with a grain size of 5 to 10 nm diameter. Al wets the grain boundaries of Ag in a composition of up to 60 at% Al. The hexagonal lattice structure nucleates at the grain boundaries and grows subsequently into the silver grains until all Ag is consumed.

- Under the condition of fast transformation, at first, this hexagonal phase is stabilized way off its equilibrium with an Al content up to 66 at% Al. The

composition of the hexagonal phase approaches gradually the equilibrium only after the transport rate has slowed down.

- Based on plausible arguments, it is suggested that this deviation from equilibrium is due to the faster atom transport in Al rich alloys, which allows the higher reduction rate of the system's free energy.

- At the grain boundaries of the Al layer, the hexagonal γ phase is nucleated directly in its equilibrium composition. The amount of γ-phase formed at early stages inside the Al layer remains small because of the smaller number of grain boundaries in Al and the sluggish growth of the γ phase in its equilibrium configuration.

6 Interreaction of Ni/Al [125]

In contrast to the previously considered case of Ag/Al, the reaction of Ni and Al attracted already considerable interest, so that a large amount of experimental data are available. In the lower part of fig. 56, a phase diagram containing the relevant phases observed during thin film interreaction is shown. Early work, mainly based on RBS, revealed the phase formation sequence of the equilibrium phases in the order of increasing Ni content [126, 127, 128, 129, 130], with the exception of the Ni_5Al_3 phase. This phase sequence agrees with the prediction of the *effective heat of formation rule* by Pretorius et al. [131], as the effective heats of formation at the composition of the lowest eutectic indeed appear in the order of decreasing Al content (see top of fig. 56). On the other hand, one must not overlook, that because of the large difference in the melting point of both metals, the diffusivity of Al rich phases exceeds that of Ni rich ones by several orders of magnitude. From bulk data of the interdiffusion [132] the $NiAl_3$ phase, most rich in Al, is seen to have the highest growth rate at low temperatures. Hence, it is not astonishing that this phase appears first during thin film interreaction.

More recent studies have been devoted to the earliest reaction stages, where calorimetry indicated potential nucleation effects by two distinguished heat releases as discussed in section 2.4. Thus, attention is focused on eventual precursor reactions reducing the driving force before formation of the first equilibrium compound. Ma et al. [130] interpreted results of analytical electron microscopy as intermixing of both fcc materials on a depth of about 16 nm prior to formation of $NiAl_3$. By contrast, Barmak and coworkers demonstrated the formation
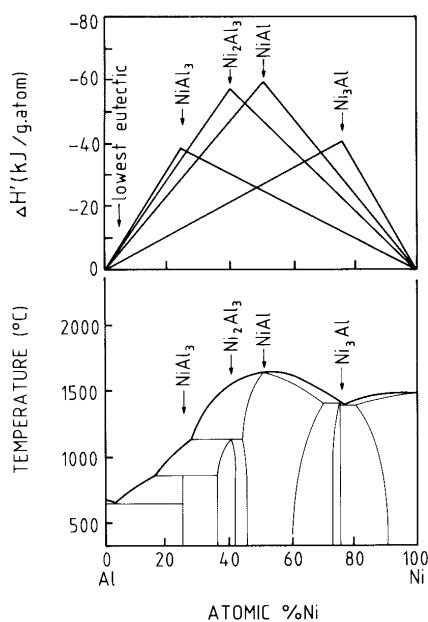

Figure 56: Phase diagram with equilibrium phases relevant for thin film interreaction and corresponding effective heat of formations according to Pretorius et al. [21]

of a B2 phase and an amorphous phase [133] already during deposition. Furthermore, they presented evidence by electron diffraction and calorimetry that a metastable phase of 63 at%Al develops during early annealing stages [41]. In electron diffraction patterns, it is indicated that this metastable phase has a B2 structure, although the determined composition deviates considerably from the stoichiometry of this ordered phase. Besides, Edelstein et al. [26] identified in XRD spectra of annealed ion beam sputtered multilayers, the metastable η phase (Ni_2Al_9) which was previously known only from rapid quenching of NiAl alloys. The appearance of the η was confirmed by Barmak et al. [133]. In summary, the experimental results seem to be contradictory, which leads K. Barmak to the suggestion that different deposition techniques might produce different reaction schemes, depending on the degree of initial interdiffusion or subtle microstructural differences.

6.1 Experiments

Atomprobe analysis is a suitable tool to investigate the influence of different deposition methods as even minor pre-reactions or impurities can be detected. To address such effects, Ni/Al interreaction couples have been prepared with two different deposition methods [42]. For the first kind of specimen, a 15 to 30 nm thick Al layer was deposited on single crystalline Ni tips by electron beam evaporation. This way, the specimen geometry of fig. 21a (page 34) is obtained. An electron micrograph of such a specimen is shown in fig. 57a. A smooth cap
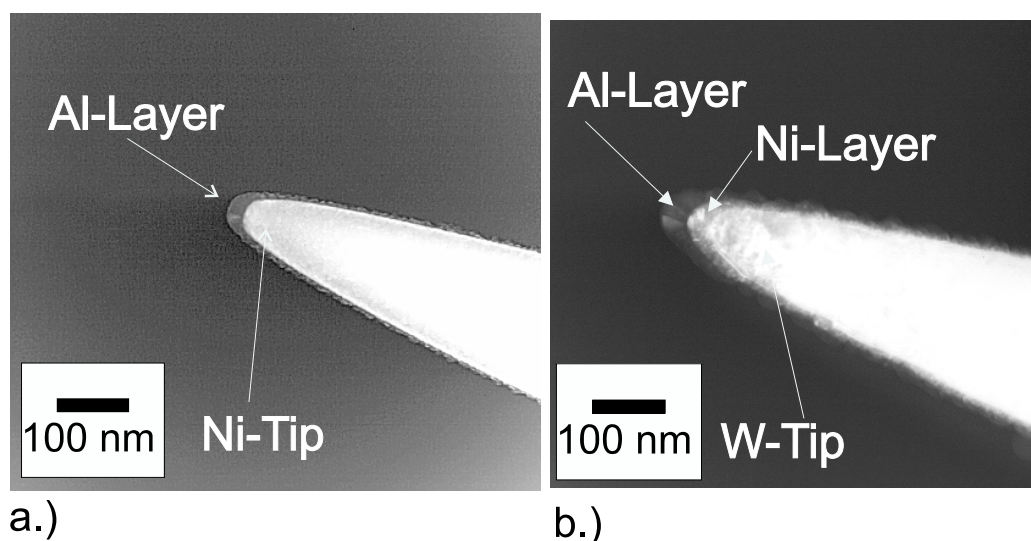

Figure 57: Electron micrographs of reaction couples in the as-deposited state: a) Al layer deposited on Ni tip by electron beam evaporation. b) sputter deposited Al/Ni bi-layer on W substrate
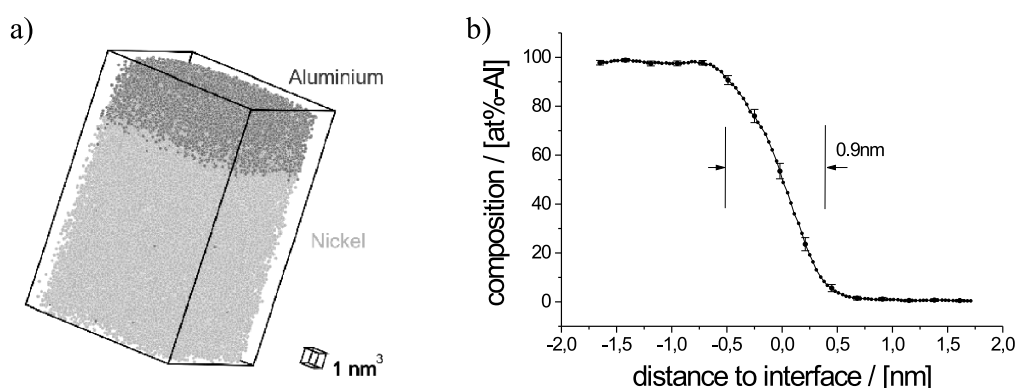
Figure 58: Atom distribution determined at the interface between Ni tip and Al layer deposited by electron beam evaporation (a) and composition profile determined normal to the interface (b). (Error bars indicate a 2σ significance level.)

layer is observed. Induced by the field-developed substrate surface and a low growth rate of $1\,\mathrm{nm/min}$, the microstructure of the Al layer gets comparatively coarse. Preferentially, one central grain grows at the tip apex, so that no grain boundary is found within or close to the analysed volume. For the second kind of specimen, bi-layers were sputter-deposited on tungsten substrate tips to achieve the geometry of fig. 21b. In this case, both layers are nano-crystalline with significantly smaller grain size of 10 to 20 nm diameter, as is seen in the electron micrograph reproduced in fig. 57b.

6.1.1 Coarse-grained layers

In figure 58, the reconstruction of the TAP data of a specimen with an Al cap-layer is shown in the as-prepared state (a) together with a composition profile determined normal to the prepared interface (b). The chemical transition at the freshly prepared interfaces appears on a depth of 0.9 nm (10%-90% criterion), although deposition was performed at 50 K. This degree of initial intermixing is comparable to that observed at Ag/Al specimens, so that one might argue that the mixing is just an artefact of the interface curvature. However, a geometrical estimate assuming a spherical substrate surface of 50 nm radius and a lateral width of the measurement of 10 nm, expects the variation of the interface position to only $\pm 1.5\,\text{Å}$, which is significantly smaller than the observed mixing depth. Indeed, the interface appears perfectly flat in the reconstructions, and composition profiles determined with reduced cross section at different lateral positions within the analyzed volume match closely at the interface, as discussed in [125]. Therefore, the observed intermixing must be interpreted as real; it is probably caused by the strong, attractive interaction between Ni and Al.

Specimens were annealed at various temperatures using an UHV furnace. According to experimental experience, the annealing time must not exceed one hour to preserve the required surface quality of the specimens. Hence, the annealing temperature has to be varied to access all reaction stages. In preliminary measurements using a conventional atomprobe [72], the equilibrium compounds were found at tip-shaped reaction couples in agreement to the established formation sequence [127]. Formation of Ni_2Al_3 was found after 5 min annealing at 350 °C, and of NiAl and Ni_3Al after 5 min annealing at 550 °C. The 3D-atomprobe improves the data statistics significantly by its increased measurement volume, and allows furthermore to relate composition variations to microstructural features because of its spatially resolved 3D analysis.

In fig. 59, a typical reconstruction obtained from tips which were annealed at low temperatures is shown. Up to an annealing temperature of 250 °C, always planar layer structures are seen without any evidence of grain boundary effects. Composition profiles determined normal to the reaction zone are presented in fig. 59 b)
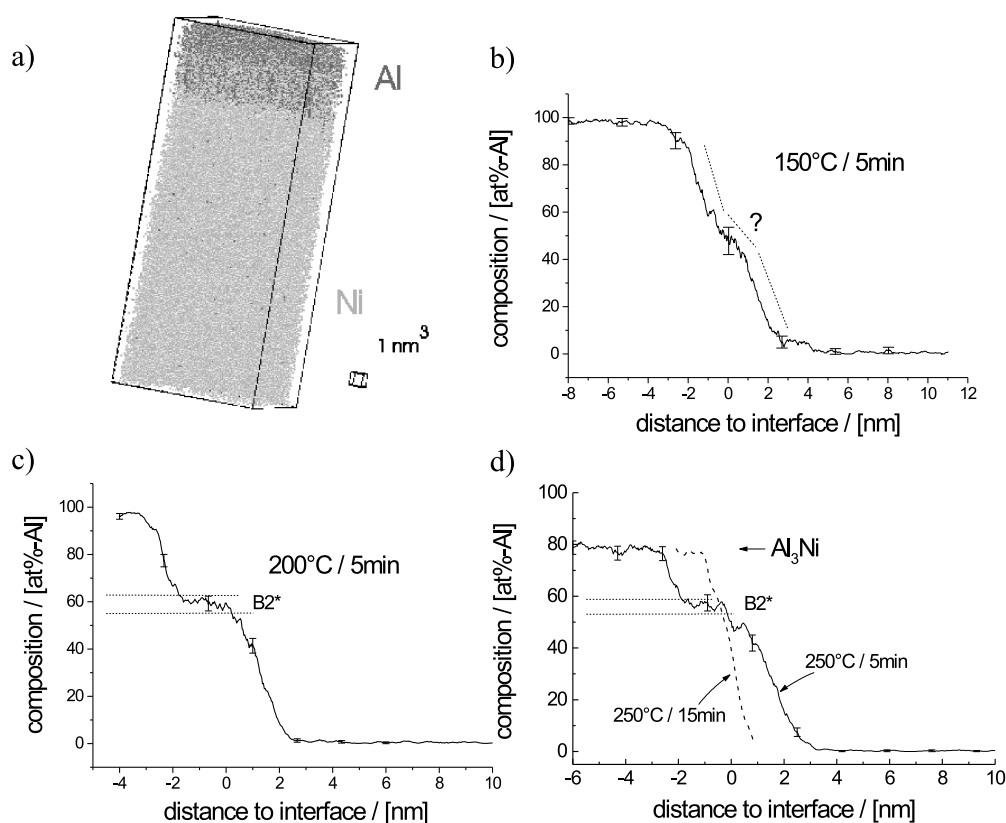

Figure 59: a) Atom distribution determined after 5 min heat treatment at 200 °C. Composition profiles taken normal to the initial interface after annealing 150 °C/5 min (b), 200 °C/5 min (c), 250 °C/ 5 & 15 min (d). (Error bars indicate the 2σ significance level.)

to d) as obtained after heat treatments 150 °C/5min, 200 °C/5min, 250 °C/5 min and 250 °C/15 min. When compared to the as-deposited state (fig. 58), a change in the profile is seen already after short-time annealing at 150 °C, which must be interpreted as significant in view of the results obtained in later stages. The slope of the profile decreases significantly in the composition range from about 35 at% to 67 at%-Al. From this, a composition plateau has developed in a slightly later state after 5 min annealing at 200 °C, indicating the formation of a distinct phase with an existence range spreading from 56 at% to 61 at%-Al in this early reaction stage. A similar plateau is observed for annealings up to 30 min at 200 °C. However, in spite of the significantly increased annealing time, the width of the plateau does not grow significantly. It is found in a maximum thickness of 3 nm.

After annealing at 250 °C for 5 min, a second phase of (77±2) at%-Al is noticed, which also forms as a planar layer along the initial interface. Subsequently, this phase grows while the other disappears, as is demonstrated by the profile after 15 min annealing at 250 °C, where only a minor shoulder reminds to the former phase. It is worth to point out that, opposed to the later disappearance of Al-rich equilibrium phases (see. eg. [72]), the shrinkage in this early stages is not due to the consumption of Al since the competing $NiAl_3$ phase is still growing. Thus, it is obvious that the phase which has formed first, is indeed an intermediate one, disappearing during further aging because of growth competition.

In order to follow subsequent reaction stages, temperature was increased to 400 °C. Remarkably, the planar layer structure is destroyed in these reaction stages, where the formation of Ni_2Al_3 is expected according to earlier measure-
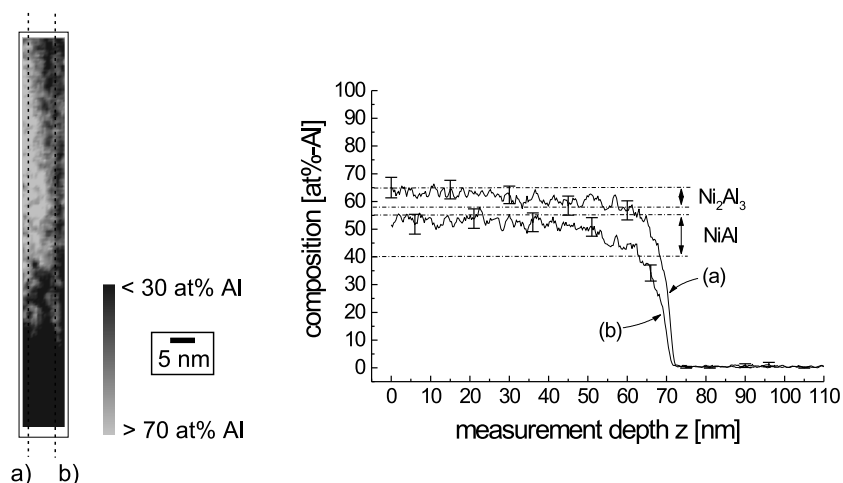

Figure 60: 2D composition map determined after 5 min annealing at 400 °C. Composition profiles shown at the right side are determined parallel to the tip axis at different lateral positions as indicated within the map (error bars indicate the 2σ significance level).

ments by conventional analytical field ion microscopy [72]. This is clarified by the exemplary composition maps shown in fig. 60. Chemical inhomogenities have developed in lateral direction in contrast to a layer geometry aligned parallel to the initial interface. According to the composition profiles determined at two different lateral positions, Ni_2Al_3 and NiAl meet at an interface aligned along the tip axis. Since in earlier stages a strictly planar reaction morphology is observed, it is suggested that the advanced reaction is accompanied by a recrystallization process which destroys the planarity. Similar as discussed at the interdiffusion of Cu/Au, this is very likely caused by considerable lattice mismatch between the products and the initial reaction partners. It is worth to note that the lattice mismatch of the reacting metals is quite comparable to that between Cu and Au, where the recrystallization is initialized as soon as the mixing amplitude exceeds about 20 at%. By analogy, probably the formation of higher alloyed compounds is accompanied by a recrystallization to relax induced stress in the case of Ni/Al, too.

6.1.2 Nano-crystalline layers

Similar to the profile shown in fig. 58b, sputter-deposited layers show also a solution zone of about 1 to 2 nm width in the as-prepared state [125]. This finding is in agreement with the conclusion of Edelstein et al. based on small angle scattering spectra [26]. Remarkably, in contrast to the measurements of specimens made by electron beam evaporation, no intermediate phase with 60 at%-Al is observed after annealing the specimens at 200 °C. Instead, the TAP data reveal a diffusion of Ni into Al along certain pathways, which are assumed to be grain boundaries of the deposited Al layer. In the 2D composition map, shown in fig. 61,
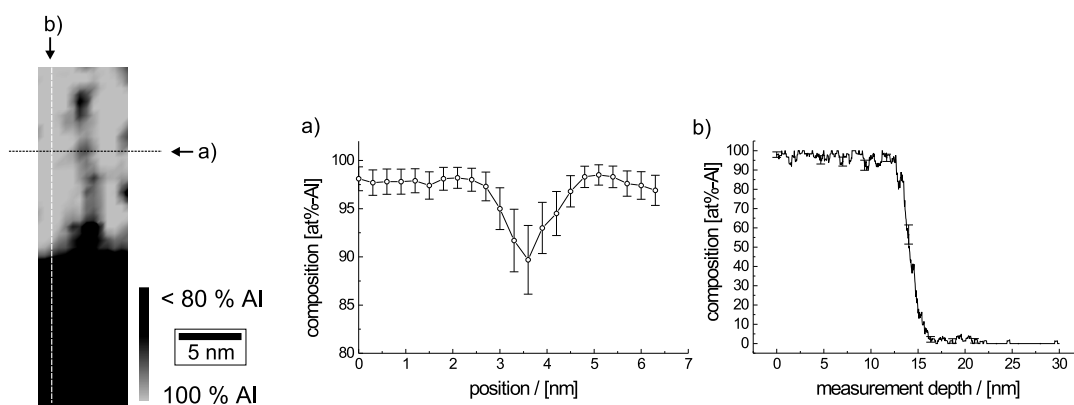

Figure 61: Composition map measured at a sputtered Ni/Al bi-layer after 5 min annealing at 200 °C. Corresponding composition profiles were determined at the indicated positions (error bars indicate the 2σ significance level).

the diffusion path along the grain boundaries is obvious. The arrangement of the Ni rich paths observed in several specimens suggests a grain diameter of 5 to 10 nm [125], in agreement with electron micrographs of the tips (fig. 57). The corresponding composition profile across the grain boundary (a) reveals a Ni content of already 10 at% in the boundary. At the original interface aside the grain boundary, a smooth chemical transition is found without any pronounced composition plateau at about 60 at%-Al (b), opposed to the reaction in the coarse grained layers at the same aging state.

In specimens annealed at 250 °C, the equilibrium phase $NiAl_3$ is observed for the first time. Fig. 62 shows a reconstruction of the atom distribution as well as two composition profiles taken through different parts of the analysed volume. It is clearly seen, that inside the Al layer the composition is not homogeneous in lateral direction. Instead, a $NiAl_3$ particle is seen laterally adjacent to Al terminating phase, which allows the conclusion that the equilibrium phase nucleates at grain boundaries and subsequently grows in lateral direction. Obviously, the interreaction does not develop on a planar layer structure in nano-crystalline specimens, even in this very early reaction stages. Beside the formation of the Al rich equilibrium phase at the grain boundary, now narrow composition plateaus at the former interface at 50 at% indicate the beginning formation of the equilibrium NiAl phase. This is confirmed in a later stage after annealing at 300 °C (see composition profile in fig. 63), where both equilbrium phases are seen very clearly, considerably grown in thickness compared to the previous state.
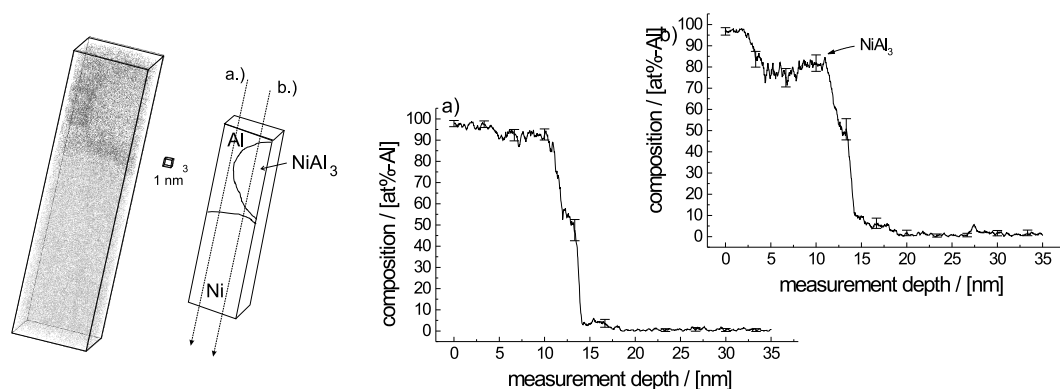

Figure 62: Volume reconstruction of a sputtered bilayer after 5 min annealing at 250 °C. Composition profiles shown at the right are determined at different lateral positions as indicated in the sketch (error bars indicate the 2σ significance level).
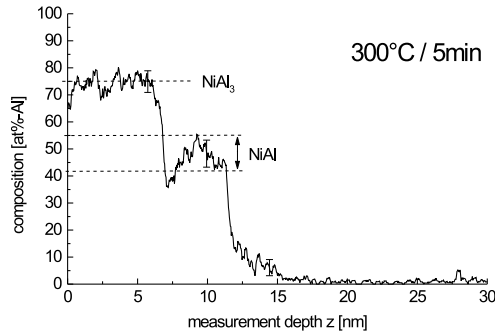
Figure 63: Composition profile through a sputtered bilayer after 5 min annealing at 300 °C (error bars corresponds to a 2σ significance level).

6.2 Discussion

Similar to the already presented case of Ag/Al, the nanoanalysis of the interreaction of Ni/Al is able to reveal detailed information on the atomic transport accompanying the reaction. Most remarkably, again an intermediate phase is identified which forms as a first reaction product. This phase forms very quickly at the beginning but stops growing at a maximum thickness of 3 nm. Furthermore the measurements prove, that the initial microstructure not only controls the spatial arrangement of the products but also the phase formation sequence in general: In planar layers with only a few nucleation sites and slow transport an intermediate phase with 60 at%-Al is formed prior to $NiAl_3$, while in nanocrystalline layers the latter is formed directly. In the following, this aspects shall be considered in further detail.

On the other hand, the lack of direct structural information turns out to be an important disadvantage when the observed preferred compositions should be related to known phases. Thus, the nature of the observed phases must be considered regarding known data of complementary methods.

6.2.1 Identification of observed phases

As presented above, phases of two different compositions are seen as first formed phases depending on the specimen's microstructure. The composition of 77±2 at%Al has been tacitly interpreted as the orthorombic equilibrium phase $NiAl_3$, although the measured Al concentration is always slightly higher than the expected stoichiometry. In literature also the formation of the metastable η-phase has been reported in early reaction stages of sputter-deposited specimens. This phase has a stoichiometry of Ni_2Al_9, which is not that far from the measured composition. Furthermore, atomprobe analysis is more likely to loose Al atoms from the counting statistics because of the lower evaporation field strength of Al. In view of this situation, it cannot be decided finally which of both phases is detected in the atomprobe measurements. However, as the majority of published

studies report the equilibrium phase, especially in layers deposited by electron beam evaporation, I tend to identify the observed composition close to the required stoichiometry with the equilibrium $NiAl_3$ phase.

The second distinguished composition at about 60 at% Al matches the existence range of the Ni_2Al_3 phase. However, this equilibrium phase is noticed in the formation sequence only later, and therefore in atomprobe measurements only after annealing at higher temperatures (350 °C[72]). Hence, it is not very likely that the intermediate product observed in very early stages is already this equilibrium phase. Remarkably, Michaelsen et al. identified a 'metastable' reaction product with 63 at%-Al by a clever interpretation of calorimetry data for multilayer specimens of varying average composition [41]. The atomprobe results confirm this interpretation as they prove the existence of such a phase by direct chemical analysis and demonstrate that it is formed as a smooth layer-like product. Michaelsen showed that in related electron diffraction patterns, all the observed reflections are consistent with the B2 structure and proposed therefore that the observed intermediate phase is a non-equilibrium Al rich B2 phase. Unfortunately, the intensity of the decisive reflections is very week and might be interpreted ambiguously. With X-ray diffraction direct evidence for the early formation of a B2 structure has been reported also for multilayers of 50 at% Al average composition and 10 nm periodicity [26], where the phase might be dictated by the consumption of the components. In the following the non-equilibrium phase ('B2*') will be considered as a reasonable hypothesis, although additional investigations by HREM are highly recommended to finally clarify the structure of this phase.

At first sight, the early intermediate formation of a B2 phase is very surprising as this phase is seen in bulk interdiffusion experiments [132] only at high temperatures because of its low mobility. However Michaelsen pointed out, that the mobility of the B2 structure is known to increase significantly if its composition deviates from stoichiometry [134].

Beside the proven deviation in composition, a careful evaluation of reported diffractometry indicates, that the intermediate product deviates from its equilibrium also in terms of its long range order. In table 4, observed reflections are allocated, as determined by X-ray [26] and electron diffraction [41] at multilayers of 10 nm periodicity and of 50 at% and 75 at% Al average composition, respectively. Obviously, the superlattice reflections fail completely to appear in X-ray diffraction, and in electron diffraction patterns they are only very weak, although the scattering contrast between Ni and Al is sufficient to yield appreciable intensities [135]. Because of the strong interaction between Al and Ni, long range order is very stable in NiAl, which is reflected by a persistent order structure up to the melting point. Thus, at the applied reaction temperatures, the equilibrium degree of order should be very close to one in contrast to the observed intensity of the superlattice reflections.

reflection	spacing /[nm]	type	XRD	ED	potential misinterpretation
100	0.289	S.L.		(x)	
110	0.204	fundamental	X	X	Al_{200}
111	0.167	S.L.		(x)	
200	0.144	fundamental		X	Al_{220}
210	0.129	S.L.		(x)	Ni_{220}
211	0.118	fundamental	X	X	Al_{222}
220	0.102	fundamental	X		Ni_{222}

Table 4: Expected reflections for the B2 NiAl phase. Reflections that are found in significant amounts by X-ray diffraction [26] and electron diffraction [37] are marked by 'X', those with only weak intensity so that they are hardly seen in the published figure by '(x)'. Especially in electron diffraction the resolution of reflections is notoriously bad, so that misinterpretation might occur. Reflections of Al or Ni with almost identical spacing are indicated in the last column. If potential intermixing of Ni and Al is taken into account the situation gets even worse.

By these considerations a remarkable parallelism between the already discussed reaction of Ag/Al and the present one of Ni/Al becomes obvious. In both cases, we find strong evidence that a phase known from the phase diagram is stabilized in an off-equilibrium condition. This way, a general mechanism of the early interreaction might become visible.

6.2.2 Early composition profiles in the case of planar geometry

Owing to its outstanding depth resolution the atomprobe analysis allows to prove several proposed concepts on the development of the first reaction product. For that, the composition profiles shown in fig. 59, determined at a planar reaction morphology shall be discussed in more detail.

Ma et al.[130] determined composition profiles at the Ni/Al interface by EDX analysis with a spatial resolution of about 4 nm. They claimed to have observed the development of a continuous intermixing on a depth of about 16 nm without formation of a distinct product phase and proposed that this intermixing will reduce the thermodynamic driving force so that appreciable nucleation barriers to the formation of $NiAl_3$ result. In view of the present data of atomprobe tomography, the formation of a solid solution on such an advanced depth must be interpreted as an artefact of the limited resolution of their analytical technique. The profiles in fig. 59 show clearly that the first product phase, non-equilibrium B2*, develops from the very beginning, fixing an upper limit of the depth of mere interdiffusion to about 1 to 2 nm. To a major part, this intermixing is already present after deposition, independent from the actual deposition technique. In

consequence, it is the intermediate B2* phase that causes a sufficient reduction of the driving force rather than the formation of a fcc solution, as was already suggested by Michaelsen et al. [41].

The formation sequence of the equilibrium products follows the prediction of the *effective heat of formation rule* proposed by Pretorius [131, 127], so that it is very tempting to test the basic assumption underlying the physical explanation of this empirical rule. Pretorius argues that at the very beginning a solution zone with the composition of the lowest eutectic develops at the interface. However, in the Ni/Al system this eutectic is found at about 3 at%-Ni. In none of the composition profiles measured by atomprobe tomography, a pronounced plateau or at least reduced slope in the composition profile is seen at that composition. Even if the observed intermediate phase is interpreted in this sense, its composition is way of the eutectic, which makes the established justification of the empirical rule very questionable.

The concept of a critical composition gradient required to allow nucleation of the product phase was introduced by Gusak [44] and Desré and Yavari [43] to describe the suppression of equilibrium phases in early reaction stages. Early calculations predicted critical interdiffusion widths of several tens of nm before nucleation of the product becomes possible. Losing some of the constraints imposed to the nucleus, the critical gradient was later recalculated to about $2 \cdot 10^9$/m for the formation of $NiAl_3$ [136]. The presented atomprobe measurements agree with this prediction as they fix a lower limit of the critical gradient at $0.5 \cdot 10^9$/m. On the other hand, one has to ask whether the concept will help to explain the phase formation sequence, when the criterion is already fulfilled by the initial intermixing stemming from layer deposition.

6.2.3 Microstructural control of formation sequence

The finding that the phase formation sequence at the prepared Ni/Al interface depends on the microstructure of the deposited layers is certainly very attractive and in the context of this report most important. Although in both investigated layer structures pure Ni and Al meet at the prepared interface, the formation of an intermediate phase (B2*) before nucleation of the $NiAl_3$ phase is only observed in quasi single-crystalline layers, while in nano-crystalline specimens the intermediate phase fails to appear at comparable aging stages. Instead the Al-rich equilibrium phase is directly nucleated at grain boundaries of the Al layer.

Microstructural effects on the phase formation sequence have been stated and discussed several times in the past [129, 26], and partly explained by different impurity levels obtained with different deposition techniques. However, as the TOF analysis is equally sensitive to all atomic species, the impurity hypothesis can be directly tested by the atomprobe spectra. In none of the described mea-

surements impurities are observed in significant amounts. Hence, it is concluded that the observed effect is directly due to the variation of the microstructure and the different transport paths resulting therefrom.

The heterogeneous nucleation of the NiAl$_3$ phase at grain boundaries of the nanocrystalline layers is understood from the complicated orthorombic structure of this phase with 20 atoms per unit cell, which lets us expect considerable interfacial energies in contact to the fcc metals. Furthermore, one has to be aware that the energy of the initial Ni/Al interface is presumably very low, so that this interface may be ruled out as an efficient nucleation site. This is seen by the following very simple consideration using a mean field ansatz. Determining the pair exchange energy $\epsilon = \epsilon_{NiAl} - (\epsilon_{NiNi} + \epsilon_{AlAl})/2$ from the stability of the B2 order, for which T$_c$ may be approximated by the melting point $T_m = 1911\,K$, we have

$$\epsilon = \frac{zkT}{2} = -2.6 \cdot 10^{-20}\,\mathrm{J/atom}\,, \tag{56}$$

where z denotes the number of nearest neighbors. From that, the chemical contribution to the energy of a sharp interface is estimated to (see e.g. [137])

$$\sigma_{\mathrm{chem}} = \frac{12}{a_0^2}\epsilon = -5.3\,\mathrm{J/m}^2\,, \tag{57}$$

where the number of neighbor bounds across a (111) interface between the fcc metals was taken into account. This value exceeds considerably the structural contribution, which may be estimated from typical energies of homo-phase grain boundaries ($\approx 0.5\,\mathrm{to}\,2\,\mathrm{J/m}^2$). Hence, the total energy of the initial interface might become even negative, which clarifies that almost no reduction of an eventual nucleation barrier can be expected from the initial interface and explains furthermore, why the preparation of a chemically sharp interface is almost impossible in this reaction couple from a thermodynamic point of view.

By that, it becomes clear that the presence of high energetic homo phase grain boundaries opens an additional reaction path by fast nucleation of NiAl$_3$. But why does this hinder the formation of the intermediate B2* phase at the remaining part of the interface between the grain boundaries?

This behaviour is only understood, if a thin reaction layer at the inter-phase boundary (P.B.) is postulated, as sketched in the upper part of fig. 64. Because of the disturbed lattice symmetry at the interface, a higher mobility is expected in this layer similar as in grain boundaries, which allows efficient intermixing of both species. The nucleation of any compound requires a sufficient chemical potential of Ni in the reaction layer. Thus, any phase formation will be essentially controlled by the Ni concentration which itself is determined by the balance of the fluxes into and out of the phase boundary as sketched in the lower part of fig. 64. In the grain boundary free case (a), the barriers of the flux from the Ni crystal might be comparable to that of the out flow into the Al layer. Hence,
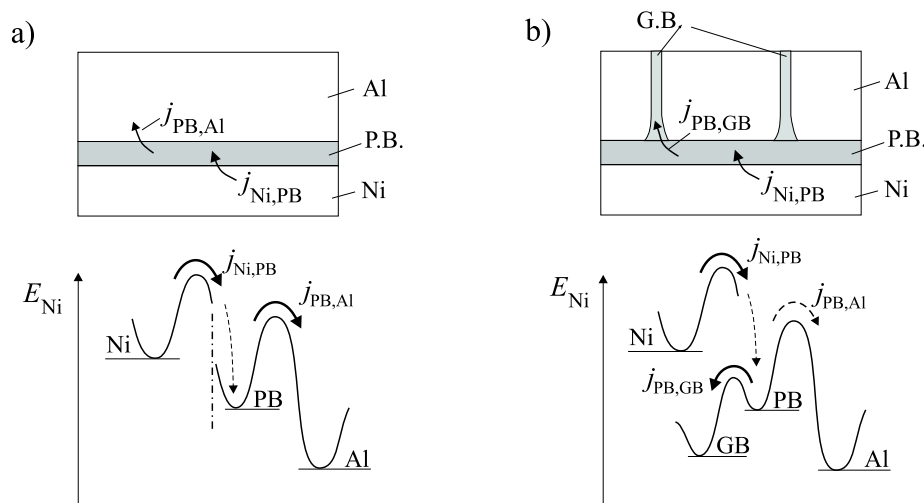
Figure 64: Scheme to explain the microstructural influence on the initial phase sequence. a) planar layer reaction: high chemical potential of Ni inside the phase boundary allows nucleation of intermediate B2 phase, b) nanocrystalline Al: potential of Ni inside the phase boundary reduced because of loss into grain boundaries.

considerable Ni concentrations are achieved in the reaction layer, which allows the formation of the Ni rich B2*. By contrast, a second reaction path is introduced in the nano-crystalline case (b), distinguished by low grain boundary transport barriers, which allow the fast Ni transport into the grain boundary sinks. If the supply into the reaction zone is not modified between both cases, which has to be expected as volume diffusion as well as grain boundary diffusion is frozen inside the Ni layer, the Ni concentration gets significantly reduced. The nucleation of the interfacial B2* phase is no longer possible.

6.3   Kinetic stabilization of non-equilibrium B2 phase

Certainly, the early formation of a non-equilibrium B2 phase is the most astonishing feature of the interreaction in Ni/Al. Because of its low mobility, this phase is seen by conventional RBS analysis only in late reaction stages, while the high resolution TAP analysis proves that it is formed very early, but vanishes subsequently in growth competition. The early nucleation of the phase might be understood from the, compared to the other compounds, most simple superlattice structure. However, the apparent stop in growth and the stabilization of an off-stoichiometric composition deserves further consideration. It is quite obvious that these effects cannot be understood by layer growth models relying on equilibrium properties of the phase. The very simple structure of B2 ordered compounds suggests to compare the experimental behaviour with the statistical prediction of Monte-Carlo simulations. This way, the phase properties are

not assumed a priori, but are established by the microscopic model during the simulated reaction.

6.3.1 Monte-Carlo simulation

The model calculations presented in the following are aimed to detect potential mechanisms rather than describing the reaction of Ni and Al quantitatively. Thus, the most simple ansatz of pair-wise interactions between next neighbors is sufficient. Only two free parameters are required to determine the equilibrium properties and the reaction kinetics, which are defined in the usual manner as exchange and asymmetry parameters

$$\epsilon = \epsilon_{Ni,Al} - (\epsilon_{Al,Al} + \epsilon_{Ni,Ni})/2\,; \qquad \epsilon_{as} = (\epsilon_{Al,Al} - \epsilon_{Ni,Ni})/2\,. \tag{58}$$

The first parameter defines the critical temperature of ordering while the latter takes into account the different strength of Al-Al and Ni-Ni bounds expected from the very different cohesion energy of both metals. The atoms are distributed on a rigid bcc host lattice. For the sake of computational efficiency, the primitive basis of the bcc lattice is chosen as co-ordinate system. The geometry of the simulated cell is sketched in fig. 65. (002) planes of the bcc structure with 32×32 or 64×64 atoms are stacked along the [111] direction. In two dimensions, periodic boundary conditions are applied to describe a bi-layer of infinite lateral size. In the remaining dimension, at one side a pure bcc Al and at the other a pure bcc Ni layer is maintained at the boundaries. Compared to the experiment, where the supply of material is always limited and of course both terminating phases have a fcc structure, this latter condition seems to be somewhat artificial. However, it allows to establish a real steady state of the atomic flux and to study its influence
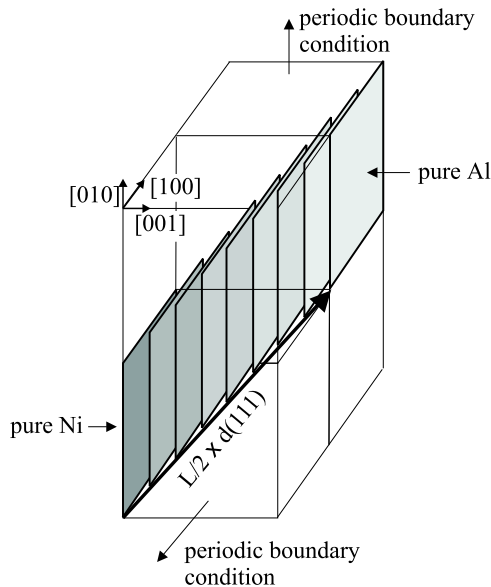

Figure 65: Geometry of the simulated volume. (002) planes are stacked along the [111] direction. Periodic boundary conditions are applied in the [100] and [010] direction. In the [001] direction pure Ni and pure Al is maintained at the boundaries.

on composition and long range order of the B2 phase. The average composition gradient established in the simulated volume is defined by the box length L, the number of (002) planes contained in the volume.

In the case of equilibrium phenomena, different atomic jump mechanisms may be constructed for computational reasons, which yield identical results as long as the principle of detailed balance is obeyed. By contrast, for the study of kinetic phenomena, these different microscopic models are by no means equivalent. Therefore, two different mechanisms were used for comparison to determine the migration of the atoms. In the first one (*'atom exchange'*), a next neighbor pair is chosen randomly in each Monte Carlo step. If the exchange of both atoms releases configurational energy ($\triangle E < 0$), the exchange is performed. If it requires an expense of energy, the atoms are exchanged with the probability

$$p \propto \exp\left(-\frac{\triangle E}{kT}\right) \tag{59}$$

(Metropolis algorithm [138]). For the second mechanism (*'vacancy jump'*), a vacancy is introduced into the system. The random walk of the vacancy is simulated by selecting in each step the jumping direction from the 8 possibilities according to the probability

$$p \propto \exp\left(-\frac{\triangle E}{2kT}\right) . \tag{60}$$

To calculate the change of the configurational energy related to a jump, vacancy-atom bonds are set to zero. Explicit formulas are presented in [135] for the analogous case of an fcc lattice. Obviously, both mechanisms fulfill the principle of detailed balance and indeed the LRO parameters obtained with both mechanisms in thermal equilibrium agree perfectly. The asymmetry parameter ϵ_{as} is effective in the vacancy jump model. Hence, with this model an asymmetry in the composition dependence of the diffusion coefficient may be described.

6.3.2   Steady state in the limit of thin layers

Using the described algorithms, the development of an Al/Ni bi-layer is simulated for various box lengths L, until the steady state is reached. For example, steady state composition profiles obtained with the vacancy exchange mechanism at a temperature $T = T_c/2$ are shown in fig. 66. If the interdiffusion coefficient were independent of the composition, a simple linear concentration variation along the box length would be expected. However, the simulated profiles develop quite differently. At the center of the simulated volume the slope of the composition curve appears to be significantly increased. This result is easily understood if the LRO is calculated at different depth positions. The order profile shown in the
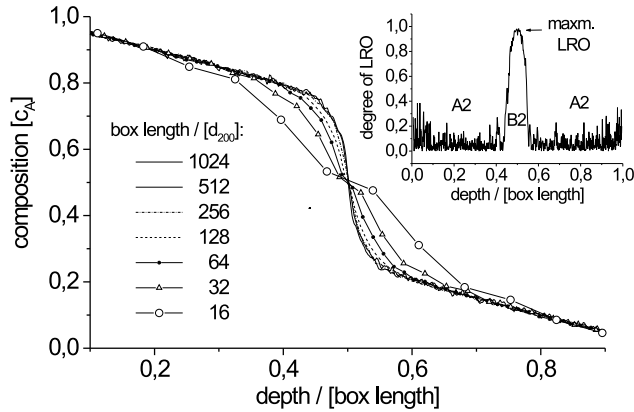
Figure 66: Composition profiles in the steady state of the M.C. simulation. Results for different lengths of the simulated volume are plotted versus the normalized depth position. The inset shows the spatial variation of the LRO parameter for a box length of 1024 lattice planes. ($\epsilon = -0.05\,\mathrm{eV}$, $\epsilon_{as} = 0$, $T = 1000\,\mathrm{K}$)

inset was determined using the definition

$$
q := \begin{cases} (c_1 - c_2)/(c_1 + c_2) & ;\text{if } c_1 + c_2 < 1 \\ (c_1 - c_2)/(2 - (c_1 + c_2)) & ;\text{else} \end{cases} \tag{61}
$$

for the long range order parameter, where c_1 and c_2 denote the composition of the two sublattices and $c_1 > c_2$ is assumed. This definition generalizes the usual order parameter defined at ideal stoichiometry to off-stoichiometric compositions. In the central region within the composition range from about 25 to 75 at% the B2 order is established. As this superstructure consists of two isolated superlattices, diffusion is hindered by the long range order. Thus, in order to keep the current constant throughout the simulated volume as required for the steady state, the composition gradient is increased in the ordered region to compensate for the reduced mobility.

As long as the equilibrium properties of the homogeneous system are obtained along the composition profile, the ratio of the mobilities of the ordered and disordered structure is fixed. Thus, if the box length is decreased but at the same time the x-axis re-scaled by the inverse factor, one would expect the steady state profiles to meet at a common master curve. The correct scaling is indeed observed for box lengths larger than about 256 lattice planes as seen in fig. 66. However, if the box size gets smaller, the composition profiles no longer agree with the master curve. Instead, the linear composition variation expected for a constant diffusion coefficient is approached gradually and furthermore the thickness of the ordered layer increases relative to the box length. This indicates that with decreasing length, which means increasing atomic current and increasing average composition gradient, the ordered phase is changed in a way that the transport mobility increases. In other words, the phase corresponds no longer to its equilibrium configuration. This is seen more clearly, if the maximum degree of LRO established in the center of the B2 layer is plotted versus the inverse of the
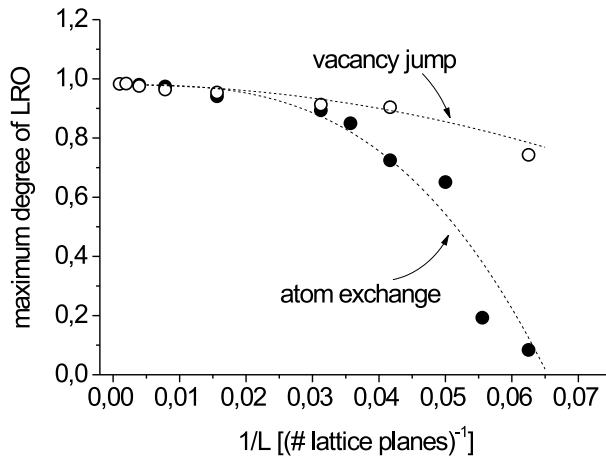
Figure 67: Maximum order established in the B2 phase in dependence on the length of the simulation volume. The reduction of LRO with decreasing length depends on the applied kinetic model. ($\epsilon = -0.05\,\text{eV}$, $\epsilon_{as} = 0$, $T = 1000\,\text{K}$)

box length, as it is done in fig. 67 for both jump mechanisms. Order decreases significantly with the box length. With the atom exchange model, it gets almost completely suppressed as soon as the box length falls below 20 lattice planes.

The described deviations from equilibrium are noticeable, as soon as the length of the simulated volume becomes smaller than 128 lattice planes. In this case the ordered region comprises fourteen (200) lattice planes corresponding to a thickness of about 2 nm. This is exactly the thickness range that was determined for the B2* phase by atomprobe tomography. Hence, it is suggested that the suppression of long range order predicted by the simulation plays indeed an important role during the early interreaction stages. At first, the reduced order allows the quick formation and initial growth of this phase. But subsequently, when order is increasingly established, the mobility decreases and in consequence the phase stops growing as indicated in the analysis. In addition the initial suppression of long range order is indicated by the weak intensity of superlattice reflections in X-ray or electron diffractometry.

6.3.3 Influence of composition-dependent mobility

The initial B2* phase is found to form in an off-equilibrium, Al rich composition. It was suggested, that the stabilization of this composition is due to the increased mobility of Al rich compositions. The kinetic Monte-Carlo simulation using the vacancy jump mechanism allows to test this concept. If the asymmetry parameter is estimated from the difference in cohesion energy of Ni and Al, $\epsilon_{as} \approx 0.1\,\text{eV}$ is found ($E_{coh}^{Al} = -0.56\,\text{eV/bond}$; $E_{coh}^{Ni} = -0.74\,\text{eV/bond}$ [139]). Introducing this parameter into the simulation, the vacancy is found predominantly inside Al rich regions. In consequence, the mobility is significantly increased in Al rich regions. Calculating the composition and LRO profiles in
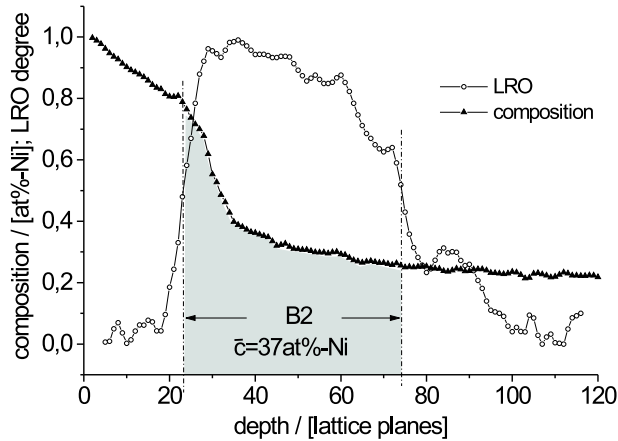
Figure 68: Composition and LRO order profiles obtained in the steady state of the M.C. simulation. ($\epsilon = -0.05\,\text{eV}$, $\epsilon_{as} = 0.1\,\text{eV}$, $T = 1000\,\text{K}$).

the steady state, a pronounced asymmetry in the concentration profile is found as shown in fig. 68. If the B2 phase region is defined by the half value width of the order profile, the average composition inside the phase is found considerably depleted in Ni, in agreement with the experimentally determined compositions. The atomprobe analysis revealed significant deviations in the composition of equilibrium phases in the case of Ni/Al and of Ag/Al as well. The concept to explain these deviations by a composition dependent mobility seems to be a quite reasonable one.

6.4   Conclusions

The early stages of the interreaction of Ni/Al thin films have been studied by atomprobe tomography. To determine the potential influence of the microstructure, the reaction of a coarse grained layer structure prepared by electron beam evaporation has been compared to that of sputtered nano-crystalline layers. It is found that beside the spatial arrangement of the product phases also the phase formation sequence itself is changed by the internal microstructure of the reacting materials.

- In quasi single crystalline layers with low density of grain boundaries the early reaction proceeds on a clearly defined layer structure. As a first product, a layer of an intermediate phase of 56 to 61 at% Al is determined. Regarding published diffractometry, this phase might be interpreted as B2 NiAl, with a composition and degree of LRO significantly deviating from its equilibrium. This intermediate layer does not grow parabolically. It is observed with a maximum thickness of 3 nm. Subsequently it disappears in competition with a layer of NiAl$_3$. In later stages the layer structure is destroyed and a reaction induced recrystallization is indicated. The further

formation sequence of the equilibrium phases follows strictly in the order from Al rich to Ni rich phases in agreement to previous work.

- By Monte-Carlo simulations of the phase stability, it is suggested that the long range order of the phase gets decreased in the case of high atomic currents or steep composition gradients. The composition deviation of the non-equilibrium B2 phase is explained by the increased mobility of Al rich ordered solutions.

- In nano-crystalline layers with a high density of grain boundaries, the early formation of an intermediate B2 phase is skipped. Instead Al grain boundaries are wetted by Ni and the equilibrium $NiAl_3$ compound is directly nucleated at these grain boundaries. Instead of clearly defined product layers, a complicated 3D reaction morphology evolves.

- To explain the microstructural control on the phase formation sequence, it is anticipated that the effective Ni concentration in the interphase boundary is significantly reduced by fast flux into grain boundary sinks in the case of the nano-crystalline sample structure.

Acknowledgement

References

[1] Semiconductor Industry Association, *'International Technology Roadmap for Semiconductors'* 1999,
http://public.itrs.net/files/1999_SIA_Roadmap/Home.htm.

[2] A. D. Smigelskas, E. O. Kirkendall, *Trans AIME* 171 (1947) 130.

[3] G. Reiss, H. Brückl, A. Hütten, Phys. Bl. 54 (1998) 339.

[4] W. J. Johnson, *Progr. Mater. Sci.* 30 (1986) 81.

[5] K. Holloway and R. Sinclair, *J. Appl. Phys.* 61 (1987) 1399.

[6] K. Samwer, *Phys. Reports* 161 (1988) 1.

[7] R. Sinclair, T. Yamashita, M. A. Parker, K. B. Kim, K. Holloway and A. F. Schwartzman, *Acta Cryst.* 44 (1988), 965.

[8] H. Sieber, P. Werner, D. Hesse, *Phil. Mag. A* 75 (1997) 21.

[9] J. M. Howe, *Mater. Trans. JIM* 39 (1998) 3.

[10] J. S. Kirkaldy, *Can. J. Phys.* 36 (1958) 917.

[11] G. V. Kidson, *J. Nucl. Mat.* 3 (1961) 21.

[12] B. E. Deal, A. S. Grove *J. Appl. Phys.* 36 (1965) 3770.

[13] J. M. Poate, K. N. Tu, J. W. Mayer, *Thin Films - Interdiffusion and Reactions* New York 1978.

[14] U. Gösele and K. N. Tu, J. Appl. Phys. 53 (1982) 3252.

[15] F. M. d'Heurle, P. Gas, and J. Philibert, *Def. Diff. Forum* 143-147 (1997) 529.

[16] R. Bormann, *Mat. Res. Soc. Symp. Proc.* 343 (1994) 169.

[17] U. Gösele, K. N. Tu, *J. Appl. Phys.* 66 (1989) 2619.

[18] W. J. Meng, C. W. Nieh, W. L. Johnson, *Appl. Phys. Lett.* 51, (1987) 1693.

[19] R. Bené, *J. Appl. Phys.* 61 (1987) 1826.

[20] R. M. Walser, R. W. Bené, *Appl. Phys. Lett.* 28 (1976) 624.

[21] R. Pretorius, *Vacuum* 4-6 (1990) 1038.

[22] R. Pretorius, A. M. Vredenberg, F. W. Saris, R. de Reus, *J. Appl. Phys.* 70 (1991) 3636.

[23] A. R. Miedema, P. F. de Chatel, F. R. De Boer, *Physica B* 100 (1980) 1.

[24] S. U. Campisano, G. Foti, E. Rimini, S. S. Lau, J. W. Mayer, *Philos. Mag.* 31 (1975) 903.

[25] G. Majni, C. Nobili, G. Ottaviani, M. Costato, and E. Galli, *J. Appl. Phys.* 52 (1981) 4047.

[26] A. S. Edelstein, R. K. Everett, G. Y. Richardson, S. B. Quadri, E. I. Altman, J. C. Foley, J. H. Perepezko, *J. appl. Phys.* 76 (1994) 7850.

[27] S. Meng et al., *Mat. Sci. Eng.* 97 (1988) 87.

[28] S. B. Newcomb and K. N. Tu, *Apl. Phys. Lett.* 48 (1986) 1436.

[29] J. E. E. Baglin, J. M. Poate in J. M. Poate, K. N. Tu and J. W. Mayer, *Thin Films — Interdiffusion and Reactions*, New York 1978 p. 312.

[30] Y. L. Corcoran, A. H. King, N. de Lanerolle, B. Kim, *J. Electr. Mat.* 19 (1990) 1177.

[31] V. M. Kosevich, A. N. Gladkikh, M. V. Karpowsky, V. N. Klimenko *Interf. Sci.* 2 (1994) 247, 261, 271.

[32] V. M. Kosevich, V. N. Klimenko, A. N. Gladkikh, M. V. Karposwky *Interf. Sci.* 3 (1995) 151.

[33] W. D. Buckley and S. C. Moss, *Solid-State Electronics* 15 (1972) 1331.

[34] K. N. Tu, W. K. Chu and J. W. Mayer, *Thin Solid Films* 25 (1975) 403.

[35] F. M. d'Heurle, *J. Mater. Res.* 3 (1988) 167.

[36] K. R. Coffey, L. A. Clevenger, K. Barmak, D. A. Rudman, and C. V. Thompson, *Appl. Phys. Lett.* 55 (1989) 852.

[37] C. Michaelsen, K. Barmak, T. P. Weihs, *J. Phys. D* 30 (1997) 3167.

[38] R. Roy, S. K. Sen, *J. Mat. Sci.* 27 (1992) 6098.

[39] K. Barmak, C. Michaelsen, J. Rickman, M. Dahms, *Mat. Res. Soc. Symp. Proc.* 403 (1996) 51.

[40] E. Ma and C. V. Thompson, L. A. Clevenger, *J. Appl. Phys.* 69 (1991) 2211.

[41] C. Michaelsen, G. Lucadamo, K. Barmak, *J. Appl. Phys.* 80 (1996) 6689.

[42] T. Jeske and G. Schmitz, *Mat. Sci. Eng.* (in press).

[43] P. J. Desré and R. Yavari, *Phys. Rev. Lett.* 64 (1990) 1533.

[44] A. M. Gusak, *Ukr. Phys. J.* 35 (1990) 725.

[45] F. Hodaj, A. M. Gusak, and P. J. Desré, Phil. Mag. A 77 (1998) 1471.

[46] S. J. Pennycook, D. E. Jesson, *Phys. Rev. Lett.* 64 (1990) 938.

[47] A. Cerezo, T. J. Godfrey and G. D. W. Smith, *Rev. Sci. Instrum.* 59 (1988) 862.

[48] D. Blavette, B. Deconihout, A. Bostel, J. M. Sarrau, M Bouet and A. Menand, *Rev. Sci. Instrm.* 64 (1993) 2911.

[49] A. Cerezo, T. J. Godfrey, J. M. Hyde, S. J. Sijbrandij, G. D. W. Smith, *Appl. Surf. Sci.* 76/77 (1994) 374.

[50] M. K. Miller, A. Cerezo, M. G. Hetherington, and G. D. W. Smith, *'Atom Probe Microanalysis'*, Clarendon Press Oxford 1996.

[51] T. Al-Kassab, H. Wollenberger, G. Schmitz, and R. Kirchheim in M. Rühle and F. Ernst (eds.), *'High Resolution Imaging and Spectroscopy of Materials'*, to be published by Springer.

[52] D. Blavette, B. Deconihout, S. Chambreland and A. Bostel, *Ultramicr.* 70 (1998) 113.

[53] A. Ourmazd, F. H. Baumann, M. Bode, and Y. Kim, *Ultramicr.* 34 (1990) 237.

[54] P. Schwander, C. Kisielowski, M. Seibt, F. H. Baumann, Y. Kim, A. Ourmazd, *Phys. Rev. Lett.* 71 (1993) 4150.

[55] D. Stenkamp, W. Jäger, *Ultramicroscopy* 50 (1993) 321.

[56] Guido Schmitz, *'Hochauflösende Elektronenmikroskopie zur strukturellen und analytischen Untersuchung binärer Aluminiumlegierungen'*, Doctoral Thesis, Universität Göttingen 1994.

[57] G. Schmitz and F. Haider, *Scripta Mater.* 37 (1997) 1951.

[58] M. M. J. Treacy and J. M. Gibson, *Ultramicr.* 52 (1993) 31.

[59] G. Schmitz, J.C. Ewert and F. Hartung, *Ultramicr.* 77 (1999) p. 49. (see fig. 10)

[60] Frank Hartung, *'Untersuchung der Interreaktion von Cu-Au mit Hilfe der Z-Kontrast Elektronenmikroskopie'*, Diploma thesis, Universität Göttingen, 1996.

[61] S. Goudsmit, J. L. Saunderson, *Phys. Rev.* 57 (1940) 24.

[62] G. Wentzel, *Z. Phys.* 40 (1927) 590.

[63] Frank Hartung, *'Interdiffusion und Interreaktion in metallischen Schichtsystemen unter dem Einfluss diffusionsinduzierter Spannungen'*, Doctoral Thesis, Universität Göttingen 2000.

[64] P. Hartel, H. Rose, and C. Dinges, *Ultramicr.* 69 (1996) 63.

[65] F. Hartung and G. Schmitz, *Phys. Rev. B* (submitted.)

[66] W. A. Johnson, *Trans. AIME* 147 (1942) 331.

[67] H. E. Cook and J.E. Hilliard, *J. appl. phys.* 40 (1969) 2191.

[68] K. Meinel, M. Klaua and H. Bethge, *Thin solid films* 34 (1976) 157.

[69] S. K. Wonnel, J. M. Delaye, M. Bibole and Y. Limoge, *J. appl. phys.* 72 (1992) 5195.

[70] S. J. Sijbrandij, A. Cerezo, G. D. W. Smith, *Appl. Surf. Sci.* 87/88 (1995) 414.

[71] S. V. Krishnaswamy, R. Messier, Y. S. Ng, T. T. Tsong, *J. Vac. Sci. Technol.* 17 (1980) 63.

[72] T. Jeske, G. Schmitz and R. Kirchheim, *Mat. Sci. Eng.* 270 A (1999) 64.

[73] J. Schleiwies and G. Schmitz, *Mat. Sci. Eng.* (in press).

[74] J. Schleiwies, diploma thesis, Universität Göttingen 1998.

[75] K. Hono, N. Hasegawa, R. Okano, H. Fujimori, T. Sakurai, *Appl. Surf. Sci.* 67 (1993) 407.

[76] J. Schleiwies, doctoral thesis, Universität Göttingen (in preparation).

[77] D. J. Larson, R. L. Martens, T. F. Kelly, M. K. Miller, N. Tabat, *J. Appl. Phys.* 87 (2000) 5989.

[78] I. Rozdilkski, A. Cerezo, G. D. W. Smith and A. Watson *Proc. of MRS* 686 (1998) 521.

[79] L. Reich, M. Murayama and K. Hono, *Acta Mater.* 46, 6053.

[80] P. Bas, A. Bostel, B. Deconihout, and D. Blavette, *Apl. Surf. Sci.* 87/88 (1995) 298.

[81] J. Schleiwies, G. Schmitz, S. Heitmann and A. Hütten, *Apl. Phys. Lett.* (submitted).

[82] J. W. Cahn, J. E. Hilliard, *J. Chem. Phys.* 28 (1958) 258.

[83] M. Hillert, *Acta Met.* 9 (1961) 525.

[84] J. W. Cahn, *Acta Met.* 9 (1961) 795.

[85] J. DuMond, J. P. Youtz, *J. Appl Phys.* 11 (1940) 357.

[86] E. M. Philowsky and J. E. Hilliard, *J. Appl. Phys.* 40 (1969) 2198.

[87] F.-L. Yang, A. L. Greer and R. E. Somekh, *Thin Solid Films* 275 (1996) 258.

[88] F. C. Larché, J. W. Cahn, *Acta metall.* 30 (1982) 1835.

[89] F. C. Larché, J. W. Cahn, *Acta metall.* 33 (1985) 331.

[90] G. B. Stephenson, *Acta metall.* 36 (1988) 2663.

[91] A. L. Greer, *Def. Diff. Forum* 129-130 (1996) 163.

[92] K. N. Tu, *J. Appl. Phys.* 48 (1977) 3400.

[93] J. W. Cahn, J. D. Pan, R. W. Balluffi, *Scripta metall.* 13 (1979) 503.

[94] J. E. Marcur and R. W. Vook, *Thin Solid Films* 66 (1980) 371.

[95] P. Pirouz, F. Ernst, Y. Ikuhara, *Sol. State Phenomena* 59-60 (1998) 51.

[96] G. Gladyszewski, *Thin Solid Films* 204 (1991) 473.

[97] C. Lang and G. Schmitz *proc. DIMAT 2000* (in print).

[98] J. C. Ewert, F. Hartung, and G. Schmitz, *Appl. Phys. Lett.* 71 (1997) 1311.

[99] P. A. Stadelmann, *Ultrmicr.* 21 (1987) 131.

[100] H. Mehrer, *Landoldt-Börnstein: Diffusion in solid metals and alloys*, Berlin 1990.

[101] W. D. Nix, *Met. Trans. A* 20 (1989) 2217.

[102] G. Simmons and H. Wang, *single crystal elastic constants and calculated aggregate properties*, Cambridge 1971.

[103] R. Cahn and P. Haasen (eds.) *Physical Metallurgy* Amsterdam 1983.

[104] J. C. Ewert, F. Hartung, G. Schmitz, *Appl. Phys. Let.* 71 (1997) 1311.

[105] W. B. Pearson, *A handbook of lattice spacing and structures of metals and alloys*, Volume II, London 1967.

[106] J. P. Hirth and J. Lothe, *Theory of dislocations* New York, 1982.

[107] D. N. Yoon, *Ann. Rev. Mater. Sci.* 19 (1989) 43.

[108] S. Fujikawa, M. Werner, H. Mehrer, and A. Seeger, *Mater. Sci. Forum* 15-18 (1987) 431.

[109] C. T. Tomizuka, *Bull. Amer. Phys. Soc.* 2 (1957) 123.

[110] A. E. Austin, N. A. Richard, and E. Wood, *J. Appl. Phys.* 37 (1966) 3651.

[111] A. Chatterjee and D. J. Fabian, *Acta Metall.* 17 (1969) 1141.

[112] F. J. A. den Broeder, M. Klerk, J. M. Vandenberg, R. A. Hamm, *Acta Metall.* 31 (1983) 285.

[113] B. Sundmann, S. G. Fries and W. A. Oates, *Z. Metallkd.* 90 (1999) 4.

[114] K. N. Tu and B. S. Berry, *J. Appl. Phys.* 43 (1972) 3283.

[115] J. A. Borders, *Thin Solid Films* 19 (1973) 359.

[116] R. Baur, V. Gerold, *Z. Metallkunde* 52 (1961) 671.

[117] J. E. E. Baglin, F. M. d'Heurle, and W. N. Hammer, *J. Appl. Phys.* 50 (1978) 266.

[118] C. Weaver, L. C. Brown, *Phil. Mag.* 17 (1968) 881.

[119] J. E. Westmoreland, W. H. Weisenberger, *Thin Solid Films* 19, 349 (1973).

[120] G. Schmitz, O. Svenson, P. Troche, F. Harbsmeier in M. Koiwa, K. Otsuka, T. Miyazaki (eds.) *Solid-Solid Phase Transformations* Japan Inst. of Metals 1999.

[121] O. Svenson, '*Interreaktion von Al/Ag Schichten*, Diploma thesis, Universität Göttingen 1999.

[122] D. Blavette, E. Cadel, A. Franczkiewicz, A. Menand, *Science* 286 (1999) 2317.

[123] R. B. Nicholson, J. Nutting, *Acta Metall.* 9 (1961) 332.

[124] F. Gärtner, *private communication*.

[125] T. Jeske, *doctoral thesis* Univ. Göttingen (in preparation).

[126] E. G. Colgan, J. W. Mayer, *Nuc. Instr. Meth. B* 17 (1986) 242.

[127] E. G. Colgan, *Mater. Sci. Rep.* 5 (1990) 1.

[128] A. Csanády, A. Csordás-Pintér, L. Varga, L. Tóth, G. Vincze, *J. Phys. I France* 6 (1996) 925.

[129] E. Ma, M. A. Nicolet, M. Nathan, *J. Appl. Phys.* 65 (1989) 2703.

[130] E. M. Ma, C. V. Thompson, L. A. Clevenger, *J. Appl. Phys.* 69 (1991) 2211.

[131] R. Pretorius, R. de Reus, A.M. Vredenberg and F. W. Saris, *Mat. Lett.* 9 (1990) 494.

[132] M. M. P. Janssen and G. D. Riek, *Trans. Met. Soc. AIME* 239 (1967) 1372.

[133] K. Barmak, C. Michaelsen, G. Lucadamo, *J. Mater. Res.* 12 (1997) 133.

[134] S. Shankar and L.L. Seigle, *Metall. Trans. A* 9 (1978) 1467.

[135] J. C. Ewert, G. Schmitz *Europ. Phys. J. B* 17 (2000) 391.

[136] F. Hodaj, P. J. Desré *Acta Materialia* 44 (1996) 4485.

[137] P. Haasen, '*Physical Metallurgy*' Cambridge 1996 p. 212.

[138] N. Metropolis, *J. Chem. Phys.* 21 (1953) 1087.

[139] C. Kittel, *Einführung in die Festkörperphysik* München 1973, p. 128.